Monograph Series on
Computational Modeling of Forming Processes

Edited by C. Agelet de Saracibar

On the Computational Modeling and Numerical Simulation of FSW Processes

C. Agelet de Saracibar, M. Chiumenti, M. Cervera,
N. Dialami, D. Santiago, G. Lombera

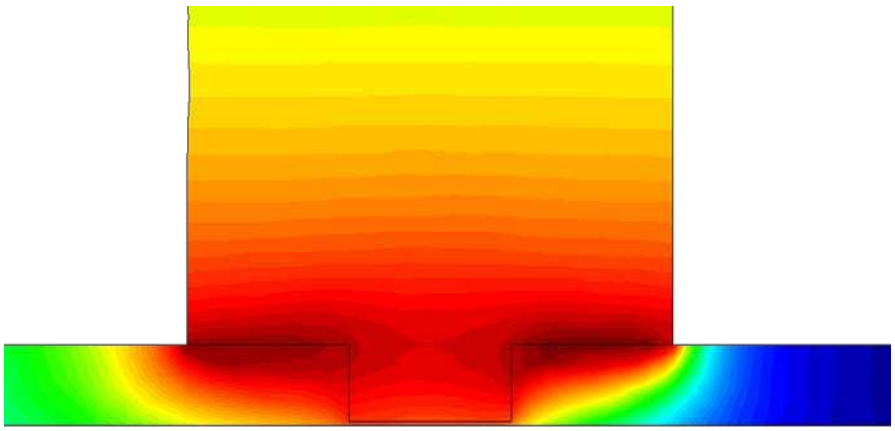

On the Computational Modeling and Numerical Simulation of FSW Processes

C. Agelet de Saracibar*♦, M. Chiumenti*♦, M. Cervera*♦, N. Dialami*,
D. Santiagoº, G. Lomberaº

♦ETS Ingenieros de Caminos, Canales y Puertos, UPC, Barcelona, Spain
*International Center for Numerical Methods in Engineering (CIMNE), Barcelona, Spain
ºGrupo de Ingeniería Asistido por Computadora, Universidad Nacional de Mar del Plata, Mar del Plata, Argentina

agelet@cimne.upc.edu, michele@cimne.upc.edu, miguel.cervera@upc.edu, narges@cimne.upc.edu, dsantiago@fi.mdp.edu.ar, glombera@fi.mdp.edu.ar

December 2011

Table of contents

Abstract

This paper deals with the computational modeling and numerical simulation of the material flow around the probe tool in a Friction Stir Welding (FSW) process. Within the paradigmatic framework of the multiscale stabilization methods, suitable subgrid scale stabilized coupled thermomechanical formulations have been developed using an Eulerian description. Norton-Hoff and Sheppard-Wright thermo-rigid-viscoplastic constitutive material models have been considered. Constitutive equations for the subgrid scale models have been proposed and an approximation of the subgrid scale variables has been given. In particular Algebraic Subgrid Scale (ASGS) and Orthogonal Subgrid Scale (OSGS) methods for P1/P1/P1 linear elements have been considered. Furthermore, it has been shown that well known classical stabilized formulations, such as the Galerkin Least-Squares (GLS) or Streamline Upwind/Petrov-Galerkin (SUPG) methods, can be recovered as particular cases of the multiscale stabilization framework considered.

Within the framework of a product formula algorithm, the resulting algebraic system of equations has been solved using a staggered procedure, in which a mechanical problem, defined by the plastic strain rate incompressibility equation and the quasi-static linear momentum balance equation, is solved at a constant temperature and a thermal problem, defined by the energy balance equation, is solved keeping constant the mechanical variables.

The computational model has been implemented in the in-house developed FE software COMET. An assessment of the influence of the thermal deformation in the formulation has been carried out. Results obtained show that the influence of the thermal deformation is very small and can be neglected, getting a fully incompressible formulation.

Finally, the computational model implemented in COMET has been validated through a number of examples, including a 3D numerical simulation of a FSW process. Numerical results obtained have been compared with experimental results available in the literature. A good agreement on the temperature distribution has been obtained and predicted peak temperatures compare well, both in value and position, with the experimental results available.

1. Introduction

Friction Stir Welding (FSW) is a new method of welding in solid state, created and patented by “The Welding Institute” (TWI) in 1991. In FSW a cylindrical, shouldered tool with a profiled probe is rotated and slowly plunged into the joint line between two pieces of sheet or plate material, which are butted together. The parts have to be clamped onto a backing bar in a manner that prevents the abutting joint faces from being forced apart. Once the probe has been completely inserted, it is moved with a small tilt angle in the welding direction. The shoulder applies a pressure on the material to constrain the plasticised material around the probe tool. Due to the advancing and rotating effect of the probe and shoulder of the tool along the seam, an advancing side and a retreating side are formed and the softened and heated material flows around the probe to its backside where the material is consolidated to create a high-quality solid-state weld. The maximum temperature reached is of the order of 0.8 of the melting temperature. Despite the simplicity of the procedure, the mechanisms behind the process and the material flow around the probe tool are very complex. The material is extruded around the rotating tool and a vortex flow field near the probe due to the downward flow is induced by the probe thread. The process can be regarded as a solid phase keyhole welding technique since a hole to accommodate the probe is generated, then filled

during the welding sequence. The material flow depends on welding process parameters, such as welding and rotation speed, pressure, etc., and on the characteristics of the tools, such as materials, design, etc.

The first applications of FSW have been in aluminium fabrications. The weld quality is excellent, with none of the porosity that can arise in fusion welding, and the mechanical properties are at least as good as the best achievable by fusion welding. The process is environmentally friendly, because no fumes or spatter are generated, and there is no arc glare or reflected laser beams with which to contend. Another major advantage is that, by avoiding the creation of a molten pool which shrinks significantly on re-solidification, the distortion after welding and the residual stresses are low. With regard to joint fit up, the process can accommodate a gap of up to 10% of the material thickness without impairing the quality of the resulting weld. As far as the rate of processing is concerned, for materials of 2 mm thickness, welding speeds of up to 2 $m.min^{-1}$ can be achieved, and for 5 mm thickness up to 0.75 $m.min^{-1}$. Recent tool developments are confidently expected to improve on these figures.

Friction stir welding has been used to weld all wrought aluminium alloys, across the AA-2xxx, AA-5xxx, AA-6xxx and AA-7xxx series of alloys, some of which are bordering on being classed as virtually unweldable by fusion welding techniques. The process can also weld dissimilar aluminium alloys, whereas fusion welding may result in the alloying elements from the different alloys interacting to form deleterious intermetallics through precipitation during solidification from the molten weld pool. Friction stir welding can also make hybrid components by joining dissimilar materials such as aluminium and magnesium alloys. The thicknesses of AA-6082-T6 that have so far been welded have ranged from 1.2 mm to 50 mm in a single pass, to more than 75 mm when welding from both sides. Welds have also been made in pressure die cast aluminium material without any problems from pockets of entrapped high pressure gas, which would violently disrupt a molten weld pool encountering them.

The original application for friction stir welding was the welding of long lengths of material in the aerospace, shipbuilding and railway industries. Examples include large fuel tanks and other containers for space launch vehicles, cargo decks for high-speed ferries, and floors for railway carriages. FSW is used already in routine, as well as in critical applications, for the joining of structural components made of aluminum and its alloys. Indeed, it has been convincingly demonstrated that the process results in strong and ductile joints, sometimes in systems which have proved difficult using conventional welding techniques. The process is most suitable for components which are flat and long (plates and sheets) but can be adapted for pipes, hollow sections and positional welding.

The computational modeling of FSW processes is a complex task and it has been a research topic of increasing interest in computational mechanics during the last decades. Xu et al. (2001) [46] and Xu and Deng (2003, 2004) [47, 48] developed a 3D FE procedure to simulate the FSW process using the commercial FEM code ABAQUS, focusing on the velocity field, the material flow characteristics and the equivalent plastic strain distribution,. The authors use an ALE formulation with adaptive meshing and consider large elasto-plastic deformations and temperature-dependent material properties. However, the authors did not perform a fully coupled thermo-mechanical simulation, superimposing the temperature map obtained from the experiments as a prescribed temperature field to perform the mechanical analysis. The numerical results were compared to experimental data available, showing a reasonable good correlation between the equivalent plastic strain distributions and the distribution of the microstructure zones in the weld.

Ulysse (2002) [44] presented a fully coupled 3D FEM visco-plastic model for FSW of thick aluminum plates using the commercial FEM code FIDAP. The author investigated the

effect of tool speeds on the process parameters. It was found that a higher translational speed leads to a higher welding force, while increasing the rotational speed has the opposite effect, that of force reduction. Reasonable agreement between the predicted and the measured temperature was obtained and the discrepancies were explained by an inadequate representation of the constitutive behavior of the material for the wide ranges of strain-rate, temperatures and strains typically found during FSW.

Chen and Kovacevic (2003) [12] developed a 3D FEM model to study the thermal history and thermo-mechanical phenomena in the butt-welding of aluminum alloy AA-6061-T6 using the commercial FEM code ANSYS. Their model incorporated the mechanical reaction between the tool and the weld material. Experiments were conducted and an X-ray diffraction technique was used to measure the residual stress in the welded plate. The welding tool (i.e. the shoulder and pin) in the FEM model was modeled as a heat source, with the nodes moved forward at each computational time step. This simple model severely limited the accuracy of the stress and force predictions.

Colegrove et al. (2000, 2004) [19, 20] used the CFD commercial software FLUENT for a 2D and 3D numerical investigation on the influence of pin geometry during FSW, comparing different pin shapes in terms of material flow and welding forces on the basis of both a stick and a slip boundary condition at the tool-workpiece interface. In spite of the good obtained results, the accuracy of the analysis is limited by the assumption of isothermal conditions.

Seidel and Reynolds (2003) [40] also used the CFD commercial software FLUENT to model the 2D steady-state flow around a cylindrical tool.

Bendzsak et al. (2000) [4, 5] used the Eulerian code Stir3D to model the flow around a FSW tool, including the tool thread and tilt angle in the tool geometry and obtaining complex flow patterns. The temperature effects on the viscosity were neglected.

Schmidt and Hattel (2004) [38] presented the development of a 3D fully coupled thermo mechanical FE model in ABAQUS/Explicit using the Arbitrary Lagrangian Eulerian (ALE) formulation. The flexibility of the FSW machine was taken into account be connecting the rigid tool to a spring. The workpiece was modeled as a cylindrical volume with inlet and outlet boundary conditions. A rigid backplate was used. The contact forces were modeled using a Coulomb friction law, and the surface was allowed to separate. Heat generated by friction and plastic deformation is considered. The simulation modeled the dwell and weld phases of the process.

Askari et al. (2003) [3] used the CTH hydrocode coupled to an advection-diffusion solver for the energy balance equation. The CTH code uses the finite volume method to discretise the domain. The elastic response was taken into account in this case. The results proved encouraging with respect to gaining an understanding of the material flow around the tool. However, simplified friction conditions were used.

Nikiforakis (2005) [37] used a finite difference method to model the FSW process. Despite the fact that he was only presenting 2D results, the model proposed had the advantage of minimizing calibration of model parameters, taking into account a maximum of physical effects. A transient and fully coupled thermo-fluid analysis was performed. The rotation of the tool was handled through the use of the overlapping grid method. A rigid-viscoplastic material law was used and sticking contact at the tool work piece interface was assumed. Hence, heating was due to plastic deformation only.

Heurtier et al. (2006) [30] used a 3D semi-analytical coupled thermomechanical FE model to simulate FSW processes. The model uses an analytical velocity field and considers heat input from the tool shoulder and plastic strain of the bulk material. Trajectories, temperature, strain, strain rate fields and micro-hardness in various weld zones are computed and compared to experimental results obtained on an AA 2024-T351 alloy FSW joint.

Buffa et al. (2006) [6] using the commercial FE software DEFORM-3D, proposed a 3D Lagrangian, implicit, coupled thermo-mechanical numerical model for the simulation of FSW processes, using a rigid-viscoplastic material description and a continuum assumption for the weld seam. The proposed model is able to predict the effect of process parameters on process variables, such as the temperature, strain and strain rate fields, as well as material flow and forces. A reasonable good agreement between the numerically predicted results, on forces and temperature distribution, and experimental data was obtained. The authors found that the temperature distribution about the weld line is nearly symmetric because the heat generation during FSW is dominated by rotating speed of the tool, which is much higher than the advancing speed. On the other hand, the material flow in the weld zone is non symmetrically distributed about the weld line because the material flow during FSW is mainly controlled by both advancing and rotating speeds.

De Vuyst et al. [22-25] used the coupled thermo-mechanical finite element code MORFEO to simulate the flow around simplified tool geometries for FSW process. The rotation and advancing speed of the tool were modeled using prescribed velocity fields. An attempt to consider features associated to the geometrical details of the probe and shoulder, which had not been discretised in the FE model in order to avoid very large meshes, was taken into account using additional special velocity boundary conditions. In spite of that, a mesh of roughly 250,000 nodes and almost 1.5 million of linear tetrahedral elements was used. A Norton-Hoff rigid-viscoplastic constitutive equation was considered, with averaged values of the consistency and strain rate sensitivity constitutive parameters determined from hot torsion tests performed over a range of temperatures and strain rates. The computed streamlines were compared with the flow visualization experimental results obtained using copper marker material sheets inserted transversally or longitudinally to the weld line. The simulation results correlate well when compared to markers inserted transversely to the welding direction. However, when compared to a marker inserted along the weld centerline only qualitative results could be obtained. The correlation may be improved by modeling the effective weld thickness of the experiment, using a more realistic material model, for example, by incorporating a yield stress or temperature dependent properties, refine velocity boundary conditions or further refining the mesh in specific zones, such as for instance, under the probe. The authors conclude that it is essential to take into account the effects of the probe thread and should thread in order to get realistic flow fields.

On the experimental side, several flow visualization techniques have been developed by a number of authors. Colligan (1999) [21] used steel shot makers embedded in the weld zone of AA-6061-T6 and AA-7075-T6 aluminum alloys. Through X-ray analysis, he concluded that FSW is due to a combination of both stirring and extrusion of the material. Reynolds and Seidel (2001) [39] carried out similar experiments. However, they embedded AA-5454 aluminum alloy in AA-2195 aluminum alloy. The inserts were placed before welding in strategic positions in the depth of the weld at various positions relative to the weld line. They observed a difference of the material flow between the advancing side and the retreating side. They also provided 3D maps of the marker flow which indicate a modest vertical flow. Other authors used the friction stir weld of dissimilar materials to analyze the material flow. With this method, Li et al. (1999) [35] demonstrated very complex vortex flows associated to the FSW of AA-2024 aluminum to AA-6061 aluminum, showing that the flow pattern depends on the welding parameters. Guerra et al. (2003) [28] used Cu foils placed along the joint line of friction stir weld in AA-6061 Al alloy. When the steady state of welding is established, he stopped the tool. Using metallographic analysis, he demonstrated that several flow zones can be distinguished around the pin: a rotational zone which rotates with the velocity of the pin, a transition zone where no marker material was found and which was subjected to a very

different thermo-mechanical history. Dickerson et al. (2003) [26] performed experiments with 0.1 mm thick copper sheets placed transversally and longitudinally to the weld line. They analyzed the flow pattern by using metallography, 2D X-rays analysis and X-rays tomography. Their results are freely available to the FSW community. They show that copper sheets embedded into aluminum AA-2024-T3 could be successfully used as marker material. Moreover, it permits the use of a number of techniques to analyze the flow. Metallography appears to be a good technique, complementary to X-ray images.

This paper deals with the computational modeling and numerical simulation of the material flow around the probe tool in a Friction Stir Welding (FSW) process. The main motivations and goals behind this work are the following.

A first goal of this paper is to develop, within the paradigmatic framework of the multiscale stabilization methods, suitable subgrid scale stabilized coupled thermomechanical formulations for linear finite elements using an Eulerian description. Norton-Hoff and Sheppard-Wright thermo-rigid-viscoplastic constitutive material models are considered. Constitutive equations for the subgrid scale variables are proposed. Remarkably, a thermal conductivity for the themal subgrid scale is introduced and it is shown that it can be expressed as the Peclet number multiplied by the thermal conductivity of the material. Using those constitutive equations, an approximation of the subgrid scale variables and stabilization parameters is given. In particular Algebraic Subgrid Scale (ASGS) and Orthogonal Subgrid Scale (OSGS) methods for P1/P1/P1 elements are considered. Furthermore, it is shown that well known classical formulations, such as the Galerkin Least-Squares (GLS) or Streamline Upwind/Petrov-Galerkin (SUPG) methods, can be recovered as particular cases of the multiscale stabilization framework considered.

Within the framework of fractional step methods, a product formula algorithm is introduced and the resulting algebraic system of equations is solved using a staggered procedure, in which a mechanical problem, defined by the plastic strain rate incompressibility equation and the quasi-static linear momentum balance equation, is solved at constant temperature and then, a thermal problem, defined by the energy balance equation, is solved next keeping constant the mechanical variables.

A second goal of this work is to make an assessment of the influence of the thermal deformation in the formulation, in order to see if this contribution can be neglected and the problem turns out to be fully incompressible.

Finally, a third goal of this paper is to validate the computational model implemented in COMET, through a number of 2D and 3D numerical simulations of FSW processes. Numerical results obtained in the simulation are compared with other numerical or experimental results available in the literature.

The remaining of the paper is as follows. Section 2 deals with the computational model for the flow of the material around a tool probe in a FSW processes. Some key features of the FSW process are addressed and their implications in the computational model are first identified. The strong form of the governing equations and constitutive equations are provided and then, the mixed variational form of the governing equations is given. Next, the multiscale stabilization method is introduced, providing a constitutive equation for the subgrid scale variables (introducing viscosity and thermal conductivity subgrid scale parameters), giving an approximation of the subgrid scale variables and defining their associated stabilization parameters. ASGS and OSGS methods are considered and it is shown how GLS and SUPG methods can be recovered as particular cases. An operator split and product formula algorithm, defining mechanical and thermal problems, are introduced and the resulting algebraic systems of equations are written in matrix form. Finally a convenient staggered solution algorithm is presented.

Section 3 deals with the computational simulations. Three different examples have been chosen. The first two examples correspond to 2D numerical simulation of steady-state and transient, respectively, FSW processes. Numerical results obtained using COMET are compared with the ones provided by the in-house developed code Framework (FW) [45]. The software FW uses P2/P1 finite elements, a SUPG formulation and does not includes the thermal dilatation term in the formulation. An assessment of the thermal deformation is made in the second example. The third example is a 3D numerical simulation of a FSW process. The results obtained using COMET are compared with experimental results obtained by Zhu and Chao [51]. Finally some concluding remarks are drawn.

2. Computational Model

Let us start introducing some standard notation. Let Ω be an open and bounded domain of $\mathbb{R}^{n_{\text{dim}}}$, where n_{dim} is the number of dimensions of the space, $\bar{\Omega}$ its closure and $\partial\Omega$ its boundary. We assume that the boundary $\partial\Omega$ can be split into two disjoint sets $\partial_v\Omega$ and $\partial_\sigma\Omega$ such that $\partial\Omega = \partial_v\Omega \cup \partial_\sigma\Omega$ and $\partial_v\Omega \cap \partial_\sigma\Omega = \varnothing$, as well as also into two disjoint sets $\partial_\theta\Omega$ and $\partial_q\Omega$ such that $\partial\Omega = \partial_\theta\Omega \cup \partial_q\Omega$ and $\partial_\theta\Omega \cap \partial_q\Omega = \varnothing$. The space of square integrable functions in Ω is denoted by $L_2(\Omega)$ and the space of functions with derivatives up to order $m \geq 0$ belonging to $L_2(\Omega)$ is denoted by $H^m(\Omega)$. Bold characters are used for vector counterparts of these spaces. The L_2 inner products in Ω, $\partial\Omega$, $\partial_\sigma\Omega$ and $\partial_q\Omega$ are denoted as $(\cdot,\cdot)$, $(\cdot,\cdot)_{\partial\Omega}$, $(\cdot,\cdot)_{\partial_\sigma\Omega}$ and $(\cdot,\cdot)_{\partial_q\Omega}$, respectively. Hereafter, orthogonality will be understood with respect to this product.

2.1 Computational Modeling of FSW Processes

The flow of the material around a FSW tool is characterized by a Reynolds number which is much smaller than 1, typically around 10^{-4}, due to the small length scale, the low velocities and the very high viscosity of the material. For these values of the Reynolds number, the inertial forces of the linear momentum balance equation can be neglected and a quasi-static analysis can be performed.

The deformation of the material taking place around a FSW tool is extremely high. The computational modeling of the material flow around a FSW tool using a Lagrangian formulation requires continuous remeshing to avoid extremely distorted mesh elements. Therefore, the use of alternative formulations, such as an ALE formulation or an Eulerian formulation, is a better choice. In this work we will use an Eulerian formulation.

On the other hand, the Peclet number for a FSW process typically ranges from 10^1 to 10^3. For this range of values of the Peclet number, the convective term of the spatial energy balance equation cannot be neglected. Transient conditions will be considered.

Coupled thermo-mechanical rigid-viscoplastic constitutive material models, such as the Norton-Hoff or the Sheppard-Wright models, will be considered.

The resulting coupled thermo-mechanical problem will be solved using a product formula algorithm, leading to a staggered solution algorithm. A mechanical problem, involving mechanical variables as unknowns, is defined at constant temperature and a thermal problem, involving the temperature as unknown, is defined at constant configuration.

A pressure stabilized mixed linear velocity/linear pressure finite element interpolation formulation will be used to solve the mechanical problem and a convection stabilized linear temperature interpolation formulation will be used to solve the thermal problem.

2.2 *Mixed Strong Form of the Quasi-static Transient Coupled Thermo-mechanical Problem in Eulerian Form*

Let us consider a spatial velocity vector field $\mathbf{v}(\mathbf{x},t)$, a spatial pressure field $p(\mathbf{x},t)$ and a spatial temperature field $\theta(\mathbf{x},t)$. Within the framework of a coupled thermo-mechanical mixed velocity-pressure formulation, the Cauchy stress tensor field is given by an appropriate constitutive equation as a function of the velocity, pressure and temperature fields, such that,

$$\sigma(\mathbf{v},p,\theta) = p\mathbf{1} + \mathbf{s}(\mathbf{v},\theta) \tag{1}$$

where $\mathbf{s}(\mathbf{v},\theta) := \operatorname{dev}\sigma(\mathbf{v},p,\theta)$ is the deviatoric part of the Cauchy stress tensor.

Appropriate boundary conditions, such as a prescribed velocity field $\overline{\mathbf{v}}(\mathbf{x},t)$ on $\partial_v\Omega$, prescribed traction field $\overline{\mathbf{t}}(\mathbf{x},t)$ on $\partial_\sigma\Omega$, a prescribed temperature field $\overline{\theta}(\mathbf{x},t)$ on $\partial_\theta\Omega$ and prescribed normal heat flux field per unit of surface $\overline{q}(\mathbf{x},t)$ on $\partial_q\Omega$, and initial conditions, such as an initial temperature field $\theta_0(\mathbf{x})$ in Ω, are condidered.

The mixed strong form of the quasi-static transient coupled thermo-mechanical problem is defined by the momentum balance equation, the rigid plastic incompressibility equation and the energy balance equation (neglecting elastoplastic heating terms) and using a spatial Eulerian formulation can be stated as:

Find a velocity vector field $\mathbf{v}(\mathbf{x},t)$, *a pressure field* $p(\mathbf{x},t)$ *and a temperature field* $\theta(\mathbf{x},t)$, *such that the following equations hold in* Ω:

$$\nabla p + \nabla\cdot\mathbf{s}(\mathbf{v},\theta) + \mathbf{f} = 0 \tag{2}$$

$$\nabla\cdot\mathbf{v} - \frac{\partial e^\theta(\theta)}{\partial t} - \mathbf{v}\cdot\nabla e^\theta(\theta) = 0 \tag{3}$$

$$c_0\frac{\partial\theta}{\partial t} + c_0\mathbf{v}\cdot\nabla\theta = -\nabla\cdot\mathbf{q}(\theta) + R + \mathcal{D} \tag{4}$$

and $\mathbf{v}(\mathbf{x},t) = \overline{\mathbf{v}}(\mathbf{x},t)$ *on* $\partial_v\Omega$, $p(\mathbf{x},t)\mathbf{n} + \mathbf{s}(\mathbf{x},t)\cdot\mathbf{n} = \overline{\mathbf{t}}(\mathbf{x},t)$ *on* $\partial_\sigma\Omega$, $\theta(\mathbf{x},t) = \overline{\theta}(\mathbf{x},t)$ *on* $\partial_\theta\Omega$, $\mathbf{q}(\mathbf{x},t)\mathbf{n} = \overline{q}(\mathbf{x},t)$ *on* $\partial_q\Omega$ *and* $\theta(\mathbf{x},t=0) = \theta_0(\mathbf{x})$ in Ω.

where $\mathbf{f}$ is the body forces vector per unit of volume, $e^\theta(\theta)$ is the volumetric thermal strain (taking into account the thermal expansion in solid state and the thermal shrinkage during the liquid-solid phase change), c_0 is the heat capacity, $\mathbf{q}$ is the heat flux vector per unit of surface, R is an internal heat source rate per unit of volume and $\mathcal{D}$ is the internal dissipation rate per unit of volume. Additionally, appropriate constitutive equations for the deviatoric part of the Cauchy stress, as a function of the velocity (or the velocity and the temperature), and for the heat flux per unit of surface, as a function of the temperature, have to be supplied.

Using a compact notation, collecting the velocity vector field, the pressure field and the temperature field into a generalised vector field $\mathbf{V}$, the strong form of the quasi-static transient coupled thermo-mechanical problem in mixed form can be stated as:

Find a vector field $\mathbf{V}$, *such that the following equations hold in* Ω:

$$\mathcal{L}(\mathbf{V}) = \mathcal{F} \tag{5}$$

where $\mathbf{V}$, $\mathcal{L}(\mathbf{V})$ and $\mathcal{F}$ are given by

$$\mathbf{V} := \begin{bmatrix} \mathbf{v} \\ p \\ \theta \end{bmatrix}, \quad \mathcal{L}(\mathbf{V}) = \begin{bmatrix} -\nabla p - \nabla \cdot \mathbf{s}(\mathbf{v},\theta) \\ \nabla \cdot \mathbf{v} - \dfrac{\partial e^{\theta}(\theta)}{\partial t} - \mathbf{v} \cdot \nabla e^{\theta}(\theta) \\ c_0 \dfrac{\partial \theta}{\partial t} + c_0 \mathbf{v} \cdot \nabla \theta + \nabla \cdot \mathbf{q}(\theta) - \mathcal{D} \end{bmatrix}, \quad \mathcal{F} = \begin{bmatrix} \mathbf{f} \\ 0 \\ R \end{bmatrix} \tag{6}$$

2.2.1 *Constitutive equations*

Different constitutive models for the deviatoric part of the stresses can be used in the simulation of a FSW process. Here the rigid plastic Norton-Hoff and Sheppard-Wright constitutive material models are considered. Furthermore, the Fourier law is used as thermal constitutive model.

Norton-Hoff constitutive model. The rigid-plastic Norton-Hoff constitutive model is given by,

$$\mathbf{s}(\mathbf{v},\theta) = K(\theta)\left(\sqrt{3}\dot{\bar{\varepsilon}}(\mathbf{v})\right)^{m(\theta)-1} \dot{\boldsymbol{\varepsilon}}^{p}(\mathbf{v}) =: 2\mu\left(\dot{\bar{\varepsilon}}(\mathbf{v}),\theta\right) dev\left(\dot{\boldsymbol{\varepsilon}}(\mathbf{v})\right) \tag{7}$$

where $K(\theta)$ is a temperature dependent consistency parameter, $m(\theta)$ is a temperature dependent rate sensitivity parameter, $\dot{\boldsymbol{\varepsilon}}(\mathbf{v}) = \nabla^{s}\mathbf{v}$ is the deformation rate, defined as the symmetric part of the spatial velocity gradient, and $\dot{\bar{\varepsilon}}$ is the equivalent strain rate given by,

$$\dot{\bar{\varepsilon}} = \sqrt{2/3}\,\left\|\dot{\boldsymbol{\varepsilon}}^{p}\right\| = \sqrt{2/3}\,\left\|dev\left(\dot{\boldsymbol{\varepsilon}}\right)\right\| \tag{8}$$

where the norm $\left\|\dot{\boldsymbol{\varepsilon}}^{p}\right\|$ is given by,

$$\left\|\dot{\boldsymbol{\varepsilon}}^{p}\right\| = \left(\dot{\boldsymbol{\varepsilon}}^{p} : \dot{\boldsymbol{\varepsilon}}^{p}\right)^{1/2} \tag{9}$$

and $\mu\left(\dot{\bar{\varepsilon}}(\mathbf{v}),\theta\right)$ is the effective viscosity parameter.

Sheppard-Wright constitutive model. The rigid-plastic Sheppard-Wright constitutive model is given by,

$$\mathbf{s}(\mathbf{v},\theta) = 2\mu\left(\dot{\bar{\varepsilon}}(\mathbf{v}),\theta\right)\dot{\boldsymbol{\varepsilon}}^{p}(\mathbf{v}) = 2\mu\left(\dot{\bar{\varepsilon}}(\mathbf{v}),\theta\right) dev\left(\dot{\boldsymbol{\varepsilon}}(\mathbf{v})\right) \tag{10}$$

where the strain rate and temperature-dependent viscosity parameter $\mu\left(\dot{\bar{\varepsilon}}(\mathbf{v}),\theta\right)$ is given by,

$$\mu\left(\dot{\bar{\varepsilon}}(\mathbf{v}),\theta\right) = \frac{\sigma_e\left(\dot{\bar{\varepsilon}}(\mathbf{v}),\theta\right)}{3\dot{\bar{\varepsilon}}(\mathbf{v})} \tag{11}$$

where the strain rate and temperature-dependent yield stress is given by,

$$\sigma_e\left(\dot{\bar{\varepsilon}}(\mathbf{v}),\theta\right) = \frac{1}{\alpha}\log\left[\left(\frac{Z\left(\dot{\bar{\varepsilon}}(\mathbf{v}),\theta\right)}{A}\right)^{1/n} + \sqrt{1+\left(\frac{Z\left(\dot{\bar{\varepsilon}}(\mathbf{v}),\theta\right)}{A}\right)^{2/n}}\right] \tag{12}$$

where the Zener-Hollomon parameter $Z\left(\dot{\bar{\varepsilon}}(\mathbf{v}),\theta\right)$, representing the temperature compensated effective strain rate, is given by,

$$Z\left(\dot{\bar{\varepsilon}}(\mathbf{v}),\theta\right) = \dot{\bar{\varepsilon}}(\mathbf{v})\exp\left(\frac{Q}{R\theta}\right) \tag{13}$$

and α, A and n are material parameters, R is the universal gas constant and Q is the activation energy.

Fourier law. The thermal constitutive equation for the heat flux per unit of surface is defined by the Fourier law given by,

$$\mathbf{q}(\theta) = -k(\theta)\nabla\theta \tag{14}$$

where $k(\theta)$ is the temperature-dependent thermal conductivity.

2.3 *Mixed Variational Form of the Quasi-static Transient Coupled Thermo-mechanical Problem in Eulerian Form*

Let us consider the following infinite dimensional spaces,

$$\mathcal{V} = \left\{ \mathbf{v} \in \mathbf{H}^1(\Omega) \,|\, \mathbf{v} = \overline{\mathbf{v}} \text{ on } \partial_v\Omega \right\} \tag{15}$$

$$\mathcal{Q} = L^2(\Omega) \tag{16}$$

$$\mathcal{T} = \left\{ \theta \in H^1(\Omega) \,|\, \theta = \overline{\theta} \text{ on } \partial_\theta\Omega \right\} \tag{17}$$

$$\mathcal{V}_0 = \left\{ \delta\mathbf{v} \in \mathbf{H}^1(\Omega) \,|\, \delta\mathbf{v} = \mathbf{0} \text{ on } \partial_v\Omega \right\} \tag{18}$$

$$\mathcal{T}_0 = \left\{ \delta\theta \in H^1(\Omega) \,|\, \delta\theta = 0 \text{ on } \partial_\theta\Omega \right\} \tag{19}$$

and let us introduce the infinite dimensional spaces $\mathcal{W} := \mathcal{V} \times \mathcal{Q} \times \mathcal{T}$ and $\mathcal{W}_0 := \mathcal{V}_0 \times \mathcal{Q} \times \mathcal{T}_0$.

The mixed variational form of the quasi-static transient coupled thermo-mechanical problem defined in strong form by (8)-(9), can be stated, using a compact short notation, as:

Find a vector field $\mathbf{V} \in \mathcal{W}$*, such that the following equations hold in* Ω*:*

$$\left(\mathcal{L}(\mathbf{V}), \delta\mathbf{V}\right) = \left(\mathcal{F}, \delta\mathbf{V}\right) \quad \forall \delta\mathbf{V} \in \mathcal{W}_0 \tag{20}$$

where $\delta\mathbf{V}$ is given by

$$\delta\mathbf{V} := \begin{bmatrix} \delta\mathbf{v} \\ \delta p \\ \delta\theta \end{bmatrix} \tag{21}$$

Developing (20), the mixed variational form of the quasi-static transient coupled thermo-mechanical problem defined in strong form by (5)-(7) can be stated as:

Find a velocity vector field $\mathbf{v} \in \mathcal{V}$*, a pressure field* $p \in \mathcal{Q}$ *and a temperature field* $\theta \in \mathcal{T}$*, such that the following equations hold in* Ω*:*

$$-\left(\nabla p, \delta\mathbf{v}\right) - \left(\nabla\cdot\mathbf{s}(\mathbf{v},\theta), \delta\mathbf{v}\right) = \left(\mathbf{f}, \delta\mathbf{v}\right) \quad \forall \delta\mathbf{v} \in \mathcal{V}_0 \tag{22}$$

$$\left(\nabla\cdot\mathbf{v}, \delta p\right) - \left(\frac{\partial e^\theta(\theta)}{\partial t}, \delta p\right) - \left(\mathbf{v}\cdot\nabla e^\theta(\theta), \delta p\right) = 0 \quad \forall \delta p \in \mathcal{Q} \tag{23}$$

$$\left(c_0 \frac{\partial\theta}{\partial t}, \delta\theta\right) + \left(c_0\mathbf{v}\cdot\nabla\theta, \delta\theta\right) + \left(\nabla\cdot\mathbf{q}(\theta), \delta\theta\right) - \left(\mathcal{D}, \delta\theta\right) = \left(R, \delta\theta\right) \quad \forall \delta\theta \in \mathcal{T}_0 \tag{24}$$

Integrating by parts the following expressions,

$$-\left(\nabla p, \delta\mathbf{v}\right) - \left(\nabla\cdot\mathbf{s}(\mathbf{v},\theta), \delta\mathbf{v}\right) = \left(p, \nabla\cdot\delta\mathbf{v}\right) + \left(\mathbf{s}(\mathbf{v},\theta), \nabla^s\delta\mathbf{v}\right) - \left(\overline{\mathbf{t}}, \delta\mathbf{v}\right)_{\partial_\sigma\Omega} \tag{25}$$

$$\left(\nabla\cdot\mathbf{q}(\theta), \delta\theta\right) = -\left(\mathbf{q}(\theta), \nabla\delta\theta\right) + \left(\overline{q}, \delta\theta\right)_{\partial_q\Omega} \tag{26}$$

and substituting (25) into (21) and (26) into (24), the mixed variational form of the quasi-static transient coupled thermo-mechanical problem can be stated as:

Find a velocity vector field $\mathbf{v} \in \mathcal{V}$, *a pressure field* $p \in \mathcal{Q}$ *and a temperature field* $\theta \in \mathcal{T}$, *such that the following equations hold in* Ω:

$$\left(p, \nabla \cdot \delta\mathbf{v}\right) + \left(\mathbf{s}\left(\mathbf{v}, \theta\right), \nabla^s \delta\mathbf{v}\right) = l_m\left(\delta\mathbf{v}\right) \quad \forall \delta\mathbf{v} \in \mathcal{V}_0 \tag{27}$$

$$\left(\nabla \cdot \mathbf{v}, \delta p\right) - \left(\frac{\partial e^{\theta}\left(\theta\right)}{\partial t}, \delta p\right) - \left(\mathbf{v} \cdot \nabla e^{\theta}\left(\theta\right), \delta p\right) = 0 \quad \forall \delta p \in \mathcal{Q} \tag{28}$$

$$\left(c_0 \frac{\partial \theta}{\partial t}, \delta\theta\right) + \left(c_0 \mathbf{v} \cdot \nabla\theta, \delta\theta\right) - \left(\mathbf{q}\left(\theta\right), \nabla\delta\theta\right) - \left(\mathcal{D}, \delta\theta\right) = l_t\left(\delta\theta\right) \quad \forall \delta\theta \in \mathcal{T}_0 \tag{29}$$

where, using a short notation, the following mechanical and thermal operators have been introduced,

$$l_m\left(\delta\mathbf{v}\right) := \left(\mathbf{f}, \delta\mathbf{v}\right) + \left(\overline{\mathbf{t}}, \delta\mathbf{v}\right)_{\partial_\sigma \Omega} \tag{30}$$

$$l_t\left(\delta\theta\right) := \left(R, \delta\theta\right) - \left(\overline{q}, \delta\theta\right)_{\partial_q \Omega} \tag{31}$$

Using the compact short notation introduced in (8)-(9), the mixed variational form of the quasi-static transient coupled thermo-mechanical problem given by (27)-(29) can be stated as:

Find a vector field $\mathbf{V} \in \mathcal{W}$, *such that the following equations hold in* Ω:

$$B\left(\mathbf{V}, \delta\mathbf{V}\right) = L\left(\delta\mathbf{V}\right) \quad \forall \delta\mathbf{V} \in \mathcal{W}_0 \tag{32}$$

where $B\left(\mathbf{V}, \delta\mathbf{V}\right)$ and $L\left(\delta\mathbf{V}\right)$ are given by,

$$\begin{aligned} B\left(\mathbf{V}, \delta\mathbf{V}\right) := {} & \left(p, \nabla \cdot \delta\mathbf{v}\right) + \left(\mathbf{s}\left(\mathbf{v}, \theta\right), \nabla^s \delta\mathbf{v}\right) + \left(\nabla \cdot \mathbf{v}, \delta p\right) - \left(\frac{\partial e^{\theta}\left(\theta\right)}{\partial t}, \delta p\right) - \\ & - \left(\mathbf{v} \cdot \nabla e^{\theta}\left(\theta\right), \delta p\right) + \left(c_0 \frac{\partial \theta}{\partial t}, \delta\theta\right) + \left(c_0 \mathbf{v} \cdot \nabla\theta, \delta\theta\right) - \left(\mathbf{q}\left(\theta\right), \nabla\delta\theta\right) - \left(\mathcal{D}, \delta\theta\right) \end{aligned} \tag{33}$$

$$L\left(\delta\mathbf{V}\right) := l_m\left(\delta\mathbf{v}\right) + l_t\left(\delta\theta\right) \tag{34}$$

2.4 *Discrete Mixed Variational Form of the Quasi-static Transient Coupled Thermo-mechanical Problem in Eulerian Form*

The standard Galerkin projection of the variational problem defined by (32) is now straightforward. Let $\mathcal{P}_h$ denote a finite element partition of the domain Ω. The diameter of an element domain $e \in \mathcal{P}_h$ is denoted by h_e and the diameter of the finite element partition is $h = \max\left\{h_e \mid e \in \mathcal{P}_h\right\}$. We can now construct conforming finite element spaces $\mathcal{V}_h \subset \mathcal{V}$, $\mathcal{Q}_h \subset \mathcal{Q}$, $\mathcal{T}_h \subset \mathcal{T}$ and $\mathcal{W}_h := \mathcal{V}_h \times \mathcal{Q}_h \times \mathcal{T}_h$ as well as $\mathcal{V}_{0,h} \subset \mathcal{V}_0$, $\mathcal{Q}_h \subset \mathcal{Q}$, $\mathcal{T}_{0,h} \subset \mathcal{T}_0$ and $\mathcal{W}_{0,h} := \mathcal{V}_{0,h} \times \mathcal{Q}_h \times \mathcal{T}_{0,h}$. In principle, functions in $\mathcal{V}_h \subset \mathcal{V}$ and $\mathcal{T}_h \subset \mathcal{T}$ are continuous, whereas functions in $\mathcal{Q}_h \subset \mathcal{Q}$ not necessarily. Likewise, the polynomial orders of these spaces may be different. Then the discrete version of (32) can be stated as:

Find a vector field $\mathbf{V}_h \in \mathcal{W}_h$, *such that the following equations hold in* Ω:

$$B\left(\mathbf{V}_h, \delta\mathbf{V}_h\right) = L\left(\delta\mathbf{V}_h\right) \quad \forall \delta\mathbf{V}_h \in \mathcal{W}_{0,h} \tag{35}$$

where $B\left(\mathbf{V}_h, \delta\mathbf{V}_h\right)$ and $L\left(\delta\mathbf{V}_h\right)$ are the spatial discrete counterpart of the continuum expressions given by (33) and (34).

2.5 *Multiscale Stabilized Discrete Mixed Variational Form of the Quasi-static Transient Coupled Thermo-mechanical Problem in Eulerian Form*

As it is well known, convenient velocity-pressure interpolations, such as linear velocity and linear pressure interpolations, turn out to violate the inf-sup Babuska-Brezzi condition. To circumvent this stability condition, within the framework of the multiscale methods, the discrete variational form $B\left(\mathbf{V}_h,\delta\mathbf{V}_h\right)$ given by (35) is replaced by a mesh-dependent stabilized discrete variational form $B_{stab}\left(\mathbf{V}_h,\delta\mathbf{V}_h\right)$ with enhanced stability properties.

Within the paradigmatic framework of the multiscale methods, introduced by Hughes *et al.* in 1998 [31], the subgrid scale method seeks to approximate the effect of the component of the continuous solution which cannot be captured by the finite element mesh used to obtain the discrete finite element solution. The unresolved component is referred to as the subgrid scale or subscale. Let $\mathcal{W}:=\mathcal{W}_h\oplus\tilde{\mathcal{W}}$, where $\tilde{\mathcal{W}}=\tilde{\mathcal{V}}\times\tilde{\mathcal{Q}}\times\tilde{\mathcal{T}}$ is any suitable space to complete $\mathcal{W}_h$ in $\mathcal{W}$. Obviously, $\tilde{\mathcal{W}}$ is an infinite-dimensional space, but once the final method is formulated, it will be approximated by a finite-dimensional space, although we will keep the same symbol for it in order to simplify the notation. We will refer to $\tilde{\mathcal{W}}$ as the space of the subgrid scales or the space of the subscales. Likewise, let $\mathcal{W}_0:=\mathcal{W}_{0,h}\oplus\tilde{\mathcal{W}}_0$, with $\tilde{\mathcal{W}}_0=\tilde{\mathcal{V}}_0\times\tilde{\mathcal{Q}}\times\tilde{\mathcal{T}}_0$ any space to complete $\mathcal{W}_{0,h}$ in $\mathcal{W}_0$. With the above definitions in hand, we consider that there exists a component $\tilde{\mathbf{V}}\in\tilde{\mathcal{W}}$ of the exact continuous solution $\mathbf{V}\in\mathcal{W}$ which cannot be captured by the solution provided by the finite element method $\mathbf{V}_h\in\mathcal{W}_h$, such that,

$$\mathbf{V}:=\mathbf{V}_h+\tilde{\mathbf{V}} \tag{36}$$

Assuming that the exact pressure can be captured by the solution provided by the finite element method and, therefore, assuming that the pressure subgrid scale is zero, the vectors $\mathbf{V}\in\mathcal{W}$, $\mathbf{V}_h\in\mathcal{W}_h$ and $\tilde{\mathbf{V}}\in\tilde{\mathcal{W}}$ take the form,

$$\mathbf{V}=\begin{bmatrix}\mathbf{v}\\ p\\ \theta\end{bmatrix},\quad \mathbf{V}_h=\begin{bmatrix}\mathbf{v}_h\\ p_h\\ \theta_h\end{bmatrix},\quad \tilde{\mathbf{V}}=\begin{bmatrix}\tilde{\mathbf{v}}\\ 0\\ \tilde{\theta}\end{bmatrix} \tag{37}$$

Using the multiscale split given by (36) the multiscale discrete variational form version of the discrete variational form given by (32) reads:

Find a vector field $\mathbf{V}_h\in\mathcal{W}_h$ *and a vector field* $\tilde{\mathbf{V}}\in\tilde{\mathcal{W}}$*, such that the following equations hold in* Ω*:*

$$B\left(\mathbf{V}_h+\tilde{\mathbf{V}},\delta\mathbf{V}_h\right)=L\left(\delta\mathbf{V}_h\right)\quad\forall\delta\mathbf{V}_h\in\mathcal{W}_{0,h} \tag{38}$$

$$B\left(\mathbf{V}_h+\tilde{\mathbf{V}},\delta\tilde{\mathbf{V}}\right)=L\left(\delta\tilde{\mathbf{V}}\right)\quad\forall\delta\tilde{\mathbf{V}}\in\tilde{\mathcal{W}}_0 \tag{39}$$

Developing the compact expressions (38) and (39), the multiscale stabilized discrete mixed variational form version of the mixed variational form given by (27)-(29) reads:

Find velocity vector fields $\mathbf{v}_h\in\mathcal{V}_h$ *and* $\tilde{\mathbf{v}}\in\tilde{\mathcal{V}}$*, pressure field* $p_h\in\mathcal{Q}_h$ *and temperature fields* $\theta_h\in\mathcal{T}_h$ *and* $\tilde{\theta}\in\tilde{\mathcal{T}}$*, such that the following equations hold in* Ω*:*

$$\left(p_h,\nabla\cdot\delta\mathbf{v}_h\right)+\left(\mathbf{s}\left(\mathbf{v}_h+\tilde{\mathbf{v}},\theta_h+\tilde{\theta}\right),\nabla^s\delta\mathbf{v}_h\right)=l_{m_h}\left(\delta\mathbf{v}_h\right)\quad\forall\delta\mathbf{v}_h\in\mathcal{V}_{0,h} \tag{40}$$

$$\left(\nabla\cdot\left(\mathbf{v}_h+\tilde{\mathbf{v}}\right),\delta p_h\right)-\left(\partial_t e^{\theta}\left(\theta_h+\tilde{\theta}\right),\delta p_h\right)-\left(\left(\mathbf{v}_h+\tilde{\mathbf{v}}\right)\cdot\nabla e^{\theta}\left(\theta_h+\tilde{\theta}\right),\delta p_h\right)=0\quad\forall\delta p_h\in\mathcal{Q}_h \tag{41}$$

$$\left(c_0\partial_t\left(\theta_h+\tilde{\theta}\right),\delta\theta_h\right)+\left(c_0\left(\mathbf{v}_h+\tilde{\mathbf{v}}\right)\cdot\nabla\left(\theta_h+\tilde{\theta}\right),\delta\theta_h\right)-\left(\mathbf{q}\left(\theta_h+\tilde{\theta}\right),\nabla\delta\theta_h\right)-\left(\mathcal{D}_h,\delta\theta_h\right)= \\ =l_{t_h}\left(\delta\theta_h\right)\quad\forall\delta\theta_h\in\mathcal{T}_{0,h} \tag{42}$$

$$\left(p_h,\nabla\cdot\delta\tilde{\mathbf{v}}\right)+\left(\mathbf{s}\left(\mathbf{v}_h+\tilde{\mathbf{v}},\theta_h+\tilde{\theta}\right),\nabla^s\delta\tilde{\mathbf{v}}\right)=l_m\left(\delta\tilde{\mathbf{v}}\right)\quad\forall\delta\tilde{\mathbf{v}}\in\tilde{\mathcal{V}}_0 \tag{43}$$

$$\left(c_0\partial_t\left(\theta_h+\tilde{\theta}\right),\delta\tilde{\theta}\right)+\left(c_0\left(\mathbf{v}_h+\tilde{\mathbf{v}}\right)\cdot\nabla\left(\theta_h+\tilde{\theta}\right),\delta\tilde{\theta}\right)-\left(\mathbf{q}\left(\theta_h+\tilde{\theta}\right),\nabla\delta\tilde{\theta}\right)-\left(\mathcal{D}_h,\delta\tilde{\theta}\right)= \\ =l_{t_h}\left(\delta\tilde{\theta}\right)\quad\forall\delta\tilde{\theta}\in\tilde{\mathcal{T}}_0 \tag{44}$$

where the following mechanical and thermal spatial discretized operators have been introduced,

$$l_{m_h}\left(\delta\mathbf{v}_h\right):=\left(\mathbf{f}_h,\delta\mathbf{v}_h\right)+\left(\overline{\mathbf{t}}_h,\delta\mathbf{v}_h\right)_{\partial_\sigma\Omega},\quad l_{t_h}\left(\delta\theta_h\right):=\left(R_h,\delta\theta_h\right)-\left(\overline{q}_h,\delta\theta_h\right)_{\partial_q\Omega} \tag{45}$$

$$l_{m_h}\left(\delta\tilde{\mathbf{v}}\right):=\left(\mathbf{f}_h,\delta\tilde{\mathbf{v}}\right)+\left(\overline{\mathbf{t}}_h,\delta\tilde{\mathbf{v}}\right)_{\partial_\sigma\Omega},\quad l_{t_h}\left(\delta\tilde{\theta}\right):=\left(R_h,\delta\tilde{\theta}\right)-\left(\overline{q}_h,\delta\tilde{\theta}\right)_{\partial_q\Omega} \tag{46}$$

Using a full-implicit Backward-Euler time integration scheme, the time discrete version of the multiscale stabilized discrete variational form given by (38)-(39) reads:

Find a vector field $\mathbf{V}_{h,n+1}\in\mathcal{W}_h$ *and a vector field* $\tilde{\mathbf{V}}_{n+1}\in\tilde{\mathcal{W}}$, *such that the following equations hold in* Ω*:*

$$B\left(\mathbf{V}_{h,n+1}+\tilde{\mathbf{V}}_{n+1},\delta\mathbf{V}_h\right)=L\left(\delta\mathbf{V}_h\right)\quad\forall\delta\mathbf{V}_h\in\mathcal{W}_{0,h} \tag{47}$$

$$B\left(\mathbf{V}_{h,n+1}+\tilde{\mathbf{V}}_{n+1},\delta\tilde{\mathbf{V}}\right)=L\left(\delta\tilde{\mathbf{V}}\right)\quad\forall\delta\tilde{\mathbf{V}}\in\tilde{\mathcal{W}}_0 \tag{48}$$

The idea now is to estimate a solution for (48) by finding a discrete approximate solution for the subgrid scale field $\tilde{\mathbf{V}}_{n+1}\in\tilde{\mathcal{W}}$ and substituting this approximation into (47).

Developing the compact expressions (47) and (48), the time discrete multiscale stabilized discrete variational form version of the multiscale stabilized discrete variational form given by (40)-(44) reads:

Find velocity vector fields $\mathbf{v}_{h,n+1}\in\mathcal{V}_h$ *and* $\tilde{\mathbf{v}}_{n+1}\in\tilde{\mathcal{V}}$, *pressure field* $p_{h,n+1}\in\mathcal{Q}_h$ *and temperature fields* $\theta_{h,n+1}\in\mathcal{T}_h$ *and* $\tilde{\theta}_{n+1}\in\tilde{\mathcal{T}}$, *such that the following equations hold in* Ω*:*

$$\left(p_{h,n+1},\nabla\cdot\delta\mathbf{v}_h\right)+\left(\mathbf{s}\left(\mathbf{v}_{h,n+1}+\tilde{\mathbf{v}}_{n+1},\theta_{h,n+1}+\tilde{\theta}_{n+1}\right),\nabla^s\delta\mathbf{v}_h\right)=l_{m_{h,n+1}}\left(\delta\mathbf{v}_h\right)\quad\forall\delta\mathbf{v}_h\in\mathcal{V}_{0,h} \tag{49}$$

$$\left(\nabla\cdot\mathbf{v}_{h,n+1},\delta p_h\right)-\left(\frac{1}{\Delta t}\left(e^\theta\left(\theta_{h,n+1}+\tilde{\theta}_{n+1}\right)-e^\theta\left(\theta_{h,n}+\tilde{\theta}_n\right)\right),\delta p_h\right)-\left(\mathbf{v}_{h,n+1}\cdot\nabla e^\theta\left(\theta_{h,n+1}+\tilde{\theta}_{n+1}\right),\delta p_h\right)+ \\ +\left(\nabla\cdot\tilde{\mathbf{v}}_{n+1},\delta p_h\right)-\left(\tilde{\mathbf{v}}_{n+1}\cdot\nabla e^\theta\left(\theta_{h,n+1}+\tilde{\theta}_{n+1}\right),\delta p_h\right)=0\quad\forall\delta p_h\in\mathcal{Q}_h \tag{50}$$

$$\left(\frac{c_0}{\Delta t}\left(\theta_{h,n+1}-\theta_{h,n}+\tilde{\theta}_{n+1}-\tilde{\theta}_n\right),\delta\theta_h\right)+\left(c_0\left(\mathbf{v}_{h,n+1}+\tilde{\mathbf{v}}_{n+1}\right)\cdot\nabla\left(\theta_{h,n+1}+\tilde{\theta}_{n+1}\right),\delta\theta_h\right)- \\ -\left(\mathbf{q}\left(\theta_{h,n+1}+\tilde{\theta}_{n+1}\right),\nabla\delta\theta_h\right)-\left(\mathcal{D}_{h,n+1},\delta\theta_h\right)=l_{t_{h,n+1}}\left(\delta\theta_h\right)\quad\forall\delta\theta_h\in\mathcal{T}_{0,h} \tag{51}$$

$$\left(p_{h,n+1},\nabla\cdot\delta\tilde{\mathbf{v}}\right)+\left(\mathbf{s}\left(\mathbf{v}_{h,n+1}+\tilde{\mathbf{v}}_{n+1},\theta_{h,n+1}\right),\nabla^s\delta\tilde{\mathbf{v}}\right)=l_{m_{h,n+1}}\left(\delta\tilde{\mathbf{v}}\right)\quad\forall\delta\tilde{\mathbf{v}}\in\tilde{\mathcal{V}}_0 \tag{52}$$

$$\left(\frac{c_0}{\Delta t}\left(\theta_{h,n+1}-\theta_{h,n}+\tilde{\theta}_{n+1}-\tilde{\theta}_n\right),\delta\tilde{\theta}\right)+\left(c_0\left(\mathbf{v}_{h,n+1}+\tilde{\mathbf{v}}_{n+1}\right)\cdot\nabla\left(\theta_{h,n+1}+\tilde{\theta}_{n+1}\right),\delta\tilde{\theta}\right)- \\ -\left(\mathbf{q}\left(\theta_{h,n+1}+\tilde{\theta}_{n+1}\right),\nabla\delta\tilde{\theta}\right)-\left(\mathcal{D}_{h,n+1},\delta\tilde{\theta}\right)=l_{t_{h,n+1}}\left(\delta\tilde{\theta}\right)\quad\forall\delta\tilde{\theta}\in\tilde{\mathcal{T}}_0 \tag{53}$$

where the following time discrete version of the mechanical and thermal spatial discretized operators given by (45) and (46) have been introduced,

$$l_{m_{h,n+1}}\left(\delta\mathbf{v}_h\right) := \left(\mathbf{f}_{h,n+1},\delta\mathbf{v}_h\right)+\left(\overline{\mathbf{t}}_{h,n+1},\delta\mathbf{v}_h\right)_{\partial_\sigma\Omega},\quad l_{t_{h,n+1}}\left(\delta\theta_h\right) := \left(R_{h,n+1},\delta\theta_h\right)-\left(\overline{q}_{h,n+1},\delta\theta_h\right)_{\partial_q\Omega} \tag{54}$$

$$l_{m_{h,n+1}}\left(\delta\tilde{\mathbf{v}}\right) := \left(\mathbf{f}_{h,n+1},\delta\tilde{\mathbf{v}}\right)+\left(\overline{\mathbf{t}}_{h,n+1},\delta\tilde{\mathbf{v}}\right)_{\partial_\sigma\Omega},\quad l_{t_{h,n+1}}\left(\delta\tilde{\theta}\right) := \left(R_{h,n+1},\delta\tilde{\theta}\right)-\left(\overline{q}_{h,n+1},\delta\tilde{\theta}\right)_{\partial_q\Omega} \tag{55}$$

2.5.1 Mechanical and thermal constitutive equations for the subgrid scales at the element level

Performing a Taylor series expansion of the exact deviatoric part of the stress tensor $\mathbf{s}\left(\mathbf{v}_{h,n+1}+\tilde{\mathbf{v}}_{n+1},\theta_{h,n+1}+\tilde{\theta}_{n+1}\right)$ around the symmetric part of the spatial gradient velocity and the temperature fields provided by the finite element solution, the exact deviatoric stress tensor can be split as [1, 2],

$$\mathbf{s}\left(\mathbf{v}_{h,n+1}+\tilde{\mathbf{v}}_{n+1},\theta_{h,n+1}+\tilde{\theta}_{n+1}\right) := \mathbf{s}_{h,n+1}+\tilde{\mathbf{s}}_{n+1} \tag{56}$$

where

$$\mathbf{s}_{h,n+1} := \mathbf{s}\left(\mathbf{v}_{h,n+1},\theta_{h,n+1}\right) \tag{57}$$

$$\tilde{\mathbf{s}}_{n+1} := D\mathbf{s}\left(\mathbf{v}_{h,n+1},\theta_{h,n+1}\right)\cdot dev\left(\nabla^s\tilde{\mathbf{v}}_{n+1}\right)+D\mathbf{s}\left(\mathbf{v}_{h,n+1},\theta_{h,n+1}\right)\cdot\tilde{\theta}_{n+1} \tag{58}$$

Here the following uncoupled approximation is considered for the constitutive mechanical subgrid scale equation

$$\tilde{\mathbf{s}}_{n+1} := 2\tilde{\mu}_{n+1}\,dev\left(\nabla^s\tilde{\mathbf{v}}_{n+1}\right) \tag{59}$$

where $\tilde{\mu}_{n+1}$ is the secant viscosity defined as,

$$\tilde{\mu}_{n+1} := \frac{\left\|\mathbf{s}_{h,n+1}\right\|}{2\left\|dev\left(\nabla^s\mathbf{v}_{h,n+1}\right)\right\|} \tag{60}$$

and then the deviatoric subgrid scale stress tensor takes the form,

$$\tilde{\mathbf{s}}_{n+1} := 2\tilde{\mu}_{n+1}\,dev\left(\nabla^s\tilde{\mathbf{v}}_{n+1}\right) := \frac{\left\|\mathbf{s}_{h,n+1}\right\|}{\left\|dev\left(\nabla^s\mathbf{v}_{h,n+1}\right)\right\|}dev\left(\nabla^s\tilde{\mathbf{v}}_{n+1}\right) \tag{61}$$

REMARK 1. *Note that using time discrete counterpart of the rigid-plastic Norton-Hoff constitutive model given by (10), substituting (10) into (61), the following relationship holds* $\tilde{\mu}_{n+1} := \frac{1}{2}K\left(\theta_{h,n+1}\right)\left(\sqrt{3}\dot{\bar{\varepsilon}}_{h,n+1}\right)^{m\left(\theta_{h,n+1}\right)-1}$

REMARK 2. *Note that using time discrete counterpart of the rigid-plastic Sheppard-Wright constitutive model given by (13), substituting (13) into (61), the following relationship holds* $\tilde{\mu}_{n+1} := \mu\left(\dot{\bar{\varepsilon}}_{h,n+1},\theta_{h,n+1}\right)$

Analogously, performing a Taylor series expansion of the exact heat flux per unit of surface $\mathbf{q}\left(\theta_{h,n+1}+\tilde{\theta}_{n+1}\right)$ around the spatial gradient temperature field provided by the finite element solution, the exact heat transfer per unit of surface can be splitted as,

$$\mathbf{q}\left(\theta_{h,n+1}+\tilde{\theta}_{n+1}\right) := \mathbf{q}_{h,n+1}+\tilde{\mathbf{q}}_{n+1} \tag{62}$$

where

$$\mathbf{q}_{h,n+1} := \mathbf{q}\left(\theta_{h,n+1}\right) \tag{63}$$

$$\tilde{\mathbf{q}}_{n+1} := D\mathbf{q}\left(\theta_{h,n+1}\right)\cdot\nabla\tilde{\theta}_{n+1} \tag{64}$$

Here the following approximation is considered for the constitutive thermal subgrid scale equation

$$\tilde{\mathbf{q}}_{n+1} := -\tilde{k}_{n+1}\nabla\tilde{\theta}_{n+1} \tag{65}$$

where $\tilde{k}_{n+1}$ is defined as,

$$\tilde{k}_{n+1} := c_0 \left\|\mathbf{v}_{h,n+1}\right\| h_s \tag{66}$$

where h_s is the streamline characteristic length, which gives a measure of the mesh element size in the direction of the velocity field. Then the heat flux associated to the thermal subgrid scale takes the form,

$$\tilde{\mathbf{q}}_{n+1} := -\tilde{k}_{n+1}\nabla\tilde{\theta}_{n+1} := -c_0 \left\|\mathbf{v}_{h,n+1}\right\| h_s \nabla\tilde{\theta}_{n+1} \tag{67}$$

Furthermore, performing a Taylor series expansion of the exact volumetric thermal strain $e^\theta\left(\theta_{h,n+1}+\tilde{\theta}_{n+1}\right)$ around the temperature field provided by the finite element solution, the exact volumetric thermal strain can be splitted as,

$$e^\theta\left(\theta_{h,n+1}+\tilde{\theta}_{n+1}\right) := e^\theta_{h,n+1} + \tilde{e}^\theta_{h,n+1}, \quad e^\theta\left(\theta_{h,n}+\tilde{\theta}_{n}\right) := e^\theta_{h,n} + \tilde{e}^\theta_{h,n} \tag{68}$$

where

$$e^\theta_{h,n+1} := e^\theta\left(\theta_{h,n+1}\right), \quad e^\theta_{h,n} := e^\theta\left(\theta_{h,n}\right) \tag{69}$$

$$\tilde{e}^\theta_{h,n+1} := De^\theta\left(\theta_{h,n+1}\right)\cdot\tilde{\theta}_{n+1}, \quad \tilde{e}^\theta_{h,n} := De^\theta\left(\theta_{h,n}\right)\cdot\tilde{\theta}_{n} \tag{70}$$

Using the splits introduced in (56), (62) and (68) and substituting in (49)-(53) the time discrete multiscale stabilized discrete variational form given by (49)-(53) reads:

Find velocity vector fields $\mathbf{v}_{h,n+1}\in\mathcal{V}_h$ *and* $\tilde{\mathbf{v}}_{n+1}\in\tilde{\mathcal{V}}$, *pressure field* $p_{h,n+1}\in\mathcal{Q}_h$ *and temperature fields* $\theta_{h,n+1}\in\mathcal{T}_h$ *and* $\tilde{\theta}_{n+1}\in\tilde{\mathcal{T}}$, *such that the following equations hold in* Ω*:*

$$\left(p_{h,n+1},\nabla\cdot\delta\mathbf{v}_h\right)+\left(\mathbf{s}_{h,n+1},\nabla^s\delta\mathbf{v}_h\right)+\left(\tilde{\mathbf{s}}_{n+1},\nabla^s\delta\mathbf{v}_h\right)=l_{m_{h,n+1}}\left(\delta\mathbf{v}_h\right)\quad\forall\delta\mathbf{v}_h\in\mathcal{V}_{0,h} \tag{71}$$

$$\begin{aligned}&\left(\nabla\cdot\mathbf{v}_{h,n+1}-\frac{1}{\Delta t}\left(e^\theta_{h,n+1}-e^\theta_{h,n}\right)-\mathbf{v}_{h,n+1}\cdot\nabla e^\theta_{h,n+1},\delta p_h\right)-\left(\frac{1}{\Delta t}\left(\tilde{e}^\theta_{h,n+1}-\tilde{e}^\theta_{h,n}\right)+\mathbf{v}_{h,n+1}\cdot\nabla\tilde{e}^\theta_{h,n+1},\delta p_h\right)+\\&+\left(\nabla\cdot\tilde{\mathbf{v}}_{n+1}-\tilde{\mathbf{v}}_{n+1}\cdot\nabla e^\theta_{h,n+1}-\tilde{\mathbf{v}}_{n+1}\cdot\nabla\tilde{e}^\theta_{h,n+1},\delta p_h\right)=0\quad\forall\delta p_h\in\mathcal{Q}_h\end{aligned} \tag{72}$$

$$\begin{aligned}&\left(\frac{c_0}{\Delta t}\left(\theta_{h,n+1}-\theta_{h,n}\right)+c_0\mathbf{v}_{h,n+1}\cdot\nabla\theta_{h,n+1},\delta\theta_h\right)+\left(\frac{c_0}{\Delta t}\left(\tilde{\theta}_{n+1}-\tilde{\theta}_{n}\right)+c_0\mathbf{v}_{h,n+1}\cdot\nabla\tilde{\theta}_{n+1},\delta\theta_h\right)+\\&+\left(c_0\tilde{\mathbf{v}}_{n+1}\cdot\nabla\theta_{h,n+1},\delta\theta_h\right)+\left(c_0\tilde{\mathbf{v}}_{n+1}\cdot\nabla\tilde{\theta}_{n+1},\delta\theta_h\right)-\\&-\left(\mathbf{q}_{h,n+1},\nabla\delta\theta_h\right)-\left(\tilde{\mathbf{q}}_{n+1},\nabla\delta\theta_h\right)-\left(\mathcal{D}_{h,n+1},\delta\theta_h\right)=l_{t_{h,n+1}}\left(\delta\theta_h\right)\quad\forall\delta\theta_h\in\mathcal{T}_{0,h}\end{aligned} \tag{73}$$

$$\left(p_{h,n+1},\nabla\cdot\delta\tilde{\mathbf{v}}\right)+\left(\mathbf{s}_{h,n+1},\nabla^s\delta\tilde{\mathbf{v}}\right)+\left(\tilde{\mathbf{s}}_{n+1},\nabla^s\delta\tilde{\mathbf{v}}\right)=l_{m_{h,n+1}}\left(\delta\tilde{\mathbf{v}}\right)\quad\forall\delta\tilde{\mathbf{v}}\in\tilde{\mathcal{V}}_0 \tag{74}$$

$$\begin{aligned}&\left(\frac{c_0}{\Delta t}\left(\theta_{h,n+1}-\theta_{h,n}\right),\delta\tilde{\theta}\right)+\left(c_0\mathbf{v}_{h,n+1}\cdot\nabla\theta_{h,n+1},\delta\tilde{\theta}\right)+\left(c_0\mathbf{v}_{h,n+1}\cdot\nabla\tilde{\theta}_{n+1},\delta\tilde{\theta}\right)+\\&+\left(\frac{c_0}{\Delta t}\left(\tilde{\theta}_{n+1}-\tilde{\theta}_{n}\right),\delta\tilde{\theta}\right)+\left(c_0\tilde{\mathbf{v}}_{n+1}\cdot\nabla\theta_{h,n+1},\delta\tilde{\theta}\right)+\left(c_0\tilde{\mathbf{v}}_{n+1}\cdot\nabla\tilde{\theta}_{n+1},\delta\tilde{\theta}\right)-\\&-\left(\mathbf{q}_{h,n+1},\nabla\delta\tilde{\theta}\right)-\left(\tilde{\mathbf{q}}_{n+1},\nabla\delta\tilde{\theta}\right)-\left(\mathcal{D}_{h,n+1},\delta\tilde{\theta}\right)=l_{t_{h,n+1}}\left(\delta\tilde{\theta}\right)\quad\forall\delta\tilde{\theta}\in\tilde{\mathcal{T}}_0\end{aligned} \tag{75}$$

The goals now are twofold. First, to find an approximate solution for the velocitiy and temperature subgrid scales (remember that the pressure subgrid scale has been assumed to be zero) within the infinite-dimensional variational problem given by (74) and (75). For this, the

infinite-dimensional space of the subgrid scales will be approximated by a finite-dimensional space. Secondly, to substitute the approximate solution for the velocity and temperature subgrid scales into the finite dimensional variational problem given by (71)-(73).

2.5.2 *Velocity and temperature subgrid scales at the element level*

Velocity subgrid scale. Integrating by parts within each element the first two terms on the left-hand-side of (74) and taking into account the equilibrium of tractions at the interelement boundaries yields,

$$\sum_{e=1}^{nelem}\left(\tilde{\mathbf{s}}_{n+1},\nabla^s\delta\tilde{\mathbf{v}}\right)\Big|_{\Omega_e}=\sum_{e=1}^{nelem}\left(\nabla p_{h,n+1}+\nabla\cdot\mathbf{s}_{h,n+1}+\mathbf{f}_{h,n+1},\delta\tilde{\mathbf{v}}\right)\Big|_{\Omega_e}\quad\forall\delta\tilde{\mathbf{v}}\in\tilde{\mathcal{V}}_0 \tag{76}$$

Using the mechanical constitutive equation for the subgrid scale given by (61), the following approximation, at the element level, for the term on the left-hand-side in (76) is considered,

$$\left(\tilde{\mathbf{s}}_{n+1},\nabla^s\delta\tilde{\mathbf{v}}\right)\Big|_{\Omega_e}:=\left(2\tilde{\mu}_{n+1}dev\left(\nabla^s\tilde{\mathbf{v}}_{n+1}\right),\nabla^s\delta\tilde{\mathbf{v}}\right)\Big|_{\Omega_e}=\left(\left(\tau_{e,n+1}^{(1)}\right)^{-1}\tilde{\mathbf{v}}_{n+1},\delta\tilde{\mathbf{v}}\right)\Big|_{\Omega_e}\quad\forall\delta\tilde{\mathbf{v}}\in\tilde{\mathcal{V}}_0 \tag{77}$$

where $\tau_{e,n+1}^{(1)}$ is a mesh-dependent scalar stabilization parameter defined at the element level as,

$$\tau_{e,n+1}^{(1)}:=\frac{c_1h^2}{2\tilde{\mu}_{n+1}}:=\frac{c_1h^2\left\|dev\left(\nabla^s\mathbf{v}_{h,n+1}\right)\right\|}{\left\|\mathbf{s}_{h,n+1}\right\|} \tag{78}$$

where c_1 is a constant and h denotes a measure of the mesh element size.

Then using (76) and (77), the following variational approximation for the velocity subgrid scale at the element level holds,

$$\left(\tilde{\mathbf{v}}_{n+1},\delta\tilde{\mathbf{v}}\right)\Big|_{\Omega_e}=\left(\tau_{e,n+1}^{(1)}\left(\nabla p_{h,n+1}+\nabla\cdot\mathbf{s}_{h,n+1}+\mathbf{f}_{h,n+1}\right),\delta\tilde{\mathbf{v}}\right)\Big|_{\Omega_e}\quad\forall\delta\tilde{\mathbf{v}}\in\tilde{\mathcal{V}}_0 \tag{79}$$

Then the velocity subgrid scale can be approximated as,

$$\tilde{\mathbf{v}}_{n+1}\Big|_{\Omega_e}=\tau_{e,n+1}^{(1)}\left(\nabla p_{h,n+1}+\nabla\cdot\mathbf{s}_{h,n+1}+\mathbf{f}_{h,n+1}\right)\Big|_{\Omega_e}+\tilde{\mathbf{v}}_{n+1}^{\perp}\Big|_{\Omega_e} \tag{80}$$

where $\tilde{\mathbf{v}}_{n+1}^{\perp}$ belongs to the orthogonal velocity subgrid scale space $\tilde{\mathcal{V}}^{\perp}$. Different choices are available for the approximation of the velocity subgrid scale, depending on the expression chosen for $\tilde{\mathbf{v}}_{n+1}^{\perp}$. Here the following two options, leading to the Algebraic Subgrid Scale (ASGS) and Orthogonal Subgrid Scale (OSGS) methods, will be considered.

(i) Algebraic Subgrid Scale (ASGS) method. Within the ASGS method we take $\tilde{\mathbf{v}}_{n+1}^{\perp}=\mathbf{0}$ and then the velocity subgrid scale at the element level are given by,

$$\tilde{\mathbf{v}}_{n+1}\Big|_{\Omega_e}=\tau_{e,n+1}^{(1)}\left(\nabla p_{h,n+1}+\nabla\cdot\mathbf{s}_{h,n+1}+\mathbf{f}_{h,n+1}\right)\Big|_{\Omega_e} \tag{81}$$

For linear elements the deviatoric part of the stress tensor is constant within the elements and, therefore, its divergence is zero. Furthermore, if we neglect the contribution of the body forces on the velocity subgrid scale, the Galerkin Least-Squares (GLS) method can be recovered as a particular case of the ASGS method, taking,

$$\tilde{\mathbf{v}}_{n+1}\Big|_{\Omega_e}=\tau_{e,n+1}^{(1)}\nabla p_{h,n+1}\Big|_{\Omega_e} \tag{82}$$

(ii) Orthogonal Subgrid Scale (OSGS) method. Within the OSGS method proposed by Codina (2000, 2002) [15, 16], we take,

$$\tilde{\mathbf{v}}_{n+1}^{\perp}\Big|_{\Omega_e}=-\tau_{e,n+1}^{(1)}P_h\left(\nabla p_{h,n+1}+\nabla\cdot\mathbf{s}_{h,n+1}+\mathbf{f}_{h,n+1}\right)\Big|_{\Omega_e} \tag{83}$$

where $P_h(\bullet)$ is the $L_2(\bullet)$ projection operator onto $\mathcal{W}_h$. Then the velocity subgrid scale at the element level are given by,

$$\tilde{\mathbf{v}}_{n+1}\big|_{\Omega_e} = \tau^{(1)}_{e,n+1} P^{\perp}_h \left(\nabla p_{h,n+1} + \nabla \cdot \mathbf{s}_{h,n+1} + \mathbf{f}_{h,n+1} \right)\Big|_{\Omega_e} \tag{84}$$

where $P^{\perp}_h(\bullet)$ is the $L_2(\bullet)$ projection operator onto $\mathcal{W}^{\perp}_h$ defined as $P^{\perp}_h(\bullet) = (\bullet) - P_h(\bullet)$. Note that with this definition we are implicitly assuming that $\tilde{\mathcal{V}} := \mathcal{V}^{\perp}_h$ and, therefore, that the velocity subgrid scale space is orthogonal to the velocity finite element space.

Assuming that the body forces belong to the finite element space $\mathcal{W}_h$, then we get,

$$\tilde{\mathbf{v}}_{n+1}\big|_{\Omega_e} = \tau^{(1)}_{e,n+1} P^{\perp}_h \left(\nabla p_{h,n+1} + \nabla \cdot \mathbf{s}_{h,n+1} \right)\Big|_{\Omega_e} \tag{85}$$

Furthermore, for linear elements the deviatoric part of the stress tensor is constant within the elements and therefore its divergence is zero within an element, yielding the following approximation for the velocity subgrid scale,

$$\tilde{\mathbf{v}}_{n+1}\big|_{\Omega_e} = \tau^{(1)}_{e,n+1} P^{\perp}_h \left(\nabla p_{h,n+1} \right)\Big|_{\Omega_e} \tag{86}$$

Temperature subgrid scale. Integrating by parts within each element the heat flux term on the left-hand-side of (75) and taking into account the equilibrium of heat fluxes at the interelement boundaries yields,

$$\begin{aligned} &\sum_{e=1}^{nelem} \left(\tilde{\mathbf{q}}_{n+1}, \nabla \delta\tilde{\theta} \right)\Big|_{\Omega_e} = \\ &+ \sum_{e=1}^{nelem} \left(\nabla \cdot \mathbf{q}_{h,n+1} - \mathcal{D}_{h,n+1} - R_{h,n+1} + \frac{c_0}{\Delta t}\left(\theta_{h,n+1} - \theta_{h,n} \right) + c_0 \mathbf{v}_{h,n+1} \cdot \nabla \theta_{h,n+1}, \delta\tilde{\theta} \right)\Big|_{\Omega_e} + \\ &+ \sum_{e=1}^{nelem} \left(\frac{c_0}{\Delta t}\left(\tilde{\theta}_{n+1} - \tilde{\theta}_n \right) + c_0 \mathbf{v}_{h,n+1} \cdot \nabla \tilde{\theta}_{n+1} + c_0 \tilde{\mathbf{v}}_{n+1} \cdot \nabla \left(\theta_{h,n+1} + \tilde{\theta}_{n+1} \right), \delta\tilde{\theta} \right)\Big|_{\Omega_e} \qquad \forall \delta\tilde{\theta} \in \tilde{\mathcal{T}} \end{aligned} \tag{87}$$

Using the thermal constitutive equation for the subgrid scale given by (67), the following approximation at the element level for the term on the left-hand-side in (87) is considered,

$$\left(\tilde{\mathbf{q}}_{n+1}, \nabla \delta\tilde{\theta} \right)\Big|_{\Omega_e} = \left(-\tilde{k}_{n+1} \nabla \tilde{\theta}_{n+1}, \nabla \delta\tilde{\theta} \right)\Big|_{\Omega_e} = -\left(\left(\tau^{(2)}_{e,n+1} \right)^{-1} \tilde{\theta}_{n+1}, \delta\tilde{\theta} \right)\Big|_{\Omega_e} \qquad \forall \delta\tilde{\theta} \in \tilde{\mathcal{T}}_0 \tag{88}$$

where $\tau^{(2)}_{e,n+1}$ is a mesh-dependent scalar stabilization parameter defined at the element level as,

$$\tau^{(2)}_{e,n+1} := \frac{c_2 h_s^2}{\tilde{k}_{n+1}} = \frac{c_2 h_s}{c_0 \left\| \mathbf{v}_{h,n+1} \right\|} \tag{89}$$

where h_s denotes the streamline characteristic length of the element, which is computed as the maximum projection of the element side vectors on the direction of the normalized velocity vector field, and for linear tetrahedral elements is given by,

$$h_s := \max \left(\left(\mathbf{x}_j - \mathbf{x}_i \right) \cdot \frac{\mathbf{v}_{h,n+1}}{\left\| \mathbf{v}_{h,n+1} \right\|} \right) \quad \forall\, i, j = 1, .., nnode \tag{90}$$

and c_2 is defined in terms of the Peclet number Pe as,

$$c_2 := \coth Pe - \frac{1}{Pe} \tag{91}$$

where the Peclet number is given by,

$$Pe = \frac{c_0 \left\| \mathbf{v}_{h,n+1} \right\| h_s}{k_{h,n+1}} \tag{92}$$

where $k_{h,n+1}$ is the time discrete thermal conductivity at time n+1.

REMARK 3. *Note that substituting the definition of the Peclet number Pe given by (92), into the expression of the subgrid scale conductivity given by (66), the following relationship holds* $\tilde{k}_{n+1} = Pe \cdot k_{h,n+1}$.

Using (87) and (88), the following variational approximation for the temperature subgrid scale at the element level holds,

$$\begin{aligned} \left(\tilde{\theta}_{n+1}, \delta\tilde{\theta} \right)\Big|_{\Omega_e} &= \left(\tau^{(2)}_{e,n+1} \left(-\nabla \cdot \mathbf{q}_{h,n+1} + \mathcal{D}_{h,n+1} + R_{h,n+1} - \frac{c_0}{\Delta t}\left(\theta_{h,n+1} - \theta_{h,n} \right) - c_0 \mathbf{v}_{h,n+1} \cdot \nabla \theta_{h,n+1} \right), \delta\tilde{\theta} \right)\Big|_{\Omega_e} - \\ &- \left(\tau^{(2)}_{e,n+1} \left(\frac{c_0}{\Delta t}\left(\tilde{\theta}_{n+1} - \tilde{\theta}_n \right) + c_0 \mathbf{v}_{h,n+1} \cdot \nabla \tilde{\theta}_{n+1} + c_0 \tilde{\mathbf{v}}_{n+1} \cdot \nabla \left(\theta_{h,n+1} + \tilde{\theta}_{n+1} \right) \right), \delta\tilde{\theta} \right)\Big|_{\Omega_e} \qquad \forall \delta\tilde{\theta} \in \tilde{\mathcal{I}}_0 \end{aligned} \tag{93}$$

Neglecting the contribution of the temperature subgrid scale on the transient and convective terms, yields,

$$\begin{aligned} \left(\tilde{\theta}_{n+1}, \delta\tilde{\theta} \right)\Big|_{\Omega_e} &= \left(\tau^{(2)}_{e,n+1} \left(-\nabla \cdot \mathbf{q}_{h,n+1} + \mathcal{D}_{h,n+1} + R_{h,n+1} - \frac{c_0}{\Delta t}\left(\theta_{h,n+1} - \theta_{h,n} \right) - c_0 \mathbf{v}_{h,n+1} \cdot \nabla \theta_{h,n+1} \right), \delta\tilde{\theta} \right)\Big|_{\Omega_e} - \\ &- \left(\tau^{(2)}_{e,n+1} c_0 \tilde{\mathbf{v}}_{n+1} \cdot \nabla \theta_{h,n+1}, \delta\tilde{\theta} \right)\Big|_{\Omega_e} \qquad \forall \delta\tilde{\theta} \in \tilde{\mathcal{I}}_0 \end{aligned} \tag{94}$$

Then the temperature subgrid scale can be approximated at the element level as,

$$\begin{aligned} \tilde{\theta}_{n+1}\Big|_{\Omega_e} &:= \tau^{(2)}_{e,n+1} \left(-\nabla \cdot \mathbf{q}_{h,n+1} + \mathcal{D}_{h,n+1} + R_{h,n+1} - \frac{c_0}{\Delta t}\left(\theta_{h,n+1} - \theta_{h,n} \right) - c_0 \left(\mathbf{v}_{h,n+1} + \tilde{\mathbf{v}}_{n+1} \right) \cdot \nabla \theta_{h,n+1} \right)\Big|_{\Omega_e} + \\ &+ \tilde{\theta}^{\perp}_{n+1}\Big|_{\Omega_e} \end{aligned} \tag{95}$$

where $\tilde{\theta}^{\perp}_{n+1}$ belongs to the orthogonal temperature subgrid scale space $\tilde{\mathcal{I}}^{\perp}$. Different choices are available for the approximation of the temperatures subgrid scale, depending on the expression chosen for $\tilde{\theta}^{\perp}_{n+1}$. Here the following two options, leading to the Algebraic Subgrid Scale (ASGS) and Orthogonal Subgrid Scale (OSGS) methods, will be considered.

(i) Algebraic Subgrid Scale (ASGS) method. Within the ASGS method we take $\tilde{\theta}^{\perp}_{n+1} = 0$ and then the temperature subgrid scale at the element level are given by,

$$\tilde{\theta}_{n+1}\Big|_{\Omega_e} := \tau^{(2)}_{e,n+1} \left(-\nabla \cdot \mathbf{q}_{h,n+1} + \mathcal{D}_{h,n+1} + R_{h,n+1} - \frac{c_0}{\Delta t}\left(\theta_{h,n+1} - \theta_{h,n} \right) - c_0 \left(\mathbf{v}_{h,n+1} + \tilde{\mathbf{v}}_{n+1} \right) \cdot \nabla \theta_{h,n+1} \right)\Big|_{\Omega_e} \tag{96}$$

For linear elements the heat flux is constant within the elements and, therefore, its divergence is zero. Furthermore, if we neglect the contributions coming from the dissipation rate, the heat source rate, the transient term and the contribution of the velocity subgrid scale to the convective term, the Streamline Upwind/Petrov-Galerkin (SUPG) method can be recovered as a particular case of the ASGS method, taking,

$$\tilde{\theta}_{n+1}\Big|_{\Omega_e} := -\tau^{(2)}_{e,n+1} c_0 \mathbf{v}_{h,n+1} \cdot \nabla \theta_{h,n+1}\Big|_{\Omega_e} \tag{97}$$

(ii) Orthogonal Subgrid Scale (OSGS) method. Within the OSGS method proposed by Codina (2000, 2002) [15, 16], we take,

$$\tilde{\theta}^{\perp}_{n+1}\big|_{\Omega_e} := -\tau^{(2)}_{e,n+1} P_h \left(-\nabla\cdot\mathbf{q}_{h,n+1} + \mathcal{D}_{h,n+1} + R_{h,n+1} - \frac{c_0}{\Delta t}\left(\theta_{h,n+1}-\theta_{h,n}\right) - c_0\left(\mathbf{v}_{h,n+1}+\tilde{\mathbf{v}}_{n+1}\right)\cdot\nabla\theta_{h,n+1}\right)\Big|_{\Omega_e} \tag{98}$$

where $P_h(\bullet)$ is the $L_2(\bullet)$ projection operator onto $\mathcal{W}_h$. Then the temperature subgrid scale at the element level are given by,

$$\tilde{\theta}_{n+1}\big|_{\Omega_e} := \tau^{(2)}_{e,n+1} P^{\perp}_h \left(-\nabla\cdot\mathbf{q}_{h,n+1} + \mathcal{D}_{h,n+1} + R_{h,n+1} - \frac{c_0}{\Delta t}\left(\theta_{h,n+1}-\theta_{h,n}\right) - c_0\left(\mathbf{v}_{h,n+1}+\tilde{\mathbf{v}}_{n+1}\right)\cdot\nabla\theta_{h,n+1}\right)\Big|_{\Omega_e} \tag{99}$$

where $P^{\perp}_h(\bullet)$ is the $L_2(\bullet)$ projection operator onto $\mathcal{W}^{\perp}_h$ defined as $P^{\perp}_h(\bullet) = (\bullet) - P_h(\bullet)$. Note that with this definition we are implicitly assuming that $\tilde{\mathcal{T}} := \mathcal{T}^{\perp}_h$ and, therefore, that the temperature subgrid scale space is orthogonal to the temperature finite element space.

Assuming that the dissipation rate, heat source rate and transient term belong to the finite element space and neglecting the contribution from the velocity subgrid scale, we get,

$$\tilde{\theta}_{n+1}\big|_{\Omega_e} := \tau^{(2)}_{e,n+1} P^{\perp}_h \left(-\nabla\cdot\mathbf{q}_{h,n+1} - c_0\mathbf{v}_{h,n+1}\cdot\nabla\theta_{h,n+1}\right)\Big|_{\Omega_e} \tag{100}$$

Furthermore, for linear elements the heat flux is constant within the elements and, therefore, its divergence is zero within an element, yielding the following approximation for the temperature subgrid scale,

$$\tilde{\theta}_{n+1}\big|_{\Omega_e} := -\tau^{(2)}_{e,n+1} P^{\perp}_h \left(c_0\mathbf{v}_{h,n+1}\cdot\nabla\theta_{h,n+1}\right)\Big|_{\Omega_e} \tag{101}$$

2.5.3 *Stabilized discrete mixed variational form of the quasi-static transient coupled thermo-mechanical problem in Eulerian form*

Substituting the OSGS approximation of the velocity subgrid scale given by (86) and the ASGS approximation of the temperature subgrid scale given by (97), the time discrete multiscale stabilized variational form given by (71)-(73) reads:

Find a velocity vector field $\mathbf{v}_{h,n+1} \in \mathcal{V}_h$, *pressure field* $p_{h,n+1} \in \mathcal{Q}_h$ *and temperature field* $\theta_{h,n+1} \in \mathcal{T}_h$, *such that the following equations hold in* Ω*:*

$$\left(p_{h,n+1}, \nabla\cdot\delta\mathbf{v}_h\right) + \left(\mathbf{s}_{h,n+1}, \nabla^s\delta\mathbf{v}_h\right) + \sum_{e=1}^{nelem}\left(\tilde{\mathbf{s}}_{n+1}, \nabla^s\delta\mathbf{v}_h\right)\Big|_{\Omega_e} = l_{m_{h,n+1}}\left(\delta\mathbf{v}_h\right) \quad \forall\delta\mathbf{v}_h \in \mathcal{V}_{0,h} \tag{102}$$

$$\begin{aligned}
&\left(\nabla\cdot\mathbf{v}_{h,n+1}, \delta p_h\right) - \left(\frac{1}{\Delta t}\left(e^{\theta}_{h,n+1} - e^{\theta}_{h,n}\right) + \mathbf{v}_{h,n+1}\cdot\nabla e^{\theta}_{h,n+1}, \delta p_h\right) - \\
&- \sum_{e=1}^{nelem}\left(\frac{1}{\Delta t}\left(\tilde{e}^{\theta}_{h,n+1} - \tilde{e}^{\theta}_{h,n}\right) + \mathbf{v}_{h,n+1}\cdot\nabla\tilde{e}^{\theta}_{h,n+1}, \delta p_h\right)\Big|_{\Omega_e} + \\
&+ \sum_{e=1}^{nelem}\left(\nabla\cdot\tilde{\mathbf{v}}_{n+1} - \tilde{\mathbf{v}}_{n+1}\cdot\nabla e^{\theta}_{h,n+1} - \tilde{\mathbf{v}}_{n+1}\cdot\nabla\tilde{e}^{\theta}_{h,n+1}, \delta p_h\right)\Big|_{\Omega_e} = 0 \quad \forall\delta p_h \in \mathcal{Q}_h
\end{aligned} \tag{103}$$

$$\begin{aligned}
&\left(\frac{c_0}{\Delta t}\left(\theta_{h,n+1} - \theta_{h,n}\right) + c_0\mathbf{v}_{h,n+1}\cdot\nabla\theta_{h,n+1}, \delta\theta_h\right) - \left(\mathbf{q}_{h,n+1}, \nabla\delta\theta_h\right) - \left(\mathcal{D}_{h,n+1}, \delta\theta_h\right) + \\
&+ \sum_{e=1}^{nelem}\left(\frac{c_0}{\Delta t}\left(\tilde{\theta}_{n+1} - \tilde{\theta}_n\right) + c_0\mathbf{v}_{h,n+1}\cdot\nabla\tilde{\theta}_{n+1}, \delta\theta_h\right)\Big|_{\Omega_e} + \\
&+ \sum_{e=1}^{nelem}\left(c_0\tilde{\mathbf{v}}_{n+1}\cdot\nabla\theta_{h,n+1} + c_0\tilde{\mathbf{v}}_{n+1}\cdot\nabla\tilde{\theta}_{n+1}, \delta\theta_h\right)\Big|_{\Omega_e} - \\
&- \sum_{e=1}^{nelem}\left(\tilde{\mathbf{q}}_{n+1}, \nabla\delta\theta_h\right)\Big|_{\Omega_e} = l_{t_{h,n+1}}\left(\delta\theta_h\right) \quad \forall\delta\theta_h \in \mathcal{T}_{0,h}
\end{aligned} \tag{104}$$

Neglecting the influence of the temperature subgrid scale terms on (103) and on the transient term in (104) and neglecting second-order subgrid scale effects on (104), the time discrete multiscale stabilized variational form given by (102)-(104) reads:

Find a velocity vector field $\mathbf{v}_{h,n+1} \in \mathcal{V}_h$, *pressure field* $p_{h,n+1} \in \mathcal{Q}_h$ *and temperature field* $\theta_{h,n+1} \in \mathcal{T}_h$, *such that the following equations hold in* Ω:

$$\left(p_{h,n+1}, \nabla \cdot \delta\mathbf{v}_h\right) + \left(\mathbf{s}_{h,n+1}, \nabla^s \delta\mathbf{v}_h\right) + \sum_{e=1}^{nelem} \left(\tilde{\mathbf{s}}_{n+1}, \nabla^s \delta\mathbf{v}_h\right)\Big|_{\Omega_e} = l_{m_{h,n+1}}\left(\delta\mathbf{v}_h\right) \quad \forall \delta\mathbf{v}_h \in \mathcal{V}_{0,h} \tag{105}$$

$$\left(\nabla \cdot \mathbf{v}_{h,n+1}, \delta p_h\right) - \left(\frac{1}{\Delta t}\left(e^{\theta}_{h,n+1} - e^{\theta}_{h,n}\right) + \mathbf{v}_{h,n+1} \cdot \nabla e^{\theta}_{h,n+1}, \delta p_h\right) + \sum_{e=1}^{nelem} \left(\nabla \cdot \tilde{\mathbf{v}}_{n+1}, \delta p_h\right)\Big|_{\Omega_e} - \\ - \sum_{e=1}^{nelem} \left(\tilde{\mathbf{v}}_{n+1} \cdot \nabla e^{\theta}_{h,n+1}, \delta p_h\right)\Big|_{\Omega_e} = 0 \quad \forall \delta p_h \in \mathcal{Q}_h \tag{106}$$

$$\left(\frac{c_0}{\Delta t}\left(\theta_{h,n+1} - \theta_{h,n}\right) + c_0 \mathbf{v}_{h,n+1} \cdot \nabla \theta_{h,n+1}, \delta\theta_h\right) - \left(\mathbf{q}_{h,n+1}, \nabla \delta\theta_h\right) - \left(\mathcal{D}_{h,n+1}, \delta\theta_h\right) + \\ + \sum_{e=1}^{nelem} \left(c_0 \mathbf{v}_{h,n+1} \cdot \nabla \tilde{\theta}_{n+1}, \delta\theta_h\right)\Big|_{\Omega_e} + \sum_{e=1}^{nelem} \left(c_0 \tilde{\mathbf{v}}_{n+1} \cdot \nabla \theta_{h,n+1}, \delta\theta_h\right)\Big|_{\Omega_e} - \\ - \sum_{e=1}^{nelem} \left(\tilde{\mathbf{q}}_{n+1}, \nabla \delta\theta_h\right)\Big|_{\Omega_e} = l_{t_{h,n+1}}\left(\delta\theta_h\right) \quad \forall \delta\theta_h \in \mathcal{T}_{0,h} \tag{107}$$

Using the mechanical constitutive equation for the subgrid scale given by (59), substituting in the third term on the left-hand-side of (105), integrating by parts and assuming that the velocity subgrid scale vanish at the element boundaries, yields,

$$\sum_{e=1}^{nelem} \left(\tilde{\mathbf{s}}_{n+1}, \nabla^s \delta\mathbf{v}_h\right)\Big|_{\Omega_e} = \sum_{e=1}^{nelem} \left(2\tilde{\mu}_{n+1} dev\left(\nabla^s \tilde{\mathbf{v}}_{n+1}\right), \nabla^s \delta\mathbf{v}_h\right)\Big|_{\Omega_e} = \\ = \sum_{e=1}^{nelem} \left(2\tilde{\mu}_{n+1} dev\left(\nabla^s \delta\mathbf{v}_h\right), \nabla^s \tilde{\mathbf{v}}_{n+1}\right)\Big|_{\Omega_e} = \\ = -\sum_{e=1}^{nelem} \left(\nabla \cdot \left(2\tilde{\mu}_{n+1} dev\left(\nabla^s \delta\mathbf{v}_h\right)\right), \tilde{\mathbf{v}}_{n+1}\right)\Big|_{\Omega_e} + \sum_{e=1}^{nelem} \left(2\tilde{\mu}_{n+1} dev\left(\nabla^s \delta\mathbf{v}_h\right) \cdot \mathbf{n}, \tilde{\mathbf{v}}_{n+1}\right)\Big|_{\partial\Omega_e} = \\ = -\sum_{e=1}^{nelem} \left(\nabla \cdot \left(2\tilde{\mu}_{n+1} dev\left(\nabla^s \delta\mathbf{v}_h\right)\right), \tilde{\mathbf{v}}_{n+1}\right)\Big|_{\Omega_e} \tag{108}$$

where $\mathbf{n}$ is the unit outward normal to the element boundaries.

For linear elements $2\tilde{\mu}_{n+1} dev\left(\nabla^s \delta\mathbf{v}_h\right)$ is constant within the elements and therefore its divergence is zero within an element, getting,

$$\sum_{e=1}^{nelem} \left(\tilde{\mathbf{s}}_{n+1}, \nabla^s \delta\mathbf{v}_h\right)\Big|_{\Omega_e} = -\sum_{e=1}^{nelem} \left(\nabla \cdot \left(2\tilde{\mu}_{n+1} dev\left(\nabla^s \delta\mathbf{v}_h\right)\right), \tilde{\mathbf{v}}_{n+1}\right)\Big|_{\Omega_e} = 0 \tag{109}$$

Using the thermal constitutive equation for the temperature subgrid scale given by (65), substituting in the last term of the left-hand-side of (107), integrating by parts and assuming that the temperature subgrid scale vanish at the element boundaries, yields,

$$\sum_{e=1}^{nelem} \left(\tilde{\mathbf{q}}_{n+1}, \nabla \delta\theta_h\right)\Big|_{\Omega_e} = -\sum_{e=1}^{nelem} \left(\tilde{k}_{n+1} \nabla \tilde{\theta}_{n+1}, \nabla \delta\theta_h\right)\Big|_{\Omega_e} = -\sum_{e=1}^{nelem} \left(\tilde{k}_{n+1} \nabla \delta\theta_h, \nabla \tilde{\theta}_{n+1}\right)\Big|_{\Omega_e} = \\ = \sum_{e=1}^{nelem} \left(\nabla \cdot \left(\tilde{k}_{n+1} \nabla \delta\theta_h\right), \tilde{\theta}_{n+1}\right)\Big|_{\Omega_e} - \sum_{e=1}^{nelem} \left(\tilde{k}_{n+1} \nabla \delta\theta_h \cdot \mathbf{n}, \tilde{\theta}_{n+1}\right)\Big|_{\partial\Omega_e} = \\ = \sum_{e=1}^{nelem} \left(\nabla \cdot \left(\tilde{k}_{n+1} \nabla \delta\theta_h\right), \tilde{\theta}_{n+1}\right)\Big|_{\Omega_e} \tag{110}$$

where $\mathbf{n}$ is the unit outward normal to the element boundaries.

For linear elements $\tilde{k}_{n+1} \nabla \delta\theta_h$ is constant within the elements and therefore its divergence is zero within an element, getting,

$$\sum_{e=1}^{nelem}\left(\tilde{\mathbf{q}}_{n+1},\nabla\delta\theta_h\right)\Big|_{\Omega_e}=\sum_{e=1}^{nelem}\left(\nabla\cdot\left(\tilde{k}_{n+1}\nabla\delta\theta_h\right),\tilde{\theta}_{n+1}\right)\Big|_{\Omega_e}=0 \tag{111}$$

Integrating by parts, at the element level, the third term on the left-hand-side of (106) and assuming that the velocity subgrid scale vanish at the element boundaries, yields,

$$\begin{aligned}\sum_{e=1}^{nelem}\left(\nabla\cdot\tilde{\mathbf{v}}_{n+1},\delta p_h\right)\Big|_{\Omega_e}&=-\sum_{e=1}^{nelem}\left(\tilde{\mathbf{v}}_{n+1},\nabla\delta p_h\right)\Big|_{\Omega_e}+\sum_{e=1}^{nelem}\left(\tilde{\mathbf{v}}_{n+1}\cdot\mathbf{n},\delta p_h\right)\Big|_{\Omega_e}=\\&=-\sum_{e=1}^{nelem}\left(\tilde{\mathbf{v}}_{n+1},\nabla\delta p_h\right)\Big|_{\Omega_e}\end{aligned} \tag{112}$$

where $\mathbf{n}$ is the unit outward normal to the element boundaries.

Integrating by parts, at the element level, the fourth term on the left-hand-side of (107) and assuming that the temperature subgrid scale vanish at the element boundaries, yields,

$$\begin{aligned}\sum_{e=1}^{nelem}\left(c_0\mathbf{v}_{h,n+1}\cdot\nabla\tilde{\theta}_{n+1},\delta\theta_h\right)\Big|_{\Omega_e}&=-\sum_{e=1}^{nelem}\left(\tilde{\theta}_{n+1},c_0\mathbf{v}_{h,n+1}\cdot\nabla\delta\theta_h\right)\Big|_{\Omega_e}-\\&-\sum_{e=1}^{nelem}\left(\tilde{\theta}_{n+1},c_0\nabla\cdot\mathbf{v}_{h,n+1}\delta\theta_h\right)\Big|_{\Omega_e}+\sum_{e=1}^{nelem}\left(\tilde{\theta}_{n+1},c_0\mathbf{v}_{h,n+1}\cdot\mathbf{n}\delta\theta_h\right)\Big|_{\partial\Omega_e}=\\&-\sum_{e=1}^{nelem}\left(\tilde{\theta}_{n+1},c_0\mathbf{v}_{h,n+1}\cdot\nabla\delta\theta_h\right)\Big|_{\Omega_e}-\sum_{e=1}^{nelem}\left(\tilde{\theta}_{n+1},c_0\nabla\cdot\mathbf{v}_{h,n+1}\delta\theta_h\right)\Big|_{\Omega_e}\end{aligned} \tag{113}$$

where $\mathbf{n}$ is the unit outward normal to the element boundaries.

Then substituting into (109)-(113), the time discrete multiscale stabilized variational form given by (102)-(104) reads:

Find a velocity vector field $\mathbf{v}_{h,n+1}\in\mathcal{V}_h$, *pressure field* $p_{h,n+1}\in\mathcal{Q}_h$ *and temperature field* $\theta_{h,n+1}\in\mathcal{T}_h$, *such that the following equations hold in* Ω:

$$\left(p_{h,n+1},\nabla\cdot\delta\mathbf{v}_h\right)+\left(\mathbf{s}_{h,n+1},\nabla^s\delta\mathbf{v}_h\right)=l_{m_{h,n+1}}\left(\delta\mathbf{v}_h\right)\quad\forall\delta\mathbf{v}_h\in\mathcal{V}_{0,h} \tag{114}$$

$$\begin{aligned}&\left(\nabla\cdot\mathbf{v}_{h,n+1},\delta p_h\right)-\left(\frac{1}{\Delta t}\left(e^{\theta}_{h,n+1}-e^{\theta}_{h,n}\right)+\mathbf{v}_{h,n+1}\cdot\nabla e^{\theta}_{h,n+1},\delta p_h\right)-\\&-\sum_{e=1}^{nelem}\left(\tilde{\mathbf{v}}_{n+1},\nabla\delta p_h\right)\Big|_{\Omega_e}-\sum_{e=1}^{nelem}\left(\tilde{\mathbf{v}}_{n+1}\cdot\nabla e^{\theta}_{h,n+1},\delta p_h\right)\Big|_{\Omega_e}=0\quad\forall\delta p_h\in\mathcal{Q}_h\end{aligned} \tag{115}$$

$$\begin{aligned}&\left(\frac{c_0}{\Delta t}\left(\theta_{h,n+1}-\theta_{h,n}\right)+c_0\mathbf{v}_{h,n+1}\cdot\nabla\theta_{h,n+1},\delta\theta_h\right)-\left(\mathbf{q}_{h,n+1},\nabla\delta\theta_h\right)-\left(\mathcal{D}_{h,n+1},\delta\theta_h\right)+\\&-\sum_{e=1}^{nelem}\left(\tilde{\theta}_{n+1},c_0\mathbf{v}_{h,n+1}\cdot\nabla\delta\theta_h\right)\Big|_{\Omega_e}-\sum_{e=1}^{nelem}\left(\tilde{\theta}_{n+1},c_0\nabla\cdot\mathbf{v}_{h,n+1}\delta\theta_h\right)\Big|_{\Omega_e}+\\&+\sum_{e=1}^{nelem}\left(c_0\tilde{\mathbf{v}}_{n+1}\cdot\nabla\theta_{h,n+1},\delta\theta_h\right)\Big|_{\Omega_e}=l_{t_{h,n+1}}\left(\delta\theta_h\right)\quad\forall\delta\theta_h\in\mathcal{T}_{0,h}\end{aligned} \tag{116}$$

Using the OSGS approximation for the velocity subgrid scale given by (86) and the ASGS approximation for the temperature subgrid scale given by (97), the time-discrete multiscale stabilized variational form given by (114)-(116) reads:

Find the velocity vector field $\mathbf{v}_{h,n+1}\in\mathcal{V}_h$, *the pressure field* $p_{h,n+1}\in\mathcal{Q}_h$ *and the temperature field* $\theta_{h,n+1}\in\mathcal{T}_h$, *such that the following equations hold in* Ω:

$$\left(p_{h,n+1},\nabla\cdot\delta\mathbf{v}_h\right)+\left(\mathbf{s}_{h,n+1},\nabla^s\delta\mathbf{v}_h\right)=l_{m_{h,n+1}}\left(\delta\mathbf{v}_h\right)\quad\forall\delta\mathbf{v}_h\in\mathcal{V}_{0,h} \tag{117}$$

$$\begin{aligned}&\left(\nabla\cdot\mathbf{v}_{h,n+1},\delta p_h\right)-\left(\frac{1}{\Delta t}\left(e^{\theta}_{h,n+1}-e^{\theta}_{h,n}\right)+\mathbf{v}_{h,n+1}\cdot\nabla e^{\theta}_{h,n+1},\delta p_h\right)-\\&-\sum_{e=1}^{nelem}\tau^{(1)}_{e,n+1}\left(P_h^{\perp}\left(\nabla p_{h,n+1}\right),\nabla\delta p_h\right)\Big|_e-\\&-\sum_{e=1}^{nelem}\tau^{(1)}_{e,n+1}\left(P_h^{\perp}\left(\nabla p_{h,n+1}\right)\cdot\nabla e^{\theta}\left(\theta_{h,n+1}\right),\delta p_h\right)\Big|_e=0\quad\forall\delta p_h\in\mathcal{Q}_h\end{aligned} \tag{118}$$

$$\left(\frac{c_0}{\Delta t}\left(\theta_{h,n+1}-\theta_{h,n}\right)+c_0\mathbf{v}_{h,n+1}\cdot\nabla\theta_{h,n+1},\delta\theta_h\right)-\left(\mathbf{q}_{h,n+1},\nabla\delta\theta_h\right)-\left(\mathcal{D}_{h,n+1},\delta\theta_h\right)+$$
$$+\sum_{e=1}^{nelem}\tau_{e,n+1}^{(2)}\left(c_0\mathbf{v}_{h,n+1}\cdot\nabla\theta_{h,n+1},c_0\nabla\cdot\mathbf{v}_{h,n+1}\delta\theta_h\right)\Big|_e+$$
$$+\sum_{e=1}^{nelem}\tau_{e,n+1}^{(2)}\left(c_0\mathbf{v}_{h,n+1}\cdot\nabla\theta_{h,n+1},c_0\mathbf{v}_{h,n+1}\cdot\nabla\delta\theta_h\right)\Big|_e+$$
$$+\sum_{e=1}^{nelem}\tau_{e,n+1}^{(1)}\left(c_0P_h^{\perp}\left(\nabla p_{h,n+1}\right)\cdot\nabla\theta_{h,n+1},\delta\theta_h\right)\Big|_e=l_{t_{h,n+1}}\left(\delta\theta_h\right)\quad\forall\delta\theta_h\in\mathcal{T}_{0,h} \tag{119}$$

REMARK 4. *Note that with the above assumptions in hand, the following remarks can be made on the stabilized governing equations: (i) no stabilization terms arise in the variational form of the momentum balance equation; (ii) an OSGS velocity subgrid scale stabilization term arises in the variational equation of the pressure constitutive equation, while the temperature subgrid scale is not involved; (ii) both velocity and temperature subgrid scale stabilization terms arise in the variational form of the energy balance equation.*

Using a compact short notation, the time discrete stabilized variational problem defined by (117)-(119) can be stated as:

Find a vector field $\mathbf{V}_{h,n+1}\in\mathcal{W}_h$ *, such that the following equations hold in* Ω*:*

$$B_{stab}\left(\mathbf{V}_{h,n+1},\delta\mathbf{V}_h\right)=L\left(\delta\mathbf{V}_h\right)\quad\forall\delta\mathbf{V}_h\in\mathcal{W}_{0,h} \tag{120}$$

where the time discrete stabilized variational form $B_{stab}\left(\mathbf{V}_{h,n+1},\delta\mathbf{V}_h\right)$ is given by,

$$B_{stab}\left(\mathbf{V}_{h,n+1},\delta\mathbf{V}_h\right)=B\left(\mathbf{V}_{h,n+1},\delta\mathbf{V}_h\right)-$$
$$-\sum_{e=1}^{nelem}\tau_{e,n+1}^{(1)}\left(P_h^{\perp}\left(\nabla p_{h,n+1}\right),\nabla\delta p_h\right)\Big|_e-$$
$$-\sum_{e=1}^{nelem}\tau_{e,n+1}^{(1)}\left(P_h^{\perp}\left(\nabla p_{h,n+1}\right)\cdot\nabla e^{\theta}\left(\theta_{h,n+1}\right),\delta p_h\right)\Big|_e+$$
$$+\sum_{e=1}^{nelem}\tau_{e,n+1}^{(2)}\left(c_0\mathbf{v}_{h,n+1}\cdot\nabla\theta_{h,n+1},c_0\nabla\cdot\mathbf{v}_{h,n+1}\delta\theta_h\right)\Big|_e+$$
$$+\sum_{e=1}^{nelem}\tau_{e,n+1}^{(2)}\left(c_0\mathbf{v}_{h,n+1}\cdot\nabla\theta_{h,n+1},c_0\mathbf{v}_{h,n+1}\cdot\nabla\delta\theta_h\right)\Big|_e+$$
$$+\sum_{e=1}^{nelem}\tau_{e,n+1}^{(1)}\left(c_0P_h^{\perp}\left(\nabla p_{h,n+1}\right)\cdot\nabla\theta_{h,n+1},\delta\theta_h\right)\Big|_e \tag{121}$$

and $B\left(\mathbf{V}_{h,n+1},\delta\mathbf{V}_h\right)$ and $L\left(\delta\mathbf{V}_h\right)$ are given by,

$$B\left(\mathbf{V}_{h,n+1},\delta\mathbf{V}_h\right)=\left(p_{h,n+1},\nabla\cdot\delta\mathbf{v}_h\right)+\left(\mathbf{s}_{h,n+1},\nabla^s\delta\mathbf{v}_h\right)+\left(\nabla\cdot\mathbf{v}_{h,n+1},\delta p_h\right)-$$
$$-\left(\frac{1}{\Delta t}\left(e^{\theta}\left(\theta_{h,n+1}\right)-e^{\theta}\left(\theta_{h,n}\right)\right)+\mathbf{v}_{h,n+1}\cdot\nabla e^{\theta}\left(\theta_{h,n+1}\right),\delta p_h\right)+$$
$$+\left(\frac{c_0}{\Delta t}\left(\theta_{h,n+1}-\theta_{h,n}\right)+c_0\mathbf{v}_{h,n+1}\cdot\nabla\theta_{h,n+1},\delta\theta_h\right)-\left(\mathbf{q}\left(\theta_{h,n+1}\right),\nabla\delta\theta_h\right)-\left(\mathcal{D}_{h,n+1},\delta\theta_h\right) \tag{122}$$

$$L\left(\delta\mathbf{V}_h\right)=l_{m_{h,n+1}}\left(\delta\mathbf{v}_h\right)+l_{t_{h,n+1}}\left(\delta\theta_h\right) \tag{123}$$

Let us introduce now a new vector field $\Pi_{h,n+1}:=P_h\left(\nabla p_{h,n+1}\right)$ defined as the projection of the pressure gradient onto the finite element space [1, 2]. Let us also introduce $\Upsilon=\mathbf{H}^1$ and $\Upsilon_h\subset\Upsilon$ as the space of pressure gradient projection and its finite element associated space, respectively. Taking $\Pi_{h,n+1}\in\Upsilon_h$ as an independent continuous variable, the orthogonal projection of the discrete pressure gradient can be written as [1, 2, 8, 9, 13-15],

$$P_h^{\perp}\left(\nabla p_{h,n+1}\right)=\nabla p_{h,n+1}-\Pi_{h,n+1} \tag{124}$$

Using (124) the time-discrete multiscale stabilized variational form given by (117)-(119) reads:

Find the velocity vector field $\mathbf{v}_{h,n+1}\in\mathcal{V}_h$, *the pressure field* $p_{h,n+1}\in\mathcal{Q}_h$, *the continuous pressure gradient projection* $\Pi_{h,n+1}\in\Upsilon_h$ *and the temperature field* $\theta_{h,n+1}\in\mathcal{T}_h$, *such that the following equations hold in* Ω*:*

$$\left(p_{h,n+1},\nabla\cdot\delta\mathbf{v}_h\right)+\left(\mathbf{s}_{h,n+1},\nabla^s\delta\mathbf{v}_h\right)=l_{m_{h,n+1}}\left(\delta\mathbf{v}_h\right)\quad\forall\delta\mathbf{v}_h\in\mathcal{V}_{0,h} \tag{125}$$

$$\begin{aligned}&\left(\nabla\cdot\mathbf{v}_{h,n+1},\delta p_h\right)-\left(\frac{1}{\Delta t}\left(e^{\theta}\left(\theta_{h,n+1}\right)-e^{\theta}\left(\theta_{h,n}\right)\right)+\mathbf{v}_{h,n+1}\cdot\nabla e^{\theta}\left(\theta_{h,n+1}\right),\delta p_h\right)-\\&-\sum_{e=1}^{nelem}\tau_{e,n+1}^{(1)}\left(\nabla p_{h,n+1}-\Pi_{h,n+1},\nabla\delta p_h\right)\Big|_e-\\&-\sum_{e=1}^{nelem}\tau_{e,n+1}^{(1)}\left(\left(\nabla p_{h,n+1}-\Pi_{h,n+1}\right)\cdot\nabla e^{\theta}\left(\theta_{h,n+1}\right),\delta p_h\right)\Big|_e=0\quad\forall\delta p_h\in\mathcal{Q}_h\end{aligned} \tag{126}$$

$$\sum_{e=1}^{nelem}\tau_{e,n+1}^{(1)}\left(\nabla p_{h,n+1}-\Pi_{h,n+1},\delta\Pi_h\right)\Big|_e=0\quad\forall\delta\Pi_h\in\mathcal{V}_{0,h} \tag{127}$$

$$\begin{aligned}&\left(\frac{c_0}{\Delta t}\left(\theta_{h,n+1}-\theta_{h,n}\right)+c_0\mathbf{v}_{h,n+1}\cdot\nabla\theta_{h,n+1},\delta\theta_h\right)-\left(\mathbf{q}_{h,n+1},\nabla\delta\theta_h\right)-\left(\mathcal{D}_{h,n+1},\delta\theta_h\right)+\\&+\sum_{e=1}^{nelem}\tau_{e,n+1}^{(2)}\left(c_0\mathbf{v}_{h,n+1}\cdot\nabla\theta_{h,n+1},c_0\nabla\cdot\mathbf{v}_{h,n+1}\delta\theta_h\right)\Big|_e+\\&+\sum_{e=1}^{nelem}\tau_{e,n+1}^{(2)}\left(c_0\mathbf{v}_{h,n+1}\cdot\nabla\theta_{h,n+1},c_0\mathbf{v}_{h,n+1}\cdot\nabla\delta\theta_h\right)\Big|_e+\\&+\sum_{e=1}^{nelem}\tau_{e,n+1}^{(1)}\left(c_0\left(\nabla p_{h,n+1}-\Pi_{h,n+1}\right)\cdot\nabla\theta_{h,n+1},\delta\theta_h\right)\Big|_e=l_{t_{h,n+1}}\left(\delta\theta_h\right)\quad\forall\delta\theta_h\in\mathcal{T}_{0,h}\end{aligned} \tag{128}$$

REMARK 5. *The GLS pressure stabilized formulation can be obtained as a particular case of the OSGS pressure stabilized formulation, formally setting to zero the projection of the pressure gradient and avoiding, in this case, the additional equation introduced within the OSGS framework.*

REMARK 6. *The SUPG stabilized formulation can be obtained as a particular case of the ASGS temperature stabilized formulation, formally neglecting the contributions of the first and third stabilization terms considered in (128).*

2.6 Operator Split and Product Formula Algorithm (PFA) of the Multiscale Stabilized Discrete Mixed Variational Form of the Quasi-static Transient Coupled Thermo-mechanical Problem in Eulerian Form

The time discrete stabilized variational coupled thermo-mechanical problem defined by (125)-(128) can be solved using a staggered algorithm arising from an operator split and a product formula algorithm (PFA). Within this context, a mechanical problem given by (125)-(127) and a thermal problem given by (128) are defined. The mechanical problem, with the discrete velocity, pressure and continuous pressure gradient projection as mechanical variables, is defined holding constant the discrete temperature field, while the thermal problem, with the discrete temperature as thermal variable, is defined holding constant the mechanical variables.

A staggered algorithm is defined such that for any time step, the mechanical problem is solved first at constant temperature and then the thermal problem is solved keeping constant the mechanical variables, velocity, pressure and pressure gradient projection.

Mechanical Problem. The time-discrete multiscale stabilized variational form of the mechanical problem reads:

Find the velocity vector field $\mathbf{v}_{h,n+1} \in \mathcal{V}_h$, *the pressure field* $p_{h,n+1} \in \mathcal{Q}_h$ *and the continuous pressure gradient projection* $\Pi_{h,n+1} \in \Upsilon_h$, *such that for a fixed temperature field* $\theta_{h,n} \in \mathcal{T}_h$, *the following equations hold in* Ω:

$$\left(p_{h,n+1}, \nabla \cdot \delta \mathbf{v}_h\right) + \left(\mathbf{s}_{h,n+1}, \nabla^s \delta \mathbf{v}_h\right) = l_{m_{h,n+1}}\left(\delta \mathbf{v}_h\right) \quad \forall \delta \mathbf{v}_h \in \mathcal{V}_{0,h} \tag{129}$$

$$\begin{aligned} &\left(\nabla \cdot \mathbf{v}_{h,n+1}, \delta p_h\right) - \left(\mathbf{v}_{h,n+1} \cdot \nabla e^{\theta}\left(\theta_{h,n}\right), \delta p_h\right) - \\ &- \sum_{e=1}^{nelem} \tau_{e,n+1}^{(1)} \left(\nabla p_{h,n+1} - \Pi_{h,n+1}, \nabla \delta p_h\right)\Big|_e \\ &- \sum_{e=1}^{nelem} \tau_{e,n+1}^{(1)} \left(\left(\nabla p_{h,n+1} - \Pi_{h,n+1}\right) \cdot \nabla e^{\theta}\left(\theta_{h,n}\right), \delta p_h\right)\Big|_e = 0 \quad \forall \delta p_h \in \mathcal{Q}_h \end{aligned} \tag{130}$$

$$\sum_{e=1}^{nelem} \tau_{e,n+1}^{(1)} \left(\nabla p_{h,n+1} - \Pi_{h,n+1}, \delta \Pi_h\right)\Big|_e = 0 \quad \forall \delta \Pi_h \in \mathcal{V}_{0,h} \tag{131}$$

where now $\mathbf{s}_{h,n+1} := \mathbf{s}\left(\mathbf{v}_{h,n+1}, \theta_{h,n}\right)$ is computed at the fixed temperature $\theta_{h,n}$ at time n. Note that, because the mechanical problem is solved at a constant temperature, the term arising from the local time variation of the thermal deformation is zero.

Thermal Problem. The time-discrete multiscale stabilized variational form of the thermal problem reads:

Find the temperature field $\theta_{h,n+1} \in \mathcal{T}_h$, *such that for fixed velocity vector field* $\mathbf{v}_{h,n+1} \in \mathcal{V}_h$, *pressure field* $p_{h,n+1} \in \mathcal{Q}_h$ *and continuous pressure gradient projection* $\Pi_{h,n+1} \in \Upsilon_h$, *the following equation holds in* Ω:

$$\begin{aligned} &\left(\frac{c_0}{\Delta t}\left(\theta_{h,n+1} - \theta_{h,n}\right), \delta\theta_h\right) + \left(c_0 \mathbf{v}_{h,n+1} \cdot \nabla \theta_{h,n+1}, \delta\theta_h\right) - \left(\mathbf{q}_{h,n+1}, \nabla \delta\theta_h\right) - \left(\mathcal{D}_{h,n+1}, \delta\theta_h\right) + \\ &+ \sum_{e=1}^{nelem} \tau_{e,n+1}^{(2)} \left(c_0 \mathbf{v}_{h,n+1} \cdot \nabla \theta_{h,n+1}, c_0 \nabla \cdot \mathbf{v}_{h,n+1} \delta\theta_h\right)\Big|_e + \\ &+ \sum_{e=1}^{nelem} \tau_{e,n+1}^{(2)} \left(c_0 \mathbf{v}_{h,n+1} \cdot \nabla \theta_{h,n+1}, c_0 \mathbf{v}_{h,n+1} \cdot \nabla \delta\theta_h\right)\Big|_e + \\ &+ \sum_{e=1}^{nelem} \tau_{e,n+1}^{(1)} \left(c_0 P_h^{\perp}\left(\nabla p_{h,n+1}\right) \cdot \nabla \theta_{h,n+1}, \delta\theta_h\right)\Big|_e = l_{t_{h,n+1}}\left(\delta\theta_h\right) \quad \forall \delta\theta_h \in \mathcal{T}_{0,h} \end{aligned} \tag{132}$$

2.7 *Matrix Form of the Product Formula Algorithm of the Multiscale Stabilized Discrete Mixed Variational Form of the Quasi-static Transient Coupled Thermo-mechanical Problem in Eulerian Form*

Mechanical problem. Once the finite element discretization has been performed, the matrix form of the algebraic system resulting from the variational systems (129)-(131) defining the mechanical problem reads,

$$\mathbb{F}_{dev}\left(\mathbb{V}_{n+1}\right) + \mathbb{G}\mathbb{P}_{n+1} = \mathbb{F}_{n+1} \tag{133}$$

$$\left(\mathbb{G}^T + \mathbb{C}_n\right)\mathbb{V}_{n+1} - \left(\mathbb{L}_{\tau_{e,n+1}^{(1)}} + \mathbb{C}_{\tau_{e,n+1}^{(1)}}\right)\mathbb{P}_{n+1} + \left(\mathbb{G}^T_{\tau_{e,n+1}^{(1)}} + \hat{\mathbb{C}}_{\tau_{e,n+1}^{(1)}}\right)\mathbb{Q}_{n+1} = 0 \tag{134}$$

$$\mathbb{G}_{\tau_{e,n+1}^{(1)}}\mathbb{P}_{n+1} - \mathbb{M}_{\tau_{e,n+1}^{(1)}}\mathbb{Q}_{n+1} = 0 \tag{135}$$

where $\mathbb{V}_{n+1}$, $\mathbb{P}_{n+1}$ and $\mathbb{Q}_{n+1}$ denote the global nodal velocity, pressure and pressure gradient projection vectors at time n+1, $\mathbb{F}_{dev}\left(\mathbb{V}_{n+1}\right)$ denotes the global nodal internal forces arising from the deviatoric part of the stresses, $\mathbb{F}_{n+1}$ denotes the global nodal forces vector, $\mathbb{G}$

denotes the global nodal matrix arising from the gradient operator, $\mathbb{G}^T$ denotes the global nodal matrix arising from the divergence operator, $\mathbb{C}_n$ denotes the global nodal matrix arising from the convective transport of the gradient of the thermal strain with a fixed temperature evaluated at time n, $\mathbb{L}_{\tau_{e,n+1}^{(1)}}$ denotes the global nodal stabilized Laplace operator, $\mathbb{G}^T_{\tau_{e,n+1}^{(1)}}$ denotes the global nodal stabilized divergence operator, $\mathbb{G}_{\tau_{e,n+1}^{(1)}}$ denotes the global nodal stabilized gradient operator, $\mathbb{C}_{\tau_{e,n+1}^{(1)}}$ and $\widehat{\mathbb{C}}_{\tau_{e,n+1}^{(1)}}$ denote global nodal stabilized matrices arising from the convective transport of the gradient of the thermal strain at fixed temperature at time n and $\mathbb{M}_{\tau_{e,n+1}^{(1)}}$ denotes the global nodal stabilized mass-like operator.

Thermal Problem. The algebraic system resulting from the variational form (132) defining the thermal problem reads,

$$\mathbb{E}\left(\mathbb{T}_{n+1},\mathbb{T}_n\right)+\mathbb{E}_{\tau_{e,n+1}^{(2)}}\left(\mathbb{T}_{n+1}\right)+\mathbb{E}_{\tau_{e,n+1}^{(1)}}\left(\mathbb{T}_{n+1}\right)=\mathbb{H}_{n+1} \tag{136}$$

where $\mathbb{T}_{n+1}$ and $\mathbb{T}_{n+1}$ denote the global nodal temperatures vector at time n+1 and time n, respectively, $\mathbb{E}\left(\mathbb{T}_{n+1},\mathbb{T}_n\right)$ denote the global nodal vector arising from the transient, convective and diffusive heat transfer at time n+1, $\mathbb{H}_{n+1}$ denotes the global nodal vector arising from the internal heat sources and prescribed heat flow at the boundaries and $\mathbb{E}_{\tau_{e,n+1}^{(2)}}\left(\mathbb{T}_{n+1}\right)$ and $\mathbb{E}_{\tau_{e,n+1}^{(1)}}\left(\mathbb{T}_{n+1}\right)$ denote the global nodal stabilized vectors arising from the temperature and velocity subgrid scales, respectively.

2.7.1 Solution of the mechanical problem

A computational efficient and robust solution algorithm for the mechanical problem can be built up solving first for $\mathbb{V}_{n+1}$ and $\mathbb{P}_{n+1}$ keeping fixed $\mathbb{Q}_n$ from the previous computed time step and evaluating the operators $\mathbb{L}_{\tau_{e,n}^{(1)}}$, $\mathbb{G}^T_{\tau_{e,n}^{(1)}}$, $\mathbb{C}_{\tau_{e,n}^{(1)}}$ and $\widehat{\mathbb{C}}_{\tau_{e,n}^{(1)}}$ at the time step n, instead of at the time step n+1, yielding the following modified mechanical subproblem,

$$\mathbb{F}_{dev}\left(\mathbb{V}_{n+1}\right)+\mathbb{G}\mathbb{P}_{n+1}=\mathbb{F}_{n+1} \tag{137}$$

$$\left(\mathbb{G}^T+\mathbb{C}_n\right)\mathbb{V}_{n+1}-\left(\mathbb{L}_{\tau_{e,n}^{(1)}}+\mathbb{C}_{\tau_{e,n}^{(1)}}\right)\mathbb{P}_{n+1}=-\left(\mathbb{G}^T_{\tau_{e,n}^{(1)}}+\widehat{\mathbb{C}}_{\tau_{e,n}^{(1)}}\right)\mathbb{Q}_n \tag{138}$$

To solve the nonlinear system (137)-(138) using an incremental iterative Newton-Raphson algorithm, we have to compute the exact linearization of (137)-(138) yielding the following incremental iterative linear system of equations,

$$\mathbb{K}_{T_{dev}}\left(\mathbb{V}_{n+1}^{(i)}\right)\Delta\mathbb{V}_{n+1}^{(i)}+\mathbb{G}\Delta\mathbb{P}_{n+1}^{(i)}=-\mathbb{R}_{v,n+1}^{(i)} \tag{139}$$

$$\left(\mathbb{G}^T+\mathbb{C}_n\right)\Delta\mathbb{V}_{n+1}^{(i)}-\left(\mathbb{L}_{\tau_{e,n}^{(1)}}+\mathbb{C}_{\tau_{e,n}^{(1)}}\right)\Delta\mathbb{P}_{n+1}^{(i)}=-\mathbb{R}_{p,n+1}^{(i)} \tag{140}$$

where the residual vectors $\mathbb{R}_{v,n+1}^{(i)}$ and $\mathbb{R}_{p,n+1}^{(i)}$ entering in (139) and (140), respectively, are given by,

$$\mathbb{R}_{v,n+1}^{(i)}=\mathbb{F}_{dev}\left(\mathbb{V}_{n+1}^{(i)}\right)+\mathbb{G}\mathbb{P}_{n+1}^{(i)}-\mathbb{F}_{n+1}^{(i)} \tag{141}$$

$$\mathbb{R}_{p,n+1}^{(i)}=\left(\mathbb{G}^T+\mathbb{C}_n\right)\mathbb{V}_{n+1}-\left(\mathbb{L}_{\tau_{e,n}^{(1)}}+\mathbb{C}_{\tau_{e,n}^{(1)}}\right)\mathbb{P}_{n+1}+\left(\mathbb{G}^T_{\tau_{e,n}^{(1)}}+\widehat{\mathbb{C}}_{\tau_{e,n}^{(1)}}\right)\mathbb{Q}_n \tag{142}$$

where $\mathbb{K}_{T_{dev}}\left(\mathbb{V}_{n+1}^{(i)}\right)$ denotes the deviatoric part of the mechanical consistent tangent operator and $\Delta\mathbb{V}_{n+1}^{(i)}$ and $\Delta\mathbb{P}_{n+1}^{(i)}$ denote the increment of velocity and pressure vectors, respectively, given by,

$$\Delta\mathbb{V}_{n+1}^{(i)} := \mathbb{V}_{n+1}^{(i+1)} - \mathbb{V}_{n+1}^{(i)} \tag{143}$$

$$\Delta\mathbb{P}_{n+1}^{(i)} := \mathbb{P}_{n+1}^{(i+1)} - \mathbb{P}_{n+1}^{(i)} \tag{144}$$

Once the algebraic nonlinear system of equations (141)-(142) has been solved, $\mathbb{Q}_{n+1}$ is obtained solving the system,

$$\mathbb{Q}_{n+1} = \mathbb{M}^{-1}_{\tau^{(1)}_{e,n+1}}\,\mathbb{G}_{\tau^{(1)}_{e,n+1}}\,\mathbb{P}_{n+1} \tag{145}$$

where a lumped structure for $\mathbb{M}^{-1}_{\tau^{(1)}_{e,n+1}}$ is used to reduce the computational cost [1, 2, 8, 9, 13-15].

Typical element entries for a node A of the residual vectors $\mathbb{R}^{(i)}_{v,n+1}$ and $\mathbb{R}^{(i)}_{p,n+1}$ take the form,

$$\mathbb{R}^{(i)}_{v,n+1}\Big|^{A}_{\Omega_e} = \int_{\Omega_e}\mathbf{B}^T_A\,\mathbf{s}^{(i)}_{h,n+1}d\Omega + \int_{\Omega_e}\nabla N_{v,A}\,p^{(i)}_{h,n+1}d\Omega - \int_{\Omega_e}N_{v,A}\,\mathbf{f}_{h,n+1}d\Omega - \int_{\partial\Omega_e}N_{v,A}\,\overline{\mathbf{t}}_{h,n+1}d\partial\Omega \tag{146}$$

$$\begin{aligned}\mathbb{R}^{(i)}_{p,n+1}\Big|^{A}_{\Omega_e} &= \int_{\Omega_e}N_{p,A}\,\nabla\cdot\mathbf{v}^{(i)}_{h,n+1}\,d\Omega - \int_{\Omega_e}N_{p,A}\,\mathbf{v}^{(i)}_{h,n+1}\cdot\nabla e^{\theta}\left(\theta_n\right)d\Omega - \\ &- \int_{\Omega_e}\tau^{(1)}_{e,n}\left(\nabla p^{(i)}_{h,n+1} - \Pi_{h,n}\right)\cdot\nabla e^{\theta}\left(\theta_n\right)N_{p,A}\,d\Omega - \int_{\Omega_e}\tau^{(1)}_{e,n}\left(\nabla p^{(i)}_{h,n+1} - \Pi_{h,n}\right)\cdot\nabla N_{p,A}\,d\Omega\end{aligned} \tag{147}$$

where $N_{v,A}$ and $N_{p,A}$ are the velocity and pressure shape function interpolations for node A, and $\mathbf{B}_A$ is the velocity symmetric gradient interpolation matrix for node A.

Typical element entries for nodes A and B of the matrices involved above take the form,

$$\mathbb{K}^{(i)}_{T_{dev}}\left(\mathbb{V}^{(i)}_{n+1}\right)\Big|^{AB}_{\Omega_e} = \int_{\Omega_e}\mathbf{B}^T_A : \mathbf{C}^{dev(i)}_{T_{n+1}} : \mathbf{B}_B\,d\Omega \tag{148}$$

$$\mathbb{G}\Big|^{AB}_{\Omega_e} = \int_{\Omega_e}\nabla N_{v,A}\,N_{p,B}\,d\Omega \tag{149}$$

$$\mathbb{L}_{\tau^{(1)}_{e,n}}\Big|^{AB}_{\Omega_e} = \int_{\Omega_e}\tau^{(1)}_{e,n}\,\nabla N_{p,A}\cdot\nabla N_{p,B}\,d\Omega \tag{150}$$

$$\mathbb{C}_{\tau^{(1)}_{e,n}}\Big|^{AB}_{\Omega_e} = \int_{\Omega_e}\tau^{(1)}_{e,n}\,N_{p,A}\,\nabla N_{p,B}\cdot\nabla e^{\theta}\,d\Omega \tag{151}$$

$$\mathbb{G}^T_{\tau^{(1)}_{e,n}}\Big|^{AB}_{\Omega_e} = \int_{\Omega_e}\tau^{(1)}_{e,n}\,\nabla N_{p,A}\,N_{\Pi,B}\,d\Omega \tag{152}$$

$$\widehat{\mathbb{C}}_{\tau^{(1)}_{e,n}}\Big|^{AB}_{\Omega_e} = \int_{\Omega_e}\tau^{(1)}_{e,n}\,N_{p,A}\,N_{\Pi,B}\nabla e^{\theta}\,d\Omega \tag{153}$$

$$\mathbb{M}_{\tau^{(1)}_{e,n}}\Big|^{AB}_{\Omega_e} = \int_{\Omega_e}\tau^{(1)}_{e,n}\,N_{\Pi,A}N_{\Pi,B}\,\mathbf{1}\,d\Omega \tag{154}$$

where $N_{\Pi,A}$ is the pressure gradient projection shape function interpolation for node A and $\mathbf{C}^{dev(i)}_{T_{n+1}}$ is the fourth-order deviatoric consistent tangent constitutive tensor arising from the linearization of the deviatoric part of the time discretized constitutive equation. Here the following constitutive models have been considered.

Norton-Hoff constitutive model. The discrete version of the constitutive equation for a rigid viscoplatic Norton-Hoff model at time n+1, at constant temperature at time n, is given by,

$$\mathbf{s}_{h,n+1}^{(i)} = K\left(\theta_{h,n}\right)\left(\sqrt{3}\dot{\bar{\varepsilon}}_{h,n+1}^{(i)}\right)^{m\left(\theta_{h,n}\right)-1} dev\left(\dot{\boldsymbol{\varepsilon}}_{h,n+1}^{(i)}\right) = 2\mu\left(\dot{\bar{\varepsilon}}_{h,n+1}^{(i)}, \theta_{h,n}\right) dev\left(\dot{\boldsymbol{\varepsilon}}_{h,n+1}^{(i)}\right) \tag{155}$$

where the discrete equivalent strain rate $\dot{\bar{\varepsilon}}_{h,n+1}^{(i)}$ is given by,

$$\dot{\bar{\varepsilon}}_{h,n+1}^{(i)} = \sqrt{2/3}\left\| dev\left(\dot{\boldsymbol{\varepsilon}}_{h,n+1}^{(i)}\right)\right\| \tag{156}$$

and the norm $\left\| dev\left(\dot{\boldsymbol{\varepsilon}}_{h,n+1}^{(i)}\right)\right\|$ is given by,

$$\left\| dev\left(\dot{\boldsymbol{\varepsilon}}_{h,n+1}^{(i)}\right)\right\| = \left(dev\left(\dot{\boldsymbol{\varepsilon}}_{h,n+1}^{(i)}\right) : dev\left(\dot{\boldsymbol{\varepsilon}}_{h,n+1}^{(i)}\right)\right)^{1/2} \tag{157}$$

The linearization of (155) reads,

$$\begin{aligned}\Delta\mathbf{s}_{h,n+1}^{(i)} = {} & K\left(\theta_{h,n}\right)\left(m\left(\theta_{h,n}\right)-1\right)\sqrt{3}\Delta\dot{\bar{\varepsilon}}_{h,n+1}^{(i)}\left(\sqrt{3}\dot{\bar{\varepsilon}}_{h,n+1}^{(i)}\right)^{m\left(\theta_{h,n}\right)-2} dev\left(\dot{\boldsymbol{\varepsilon}}_{h,n+1}^{(i)}\right) + \\ & + K\left(\theta_{h,n}\right)\left(\sqrt{3}\dot{\bar{\varepsilon}}_{h,n+1}^{(i)}\right)^{m\left(\theta_{h,n}\right)-2} \Delta dev\left(\dot{\boldsymbol{\varepsilon}}_{h,n+1}^{(i)}\right)\end{aligned} \tag{158}$$

where the variation $\Delta\dot{\bar{\varepsilon}}_{h,n+1}^{(i)}$ takes the form,

$$\Delta\dot{\bar{\varepsilon}}_{h,n+1}^{(i)} = \sqrt{2/3}\,\Delta\left\| dev\left(\dot{\boldsymbol{\varepsilon}}_{h,n+1}^{(i)}\right)\right\| = \sqrt{2/3}\,\mathbf{n}_{h,n+1}^{(i)} : \Delta dev\left(\dot{\boldsymbol{\varepsilon}}_{h,n+1}^{(i)}\right) \tag{159}$$

where $\mathbf{n}_{h,n+1}^{(i)}$ is the deviatoric second order unit tensor defined as,

$$\mathbf{n}_{h,n+1}^{(i)} := dev\left(\dot{\boldsymbol{\varepsilon}}_{h,n+1}^{(i)}\right) \Big/ \left\| dev\left(\dot{\boldsymbol{\varepsilon}}_{h,n+1}^{(i)}\right)\right\| = \mathbf{s}_{h,n+1}^{(i)} \Big/ \left\|\mathbf{s}_{h,n+1}^{(i)}\right\| \tag{160}$$

Substituting (160) into (159) and (159) into (158) yields,

$$\begin{aligned}\Delta\mathbf{s}_{h,n+1}^{(i)} = {} & K\left(\theta_{h,n}\right)\left(\sqrt{3}\dot{\bar{\varepsilon}}_{h,n+1}^{(i)}\right)^{m\left(\theta_{h,n}\right)-1}\left(\mathbf{I}+\left(m\left(\theta_{h,n}\right)-1\right)\mathbf{n}_{h,n+1}^{(i)}\otimes\mathbf{n}_{h,n+1}^{(i)}\right) : \Delta dev\left(\dot{\boldsymbol{\varepsilon}}_{h,n+1}^{(i)}\right) = \\ & = 2\mu\left(\dot{\bar{\varepsilon}}_{h,n+1}^{(i)}, \theta_{h,n}\right)\left(\mathbf{I}+\left(m\left(\theta_{h,n}\right)-1\right)\mathbf{n}_{h,n+1}^{(i)}\otimes\mathbf{n}_{h,n+1}^{(i)}\right) : \Delta dev\left(\dot{\boldsymbol{\varepsilon}}_{h,n+1}^{(i)}\right)\end{aligned} \tag{161}$$

and setting,

$$\Delta\mathbf{s}_{h,n+1}^{(i)} =: \mathbf{C}_{T_{n+1}}^{dev(i)} : \Delta\dot{\boldsymbol{\varepsilon}}_{h,n+1}^{(i)} \tag{162}$$

the fourth-order deviatoric consistent tangent constitutive tensor takes the form,

$$\begin{aligned}\mathbf{C}_{T_{n+1}}^{dev(i)} := {} & K\left(\theta_{h,n}\right)\left(\sqrt{3}\dot{\bar{\varepsilon}}_{h,n+1}^{(i)}\right)^{m\left(\theta_{h,n}\right)-1}\left(\mathbf{I}-\frac{1}{3}\mathbf{1}\otimes\mathbf{1}+\left(m\left(\theta_{h,n}\right)-1\right)\mathbf{n}_{h,n+1}^{(i)}\otimes\mathbf{n}_{h,n+1}^{(i)}\right) = \\ & = 2\mu\left(\dot{\bar{\varepsilon}}_{h,n+1}^{(i)}, \theta_{h,n}\right)\left(\mathbf{I}-\frac{1}{3}\mathbf{1}\otimes\mathbf{1}+\left(m\left(\theta_{h,n}\right)-1\right)\mathbf{n}_{h,n+1}^{(i)}\otimes\mathbf{n}_{h,n+1}^{(i)}\right)\end{aligned} \tag{163}$$

Sheppard-Wright constitutive model. The discrete version of the constitutive equation for a rigid viscoplastic Sheppard-Wright model at time n+1, at constant temperature at time n, is given by,

$$\mathbf{s}_{h,n+1}^{(i)} = \frac{2}{3\alpha\dot{\bar{\varepsilon}}_{h,n+1}^{(i)}}\log\left[\left(\frac{Z\left(\dot{\bar{\varepsilon}}_{h,n+1}^{(i)}, \theta_{h,n}\right)}{A}\right)^{1/n} + \sqrt{1+\left(\frac{Z\left(\dot{\bar{\varepsilon}}_{h,n+1}^{(i)}, \theta_{h,n}\right)}{A}\right)^{2/n}}\right] dev\left(\dot{\boldsymbol{\varepsilon}}_{h,n+1}^{(i)}\right) \tag{164}$$

The linearization of (164) reads,

$$\Delta\mathbf{s}_{h,n+1}^{(i)} =: \mathbf{C}_{T_{n+1}}^{dev(i)} : \Delta\dot{\boldsymbol{\varepsilon}}_{h,n+1}^{(i)} \tag{165}$$

where the fourth-order deviatoric consistent tangent constitutive tensor takes the form,

$$\mathbf{C}_{T_{n+1}}^{dev(i)} := 2\mu\left(\dot{\bar{\varepsilon}}_{h,n+1}^{(i)}, \theta_{h,n}\right)\left(\mathbf{I} - \frac{1}{3}\mathbf{1}\otimes\mathbf{1} - \mathbf{n}_{h,n+1}^{(i)}\otimes\mathbf{n}_{h,n+1}^{(i)}\right) + \tilde{\mathbf{C}}_{T_{n+1}}^{dev(i)}$$

$$\tilde{\mathbf{C}}_{T_{n+1}}^{dev(i)} = \frac{2}{3\alpha n\dot{\bar{\varepsilon}}_{h,n+1}^{(i)}}\left[\frac{\left(\frac{Z}{A}\right)^{1/n} + \left(\frac{Z}{A}\right)^{2/n}\left(\left(\frac{Z}{A}\right)^{2/n}+1\right)^{-1/2}}{\left(\frac{Z}{A}\right)^{1/n} + \left(\left(\frac{Z}{A}\right)^{2/n}+1\right)^{1/2}}\right]\mathbf{n}_{h,n+1}^{(i)}\otimes\mathbf{n}_{h,n+1}^{(i)} \tag{166}$$

where the discrete viscosity $\mu\left(\dot{\bar{\varepsilon}}_{h,n+1}^{(i)}, \theta_{h,n}\right)$ is given by,

$$\mu\left(\dot{\bar{\varepsilon}}_{h,n+1}^{(i)}, \theta_{h,n}\right) = \frac{1}{3\alpha\dot{\bar{\varepsilon}}_{h,n+1}^{(i)}}\log\left[\left(\frac{Z\left(\dot{\bar{\varepsilon}}_{h,n+1}^{(i)}, \theta_{h,n}\right)}{A}\right)^{1/n} + \sqrt{1+\left(\frac{Z\left(\dot{\bar{\varepsilon}}_{h,n+1}^{(i)}, \theta_{h,n}\right)}{A}\right)^{2/n}}\right] \tag{167}$$

2.7.2 Solution of the thermal problem

In order to solve the thermal problem, the stabilization parameters are computed using the current velocity field at time n+1, but the temperature at the time step n, instead of at the time step n+1, yielding the following modified thermal subproblem,

$$\mathbb{E}\left(\mathbb{T}_{n+1}, \mathbb{T}_n\right) + \mathbb{E}_{\tau_{e,n}^{(2)}}\left(\mathbb{T}_{n+1}\right) + \mathbb{E}_{\tau_{e,n}^{(1)}}\left(\mathbb{T}_{n+1}\right) = \mathbb{H}_{n+1} \tag{168}$$

Using a Newton-Raphson procedure to solve the nonlinear system of equations given by (168), the exact linearization of (136) yields the following incremental iterative linear system of equations,

$$\left(\mathbb{K}_{T_{n+1}}^{ther(i)} + \mathbb{K}_{\tau_{e,n}^{(1)}}^{ther} + \mathbb{K}_{\tau_{e,n}^{(2)}}^{ther}\right)\Delta\mathbb{T}_{n+1}^{(i)} = -\mathbb{R}_{\theta,n+1}^{(i)} \tag{169}$$

where the residual vector $\mathbb{R}_{\theta,n+1}^{(i)}$ is given by,

$$\mathbb{R}_{\theta,n+1}^{(i)} = \mathbb{E}\left(\mathbb{T}_{n+1}^{(i)}, \mathbb{T}_n\right) + \mathbb{E}_{\tau_{e,n}^{(2)}}\left(\mathbb{T}_{n+1}^{(i)}\right) + \mathbb{E}_{\tau_{e,n}^{(1)}}\left(\mathbb{T}_{n+1}^{(i)}\right) - \mathbb{H}_{n+1} \tag{170}$$

where $\mathbb{K}_{T_{n+1}}^{ther(i)}$, $\mathbb{K}_{\tau_{e,n}^{(1)}}^{ther}$ and $\mathbb{K}_{\tau_{e,n}^{(2)}}^{ther}$ denote the standard and the velocity and temperature stabilized contributions to the thermal consistent tangent operator, respectively, and $\Delta\mathbb{T}_{n+1}^{(i)}$ denotes the increment of temperature vector given by,

$$\Delta\mathbb{T}_{n+1}^{(i)} := \mathbb{T}_{n+1}^{(i+1)} - \mathbb{T}_{n+1}^{(i)} \tag{171}$$

Typical element entry for a node A of the residual vector $\mathbb{R}_{\theta,n+1}^{(i)}$ takes the form,

$$\begin{aligned}
\mathbb{R}_{\theta,n+1}^{(i)}\Big|_{\Omega_e}^{A} &= \int_{\Omega_e}\frac{c_0}{\Delta t}N_{\theta,A}\left(\theta_{h,n+1}^{(i)} - \theta_{h,n}\right)d\Omega + \int_{\Omega_e}N_{\theta,A}\,c_0\mathbf{v}_{h,n+1}\cdot\nabla\theta_{h,n+1}^{(i)}\,d\Omega - \\
&- \int_{\Omega_e}\nabla N_{\theta,A}\cdot\mathbf{q}_{h,n+1}^{(i)}\,d\Omega - \int_{\Omega_e}N_{\theta,A}\,\mathcal{D}_{h,n+1}^{(i)}\,d\Omega - \\
&- \int_{\Omega_e}N_{\theta,A}\,R_{h,n+1}\,d\Omega + \int_{\partial\Omega_e}N_{\theta,A}\,\overline{q}_{h,n+1}^{(i)}d\partial\Omega + \\
&+ \int_{\Omega_e}\tau_{e,n}^{(2)}\left(c_0\mathbf{v}_{h,n+1}\cdot\nabla\theta_{h,n+1}^{(i)}\right)\left(c_0\mathbf{v}_{h,n+1}\cdot\nabla N_{\theta,A}\right)d\Omega + \\
&+ \int_{\Omega_e}\tau_{e,n}^{(2)}\left(c_0\mathbf{v}_{h,n+1}\cdot\nabla\theta_{h,n+1}^{(i)}\right)N_{\theta,A}\,c_0\nabla\cdot\mathbf{v}_{h,n+1}\,d\Omega + \\
&+ \int_{\Omega_e}\tau_{e,n}^{(1)}N_{\theta,A}\,c_0\left(\nabla p_{h,n+1} - \Pi_{h,n+1}\right)\cdot\nabla\theta_{h,n+1}^{(i)}\,d\Omega
\end{aligned} \tag{172}$$

where $N_{\theta,A}$ is the temperature shape function interpolation for node A.

Typical element entries for nodes A and B of the matrices involved above take the form,

$$\mathbb{K}^{ther(i)}_{T_{n+1}}\Big|^{AB}_{\Omega_e} = \int_{\Omega_e} \frac{c_0}{\Delta t} N_{\theta,A} N_{\theta,B}\, d\Omega + \int_{\Omega_e} N_{\theta,A}\, c_0 \mathbf{v}_{h,n+1} \cdot \nabla N_{\theta,B}\, d\Omega + \\ + \int_{\Omega_e} \nabla N_{\theta,A}\, k^{(i)}_{h,n+1} \cdot \nabla N_{\theta,B}\, d\Omega - \\ - \int_{\Omega_e} N_{\theta,A}\, \frac{d\mathcal{D}^{(i)}_{h,n+1}}{d\theta_{h,n+1}} N_{\theta,B}\, d\Omega - \int_{\Omega_e} N_{\theta,A}\, \frac{dR_{h,n+1}}{d\theta_{h,n+1}} N_{\theta,B}\, d\Omega + \\ + \int_{\partial_q\Omega_e} N_{\theta,A}\, \frac{d\overline{q}^{(i)}_{h,n+1}}{d\theta_{h,n+1}} N_{\theta,B}\, d\Omega \tag{173}$$

$$\mathbb{K}^{ther}_{\tau^{(2)}_{e,n}}\Big|^{AB}_{\Omega_e} = \int_{\Omega_e} \tau^{(2)}_{e,n} \left(c_0 \mathbf{v}_{h,n+1} \cdot \nabla N_{\theta,A}\right)\left(c_0 \mathbf{v}_{h,n+1} \cdot \nabla N_{\theta,B}\right) d\Omega + \\ + \int_{\Omega_e} \tau^{(2)}_{e,n} \left(c_0 \mathbf{v}_{h,n+1} \cdot \nabla N_{\theta,B}\right) N_{\theta,A} c_0 \nabla \cdot \mathbf{v}_{h,n+1}\, d\Omega \tag{174}$$

$$\mathbb{K}^{ther}_{\tau^{(1)}_{e,n}}\Big|^{AB}_{\Omega_e} = \int_{\Omega_e} \tau^{(1)}_{e,n} N_{\theta,A}\, c_0 \left(\nabla p_{h,n+1} - \Pi_{h,n+1}\right) \cdot \nabla N_{\theta,B}\, d\Omega \tag{175}$$

3. Computational Simulations

The computational model presented in the previous sections has been implemented in the in-house developed FE software COMET [7]. In this section 3 different numerical simulations are considered. The first two examples correspond to 2D numerical simulations of a steady-state and transient, respectively, FSW processes. Numerical results obtained using COMET are compared with the numerical results provided by the in-house developed code Framework (FW) [45]. The software FW uses P2/P1 finite elements, a SUPG formulation and does not includes the thermal dilatation term in the formulation. The third example is a 3D numerical simulation of a FSW process. Results obtained using COMET are compared with experimental results obtained by Zhu and Chao [51].

3.1 2D Steady-state Coupled Thermo-mechanical Simulation of a FSW Process

The first example deals with a 2D steady-state coupled thermo-mechanical computational simulation of a FSW process. Rectangular plates of 10 cm x 6 cm at an initial uniform temperature of 500 ºC and a circular rigid tool of 0.65 cm diameter with an advancing velocity 0.115 cm/s and a rotating velocity of 490 rpm, are considered. A Sheppard-Wright material model with constant material parameters is used for the plates. The material parameters for the Sheppard-Wright model are shown in Table 1. Stabilized GLS P1/P1 triangular elements have been used in the simulation.

Figure 4 shows a scheme of the FSW process and the boundary conditions used in the 2D numerical simulation.

Table 1. Material parameters for the Sheppard-Wright model

Material	Model	A	α [mm^2 N^{-1}]	n	Q [J mol^{-1}]
Alloy 1S	Sheppard-Wright	$0.224\ 10^{13}$	0.052	4.54	177,876.4

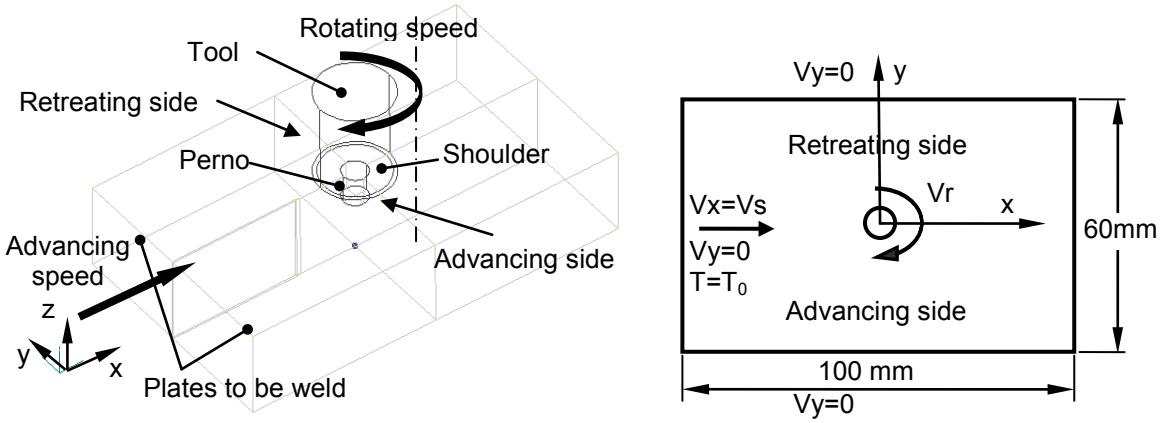

Figure 4. FSW process scheme and boundary conditions for the 2D numerical model

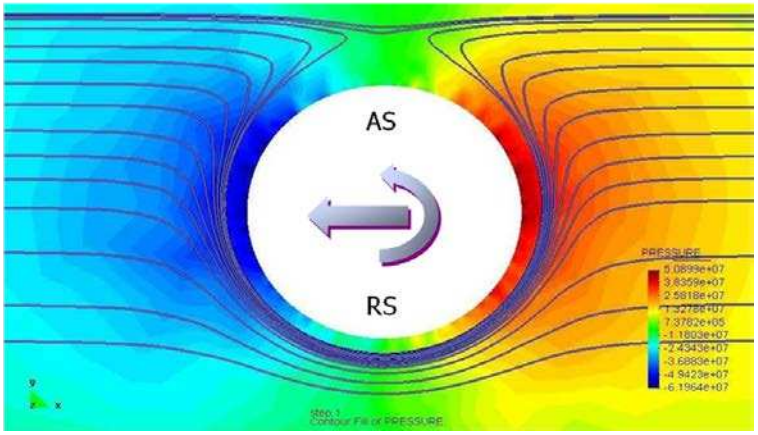

Figure 5. Pressure map distribution obtained using COMET

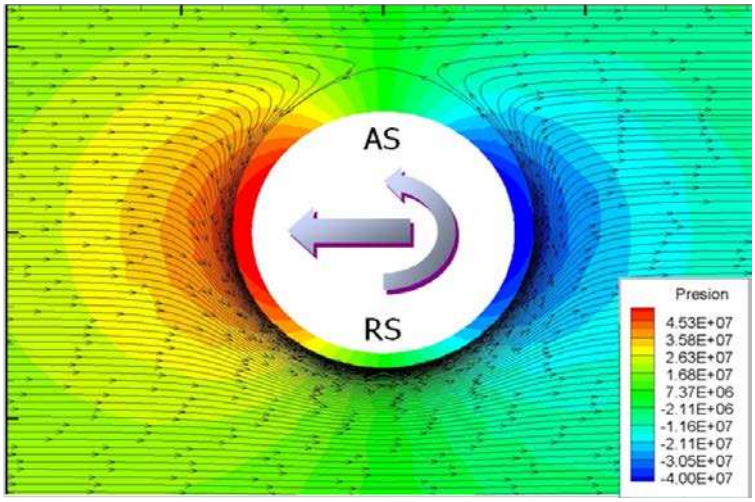

Figure 6. Pressure map distribution (compression positive) obtained using the code Framework (FW)

Figure 5 shows the pressure map and streamlines distribution obtained in this work using the in-house developed FE software COMET [7]. Those results have been compared with the results obtained for the pressure map and streamlines using the in-house developed code Framework (FW) [45], shown on Figure 6. Note that the code FW defines positive

values of the pressure as compression while in COMET it is defined the other way around. Despite the fact that different FE approximations, stabilized GLS P1/P1 elements in COMET and P2/P1 elements in FW for the mechanical problem, and different mesh sizes have been used in the simulations, the pressure maps and streamline patterns obtained look quite similar. As expected compression and traction pressures are located on the forward and backward sides of the tool, respectively. Due to the advancing and rotating velocity of the tool, an advancing side (AS) and a retreating side (RS) are formed.

3.2 2D Transient Coupled Thermo-mechanical Simulation of a FSW Process

This example shows the 2D transient coupled thermo-mechanical computational simulation of a FSW process [52]. Two rectangular aluminium plates of 10 cm x 5 cm and a circular tool of 0.6 cm diameter are considered. An advancing velocity of 40 cm/min and different rotational velocities of 0, 20, 40 and 80 rpm have been considered. An initial and environmental temperature of 20 ºC has been assumed. A Norton-Hoff material model has been used for the aluminium alloy plates. The 2 parameters of the Norton-Hoff material model, assumed here to be constant, are given in Table 2. The thermal properties of the aluminium alloy are given in Table 3. Influence of the dilatation parameter has been analysed and simulations assuming a zero-dilatation coefficient have been also carried out.

Table 2. Parameters for the Norton-Hoff material model of the aluminium alloy plates

Material	Model	K [MPa seg]	m
Aluminium Alloy	Norton-Hoff	100	0.12

Table 3. Thermal material parameters for the aluminium alloy plates

Material	α [ºC^{-1}]	ρ [Kg/m^3]	Cp [J/Kg ºC]	k [W/m ºC]
Aluminum Alloy	2.4E-05	2.7E+03	875	120

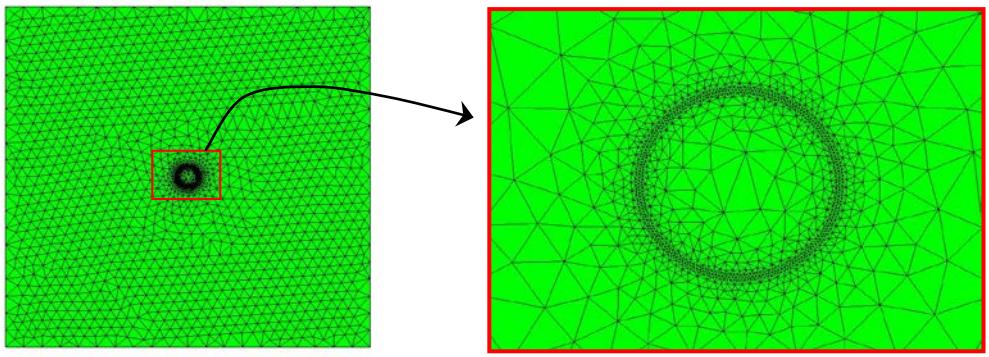

Figure 7. Finite element discretization of the plates and tool using P1/P1 GLS pressure stabilized elements. Detail of the finite element discretization around the tool area

Figure 7 shows the finite element discretization of the plates and tool using P1/P1 GLS pressure stabilized elements, including a detail of the finite element discretization around the tool area. In order to analyse the mesh-dependency in the maximum temperature, a mesh convergence analysis for a rotational velocity of 80 rpm and three different meshes, with 4,000, 5,800 and 8,100 elements, representing element sizes at the limit layer of 0.05, 0.01 and 0.005 cm, respectively, has been performed.

Table 4 shows the maximum temperature obtained in the simulations for the 5,800 element mesh and the different rotational velocities using the in-house developed FE software

COMET [7]. Those results are compared with the ones provided by the numerical code FW. As Table 4 shows, an excellent agreement exists between the results given by COMET and the ones given by FW.

Table 5 collects the results obtained for the maximum temperature for each one of the meshes. No mesh-dependency of the maximum temperature has been found.

Figure 8 shows the temperature maps obtained at the end of the simulation for three different rotational velocities, 80, 40 and 20 rpm, using the FE codes COMET and FW. The temperature maps predicted by COMET compare well with the ones given by FW.

Table 4. Maximum temperature obtained for different rotational velocities using the FE codes COMET (using the mesh of 5,800 elements) and FW

Rotational velocity [rpm]	COMET T [ºC]	FW T [ºC]
0	90	92
20	112	114
40	160	162
80	271	273

Table 5. Mesh convergence analysis for a rotational velocity of 80 rpm

Number of elements	Element size at the limit layer [cm]	Maximum temperature [ºC]
4,000	0.05	272
5,800	0.01	271
8,100	0.005	271

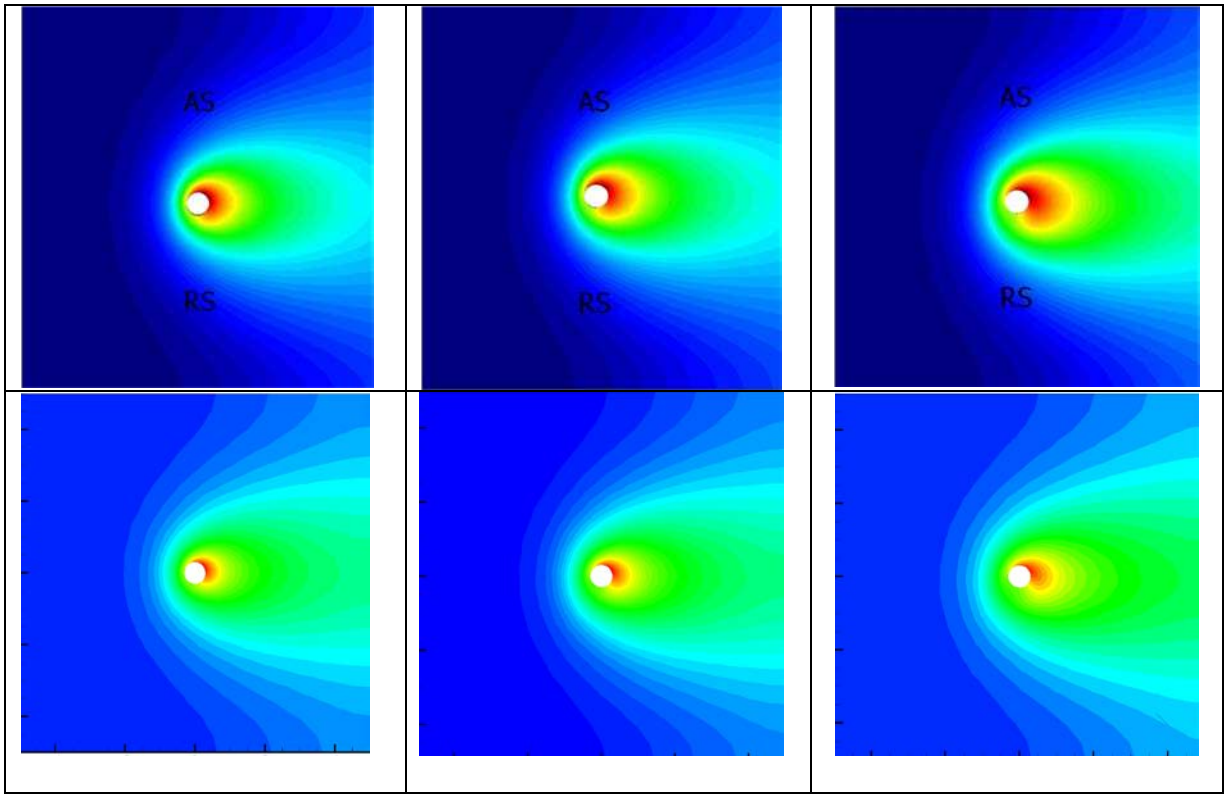

Figure 8. Temperature map distributions at the end of the simulation for different tool rotational velocities using COMET (Top) and FW (Bottom). From left to right: Tool rotational velocities of 80 rpm, 40 rpm and 20 rpm

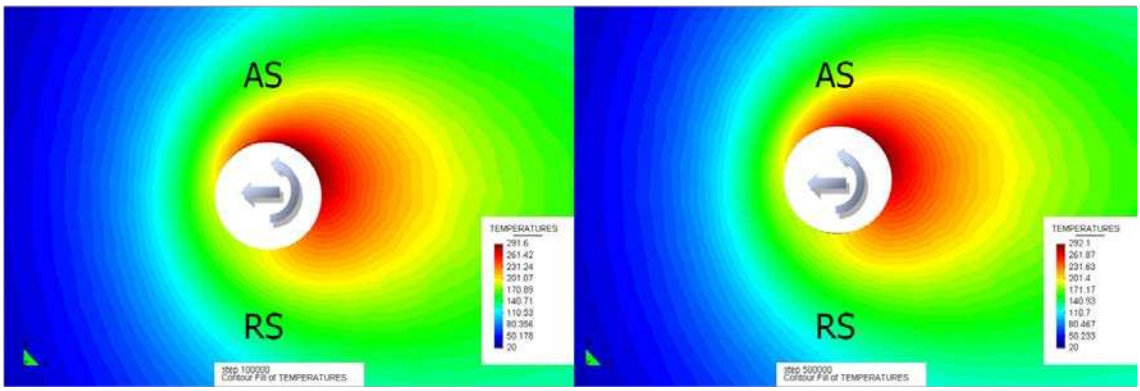

Figure 9. Temperature map distributions at the end of the simulation for a tool rotational velocity of 80 rpm using COMET; (left) α=0 ºC^{-1}; (right) α=2.40e-5 ºC^{-1}

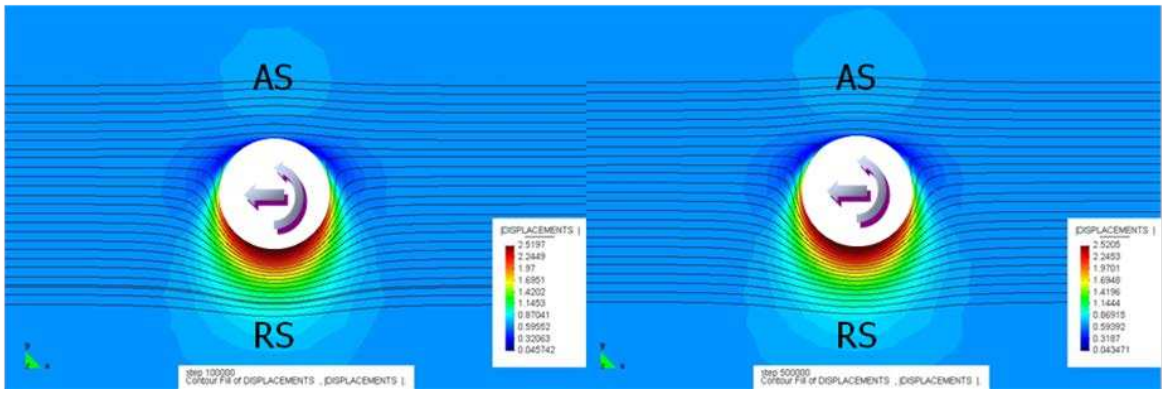

Figure 10. Velocity norm map and streamlines at the end of the simulation for a tool rotational velocity of 80 rpm using COMET; (left) α=0 ºC^{-1}; (right) α=2.40e-5 ºC^{-1}

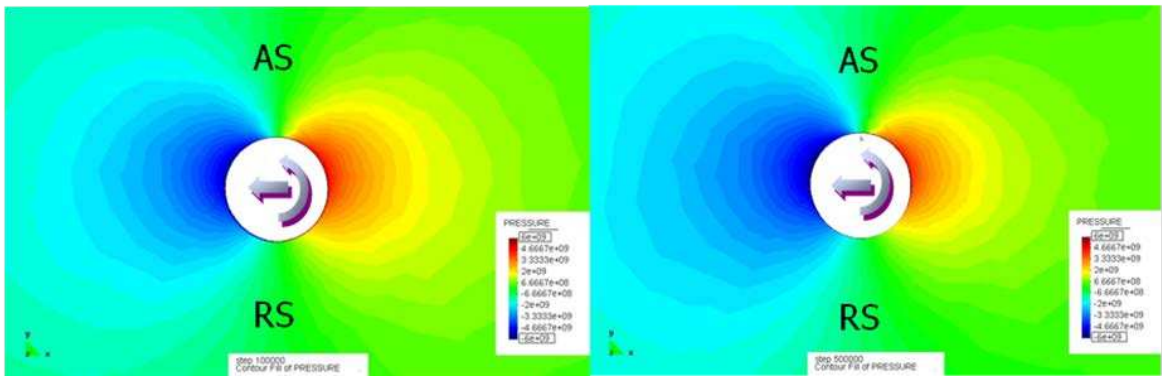

Figure 11. Pressure map and streamlines at the end of the simulation for a tool rotational velocity of 80 rpm using COMET; (left) α=0 ºC^{-1}; (right) α=2.40e-5 ºC^{-1}

Figures 9 and 10 show the temperature map and the velocity map and streamlines, respectively, for a tool rotational velocity of 80 rpm, excluding and including the thermal dilatation term. As it is shown in those figures, the influence of the thermal dilatation coefficient is negligible and no differences can be seen on the temperature map, velocity map or streamlines.

Similarly, Figure 11 shows the pressure map for a tool rotational velocity of 80 rpm, excluding and including the thermal dilatation term. Here some influence of the thermal dilatation coefficient on the pressure map distribution can be observed. Nevertheless, as it is shown in Figure 12, the influence of the thermal dilatation term is very small. Therefore, the

thermal volumetric deformation rate can be considered as negligible and the material flow can be considered as fully incompressible.

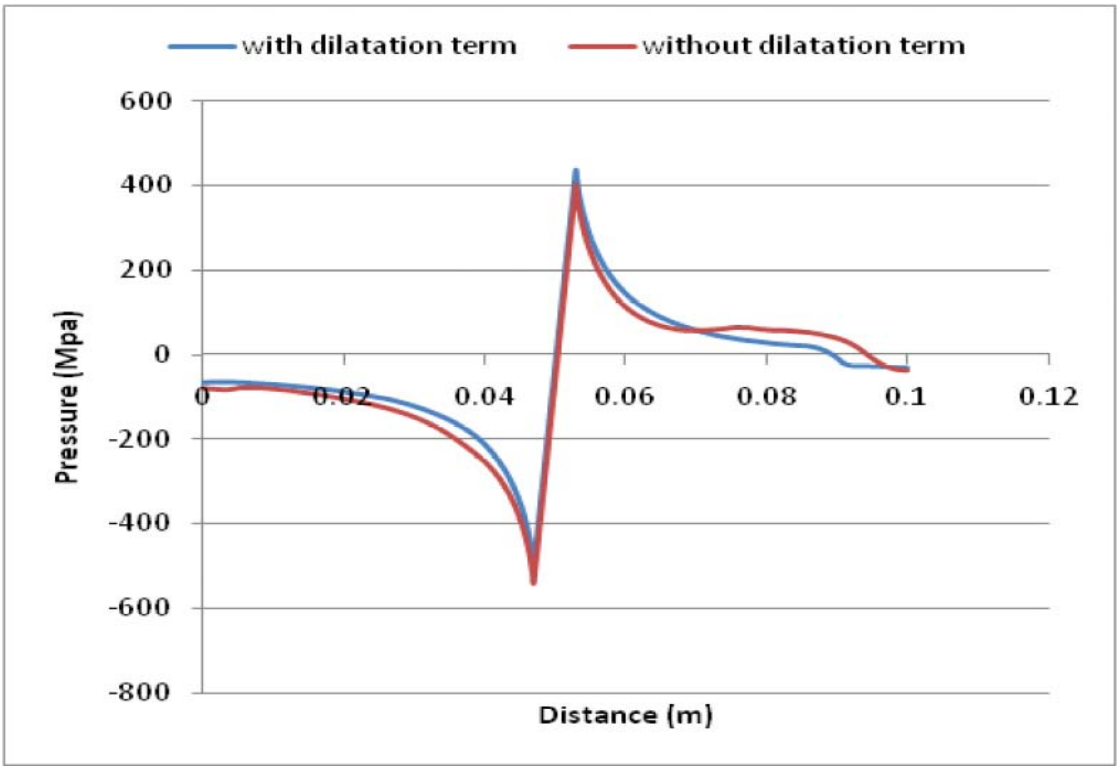

Figure 12. Pressure distribution along the welding line obtained with COMET, with and without the thermal deformation term, for a tool rotational velocity of 80 rpm

3.3 3D Transient Coupled Thermo-mechanical Simulation of a FSW Process

This example shows the 3D computational simulation of a FSW process [53]. The geometry of the tool, workpieces and backplate has been included in the simulation. The tool is cylindrical. A simplified model of the tool probe and the shoulder part has been considered, avoiding the discretization of the shoulder scroll and the probe thread.

The diameters of the tool shoulder and tool probe are 19.05 mm (3/4'') and 6.35 mm (1/4''), respectively. The heights of the tool shoulder and probe are 50 mm and 3 mm, respectively. The two workpieces have a length of 300 mm (along the x-axis in the welding direction), a total width for the 2 workpieces of 200 mm (along the y-axis in the transversal direction) and a thickness of 3.18 mm (1/8''). The backplate has a length of 300 mm, a width of 210 mm and a thickness of 19 mm.

Figure 13 shows the geometry of the tool, workpieces and backplate for a transversal section along the x-axis and the FE discretization used in the simulation where the rotational axis of the tool is located at x=0 and y=0.

The tool rotational velocity and advancing velocity are V_R = 500 rpm and V_W = 101 mm/min (4 inch/min), respectively. The material of the workpieces is an AISI 304 L. A Sheppard-Wright material model has been used to characterize the material behavior of the workpieces. The values of the constants for the Sheppard-Wright material were obtained from Jorge Jr. et al. [50] and they are shown in Table 5, being $\alpha = 0.012$ MPa^{-1}, $Q = 401$ kJ mol^{-1}, $A = 8.30\ 10^{15}$ and $n = 4.32$. The tool and backplate have been considered as thermo-rigid bodies.

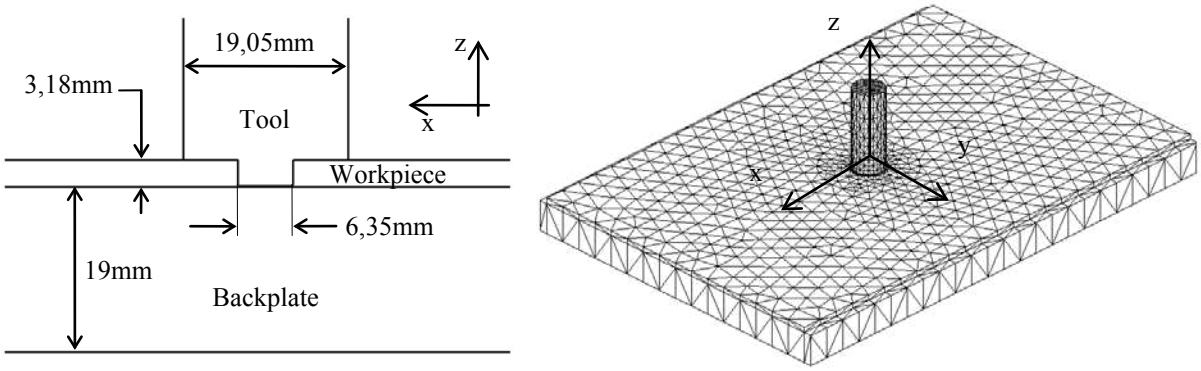

Figure 13. Detail of the geometry of the tool, workpieces and backplate for a transversal section along the x-axis (left) and FE mesh used in the simulation with FW (right)

Table 5. Material parameters for the Sheppard-Wright model

Material	Model	A	α [MPa^{-1}]	n	Q [kJ mol^{-1}]
AISI 304 L	Sheppard-Wright	$8.3\ 10^{15}$	0.012	4.32	401

Table 6. Thermal properties for the workpieces (SS 304L), tool (steel) and backplate (steel)

Material	ρ [Kg m^{-3}]	Cp [J Kg^{-1} ºC^{-1}]	k [W m^{-1} ºC^{-1}]	h [W m^{-2} ºC^{-1}]	R [m^2 ºC W^{-1}]	ε
Workpiece (SS 304L)	$8.0\ 10^3$	$0.51\ 10^3$	21.4	10	$1.67\ 10^{-6}$	0.17
Tool (steel)	$7.8\ 10^3$	$0.46\ 10^3$	43.0	10	$1.67\ 10^{-6}$	0.8
Backplate (steel)	$7.8\ 10^3$	$0.46\ 10^3$	43.0		$1.67\ 10^{-6}$	

Table 7. Boundary/Volume prescribed conditions for the workpieces, tool and backplate, for the mechanical and thermal problems

Body	Boundary/Domain	Mechanical Problem	Thermal Problem
Workpieces	Inlet	$V_x=-V_W,\ V_y=0,\ V_z=0$	T=25°C
	Outlet	P=0	Adiabatic
	Bottom	$V_x=-V_W,\ V_y=0,\ V_z=0$	Thermal contact
	Top	$V_z=0$	Convection-radiation
	Two sides	$V_x=-V_W,\ V_y=0\ ,\ V_z=0$	Adiabatic
	Shoulder	$V_{tang}=V_R.r,\quad R_P \le r \le R_S$	Thermal contact
	Probe	$V_{tang}=V_R.r,\quad 0 \le r \le R_P$	Thermal contact
Backplate	Volume	$V_x=-V_W,\ V_y=0,\ V_z=0$	
	Inlet		T=25°C
	Outlet		Adiabatic
	Top		Thermal contact
	Bottom		Adiabatic
	Two sides		Adiabatic
Tool	Volume	$V_{tang}=V_R.r,\quad 0 \le r \le R_S$	
	Side		Convection-radiation
	Top		Convection-radiation
	Shoulder		Thermal contact
	Probe		Thermal contact

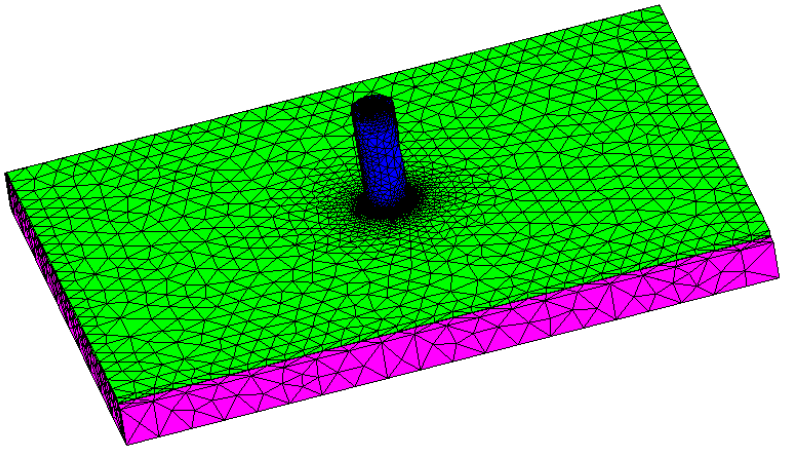

Figure 14. Finite element mesh of the tool, workpieces and backplate

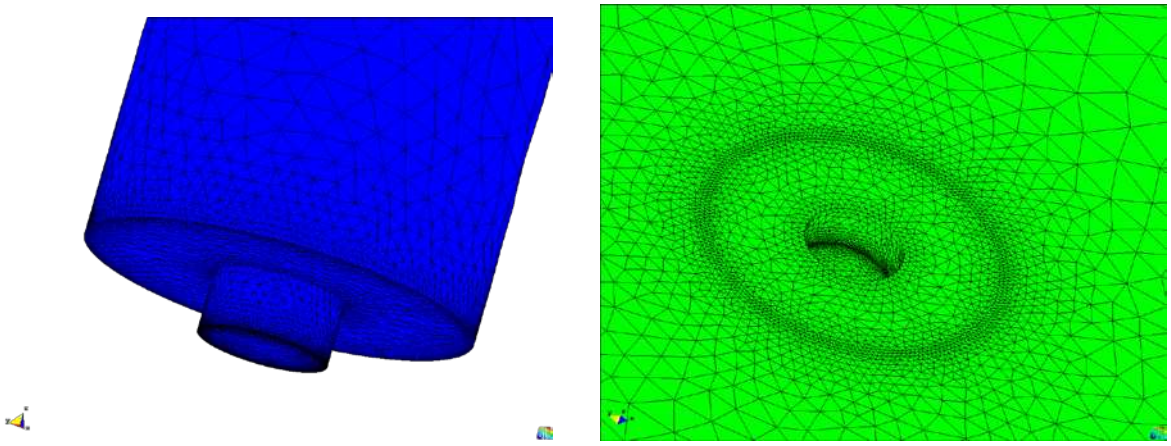

Figure 15. Details of the finite element mesh of the tool (left) and workpieces (right)

The material thermal properties, material density, heat capacity, thermal conductivity, heat transfer convection coefficient, thermal contact resistance coefficient and relative emissivity, for the workpieces (SS 304L), tool (steel) and backplate (steel) are given in Table 6.

Geometry data, process parameters and material properties used in the simulation were taken from Zhu and Chao [51], in order to be able to compare their experimental results with the numerical results obtained in this work.

Table 7 shows the boundary conditions used in the simulation, both for the mechanical (velocity and tractions) and the thermal (temperatures and heat fluxes) problems. As usual, the prescribed tool advancing velocity has been imposed as a minus prescribed advancing velocity to the workpieces and backplate, keeping fixed the tool. The prescribed rotational velocity has been applied on the tool itself. Full stick friction conditions and thermal contact boundary conditions on the tool shoulder/workpieces and on the tool probe/workpieces contact interfaces have been considered. Thermal contact boundary conditions have been also considered on the contact surface between the workpieces (bottom surface) and the backplate (top surface). The heat transfer coefficient for the thermal contact boundary conditions is 0.6 10^6 W m^{-2} $ºC^{-1}$. Convection/radiation boundary conditions have considered on the top and lateral surfaces of the tool and on the top surface of the workpieces which is not in contact with the tool shoulder. Adiabatic boundary conditions have been considered on the outlet and two external lateral surfaces of the workpieces, as well as on the outlet, bottom and two lateral

surfaces of the backplate. On the inlet surfaces of the workpieces and the backplate, the temperature has been prescribed to the environmental one. The initial and environmental temperature is 25ºC.

A finite element mesh consisting of 116,414 linear tetrahedra and 21,494 nodal points has been considered in the simulation. Prescribed advancing and rotational velocities have been imposed in an incremental way, using 1,000 time steps. A uniform time step of 0.1 sec has been considered. The full FSW numerical simulation has been done using 2,000 time steps. Computing time for the whole simulation, using a personal computer with 2 Gb RAM, was around 74 hours.

Figure 14 shows a view of the finite element mesh of the tool, workpieces and backplate. Details of the finite element mesh of the tool and workpieces are shown on Figure 15.

Figure 16 shows the temperature map distribution at the end of the numerical simulation. It can be clearly seen the convection effect due to the advancing tool speed. A detail of the temperature map on the tool and workpieces at the welding line section at the end of the simulation is shown in Figure 17. As it can be seen, extremely high temperature gradients through the thickness of the workpieces take place below the tool shoulder area.

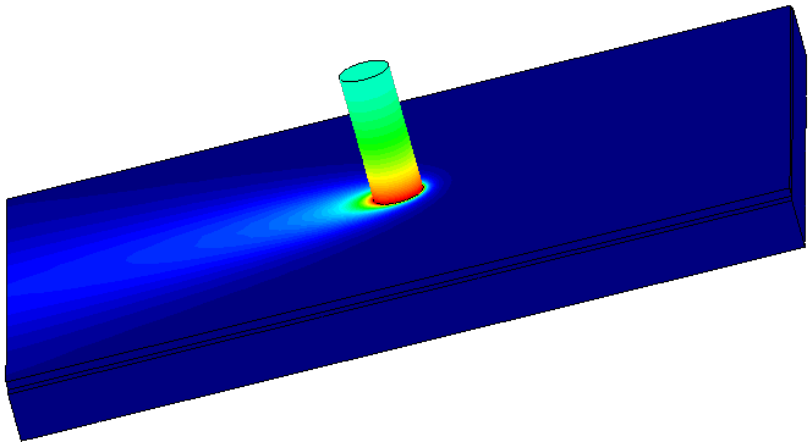

Figure 16. Temperature map distribution at the end of the simulation

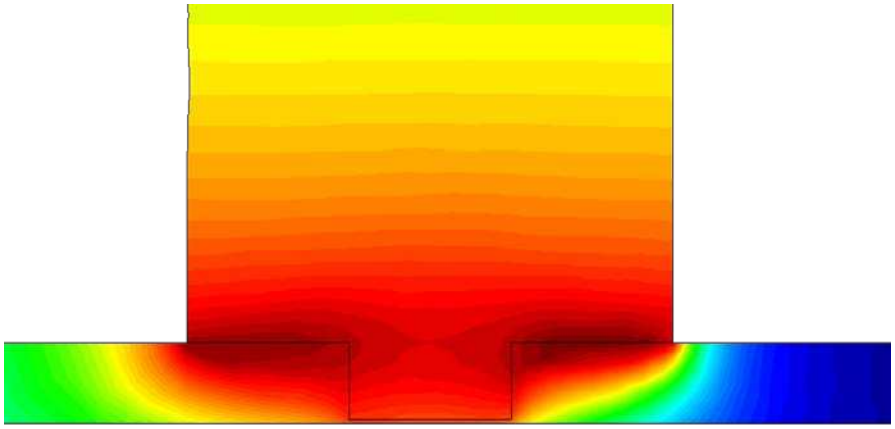

Figure 17. Temperature map distribution at the welding line section at the end of the simulation

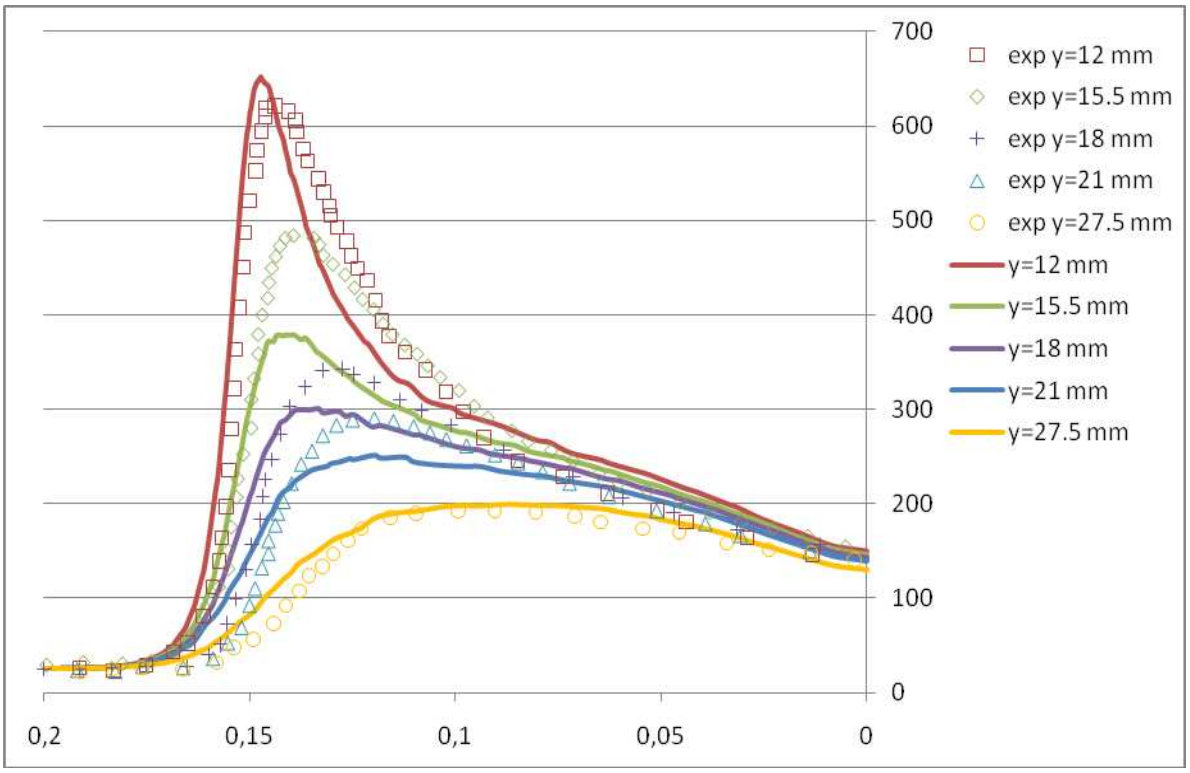

Figure 18. Comparison between the experimental results (symbols) reported by Zhu and Chao [51] and the numerical results (lines) obtained for the temperature at the end of the simulation using COMET, along five different lines parallel to the welding line on the top surface of the workpiece

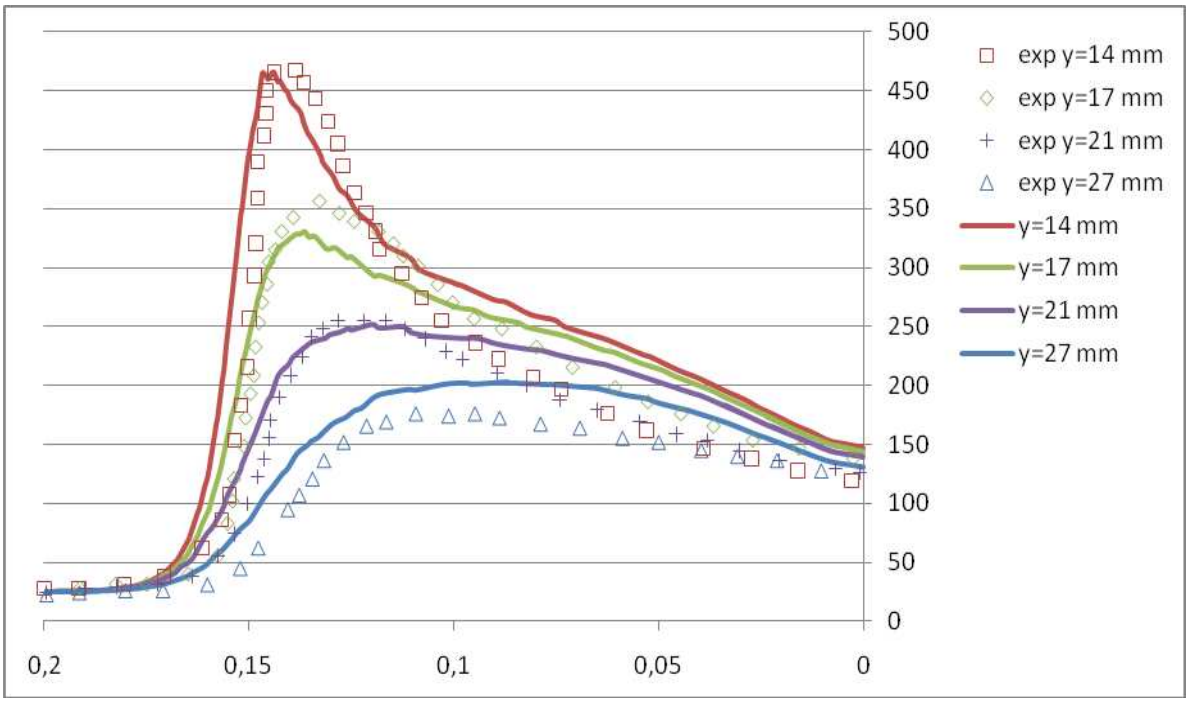

Figure 19. Comparison between the experimental results (symbols) reported by Zhu and Chao [51] and the numerical results (lines) obtained for the temperature at the end of the simulation using COMET, along four different lines parallel to the welding line on the bottom surface of the workpiece

Figures 18 and 19 show a comparison between the experimental results reported by Zhu and Chao [51] and the numerical results obtained for the temperature along five different lines parallel to the welding line on the top surface (z=3.18 mm) and four different lines parallel to the welding line on the bottom surface (z=0.0 mm) of the workpiece, respectively.

The five lines considered on the top of the surface (z=3.18 mm) of the workpiece are located at y=12 mm, y=15.5 mm, y=18 mm, y=21 mm and y=27.5 mm of the welding line. As it is shown on Figure 18, numerical results obtained compare well with the experimental ones. The peak temperature for the lines located at y=12 mm of the welding line, the one which is closest to the welding line, is catched remarkably well, both in position and value, by the numerical simulation. Peak temperatures for lines located at y=15.5 mm, y=18 mm and y=21 mm of the welding line seem to be underestimated by the numerical simulation. The reason behind this underestimation of the temperature could be that a finer mesh is still needed in those areas. Numerical and experimental temperatures match remarkably well along the line located at y=27.5 mm of the welding line.

The four lines considered on the bottom surface (z=0.0 mm) of the workpiece are located at y=14 mm, y=17 mm, y=21 mm and y=27 mm of the welding line. As it is shown on Figure 19, numerical results obtained compare well with the experimental ones. Once again, the peak temperature for the line located at y=14 mm of the welding line, the one which is closest to the welding line, is catched remarkably well, both in position and value, by the numerical simulation. Peak temperatures for lines located at y=17 mm and y=21 mm are also remarkably well catched, both in position and value, while the peak temperature for the line located at y=27 mm of the welding line is clearly overestimated. Furthermore, in general, an overestimation of the temperature distribution can be also seen along each one of the lines, being more evident for the lines located farther from the welding line. Once again, the reason behind this discrepancy can be that the mesh is not finer enough in those areas and across the thickness, to properly catch the high thermal gradients arising during the process.

4. Concluding Remarks

The computational modeling and numerical simulation of FSW processes has been addressed. Strong emphasis has been placed on developing, within the paradigmatic framework of the multiscale stabilization methods, a suitable stabilized coupled thermomechanical formulation for the numerical simulation of FSW processes, using an Eulerian description. Constitutive equations for the subgrid scale variables (velocity and temperature) have been proposed. Remarkably, a thermal conductivity for the thermal subgrid scale constitutive equation has been introduced and it has been found that the thermal conductivity for the termal subgrid scale constitutive equation can be expressed as the Peclet number multiplied by the thermal conductivity of the material. Using those constitutive equations, an approximation of the subgrid scale variables (velocity and temperature) and their associated stabilization parameters has been proposed. In particular Algebraic Subgrid Scale (ASGS) and Orthogonal Subgrid Scale (OSGS) methods have been considered. Remarkably, it has been shown that well known classical formulations, such as the Galerkin Least-Squares (GLS) or Streamline Upwind/Petrov-Galerkin (SUPG) methods, can be recovered as particular cases of the multiscale stabilization framework considered.

An assessment of the influence of the thermal expansion term on the temperature, velocity and pressure maps, has been done for some simple 2D benchmark tests. It has been shown that its influence is very small and, in fact, this term can be neglected in the formulation, leading to a fully incompressible problem. Let us remark that a stabilization of the pressure would be still needed if we decide to include this term in the formulation.

The computational model developed has been implemented in the FE software COMET developed by CIMNE and it has been validated through the numerical simulation of 2D and 3D FSW processes. In the 2D numerical simulation of a FSW process, different analyses have been carried out for four different rotational velocities. A very good agreement has been found between the maximum temperatures obtained in this work, using COMET, and the ones given by FW, for all four rotational velocities considered. In the 3D numerical simulation of a FSW process, a finite element discretization of the tool, workpieces and backplate has been considered. The numerical simulation of 3D FSW processes is a complex and computational demanding task. High temperature gradients, mainly through the thickness, are involved and a very fine discretization in the critical areas and small time steps are needed to get reliable and accurate results. Numerical results obtained for the temperature along different lines parallel to the welding line on the top and bottom surfaces of the workpiece have been obtained and compared with experimental results available. Numerical results for the temperature along those lines compare well with the experimental ones. Peak temperatures (and their positions) for the lines located closest to the welding line, fit remarkably well with the experimental results. Peak temperatures obtained for some of the lines located a little bit further of the welding line, in particular on the top surface of the workpiece, are somehow underestimated compared with the experimental ones. Most likely a finer mesh should also be used in those areas to catch the high temperature gradients arising during the process.

Acknowledgements

This research work has been partially carried out within the framework of the STREP project "Detailed Multi-Physics Modeling of Frictional Stir Welding" (DEEPWELD) of the 6th Framework Programme of the European Community, the PROFIT project "Nuevas Herramientas para Optimizar el Proceso de Soldadura por Fricción" (FSWNET) of the "Ministerio de Educación y Ciencia" of Spain and the project "Simulación Numérica del Proceso de Soldadura Mediante Batido por Fricción" (FSW) of the "Plan Nacional de I+D+I (2004-2007)" of the "Ministerio de Educación y Ciencia" of Spain. Those financial supports are gratefully acknowledged.

References

1. C. Agelet de Saracibar, M. Chiumenti, Q. Valverde, M. Cervera (2004), "On the orthogonal subgrid scale pressure stabilization of small and finite deformation J2 plasticity", *Monograph Series on Computational Methods in Forming Processes,* C. Agelet de Saracibar (ed.), Monograph CMFP 2, CIMNE (2004)
2. C. Agelet de Saracibar, M. Chiumenti, Q. Valverde, M. Cervera (2006), "On the orthogonal subgrid scale pressure stabilization of finite deformation J2 plasticity", *Computer Methods in Applied Mechanics and Engineering* 195 (2006) 1224-1251
3. A. Askari, S. Silling, B. London, M. Mahoney (2003), "Modeling and analysis of friction stir welding processes"*, Proceedings of the 4th International Symposium on Friction Stir Welding (4ISFSW)*, *GKSS Workshop*, Park City, Utah, USA, May 14-16, 2003

4. G. Bendzsak, T. North, C. Smith (2000), "An experimentally validated 3D model for friction stir welding", *Proceedings of the 2nd International Symposium on Friction Stir Welding (2ISFSW)*, Gothenburg, Sweden, June 27-29, 2000
5. G. Bendzsak, T. North, C. Smith (2000), "Material properties relevant to 3-D FSW modeling", *Proceedings of the 2nd International Symposium on Friction Stir Welding (2ISFSW)*, Gothenburg, Sweden, June 27-29, 2000
6. G. Buffa, J. Hua, R. Shivpuri, L. Fratini (2006), "A continuum-based fem model for friction stir welding – Model development", *Materials Science and Engineering* A 419 (2006) 389-396
7. M. Cervera, C. Agelet de Saracibar, M. Chiumenti (2002), "COMET – A Coupled Mechanical and Thermal Analysis Code. Data Input Manual. Version 5.0", *Technical Report IT-308,* CIMNE, 2002
8. M. Cervera, M. Chiumenti, Q. Valverde, C. Agelet de Saracibar (2003), "Mixed linear/linear simplicial elements for incompressible elasticity and plasticity", *Computer Methods in Applied Mechanics and Engineering* 192 (2003) 5249-5263
9. M. Cervera, M. Chiumenti, C. Agelet de Saracibar (2004), "Softening, localization and stabilization: capture of discontinuous solutions in J2 plasticity", *International Journal for Numerical and Analytical Methods in Geomechanics* 28 (2004) 373-393
10. M. Cervera, M. Chiumenti, C. Agelet de Saracibar (2004), "Shear band localization via local J2 continuum damage mechanics", *Computer Methods in Applied Mechanics and Engineering* 193 (2004) 849-880
11. Y. Chao, X. Qi, W. Tang (2003), "Heat transfer in friction stir welding – Experimental and numerical studies", *Journal of Manufacturing Science and Engineering* 125 (2003) 138-145
12. C.M. Chen, R. Kovacevic (2003), "Finite element modeling of friction stir welding – thermal and thermomechanical analysis", *International Journal of Machine Tools and Manufacture* 43 (2003) 1319-1326
13. M. Chiumenti, Q. Valverde, C. Agelet de Saracibar, M. Cervera (2002), "A stabilized formulation for incompressible elasticity using linear displacement and pressure interpolations", *Computer Methods in Applied Mechanics and Engineering* 191 (2002) 5253-5264
14. M. Chiumenti, Q. Valverde, C. Agelet de Saracibar, M. Cervera (2004), "A stabilized formulation for incompressible plasticity using linear triangles and tetrahedra", *International Journal of Plasticity* 20 (2004) 1487-1504
15. D. Christ, M. Cervera, M. Chiumenti, C. Agelet de Saracibar (2003), "A mixed finite element formulation for incompressibility using linear displacement and pressure interpolations", Monograph 77, CIMNE, 2003
16. R. Codina (2000), "Stabilization of incompressibility and convection through orthogonal sub-scales in finite element methods", *Computer Methods in Applied Mechanics and Engineering* 190 (2000) 1579-1599
17. R. Codina (2002), "Stabilized finite element approximation of transient incompressible flows using orthogonal subscales", *Computer Methods in Applied Mechanics and Engineering* 191 (2002) 4295-4321

18. R. Codina, J. Blasco (2000), "Stabilized finite element method for transient Navier-Stokes equations based on pressure gradient projection", *Computer Methods in Applied Mechanics and Engineering* 182 (2000) 287-300

19. P. Colegrove, M. Painter, D. Graham, T. Miller (2000), "Three dimensional flow and thermal modelling of the friction stir welding process", *Proceedings of the 2nd International Symposium on Friction Stir Welding (2ISFSW)*, Gothenburg, Sweden, June 27-29, 2000

20. P. Colegrove, H. Shercliff, P. Threadgill (2004), "Modelling the friction stir welding of aerospace alloys", *Proceedings of the 5th International Symposium on Friction Stir Welding (5ISFSW),* Metz, France, September 14-16, 2004

21. K. Colligan (1999), "Material flow behaviour during friction stir welding of aluminium", *Weld Journal*, July 1999, 229-237

22. T. De Vuyst, L. D'Alvise, A. Simar, B. de Meester, S. Pierret (2005), "Finite element modelling of friction stir welding aluminium alloys plates – Inverse analysis using a genetic algorithm", *Welding in the World*, 49, 3/4, 44-55, 2005

23. T. De Vuyst, L. D'Alvise, A. Simar, B. de Meester, S. Pierret (2004), "Inverse analysis using a genetic algorithm for the finite element modelling of friction stir welding", *Proceedings of the 5th International Symposium on Friction Stir Welding (5ISFSW),* Metz, France, September 14-16, 2004

24. T. De Vuyst, L. D'Alvise, A. Robineau, J.C. Goussain (2006), "Material flow around a friction stir welding tool – Experiment and Simulation", *Proceedings of the 8th International Seminar on Numerical Analysis of Weldability*, Graz, Austria, September 25-27, 2006

25. T. De Vuyst, L. D'Alvise, A. Robineau, J.C. Goussain (2006), "Simulation of the material flow around a friction stir welding tool", *Proceedings of the 6th International Symposium on Friction Stir Welding (6ISFSW)*, Saint-Sauveur, Quebec, Canada, October 10-13, 2006

26. T. Dickerson, H. Shercliff, H. Schmidt (2003), "A weld marker technique for flow visualization in friction stir welding", *Proceedings of the 4th International Symposium on Friction Stir Welding (4ISFSW)*, Park City, Utah, USA, May 14-16, 2003

27. P. Dong, F. Lu, J. Hong, Z. Cao (2000), "Analysis of weld formation process in friction stir welding", *Proceedings of the 2nd International Symposium on Friction Stir Welding (2ISFSW)*, Gothenburg, Sweden, June 27-29, 2000

28. M. Guerra, C. Schmids, J.C. McClure, L.E. Murr, A.C. Nunes (2003), "Flow patterns during friction stir welding", *Material Characterization* 49 (2003) 95-101

29. P. Heurtier, C. Desrayaud, F. Montheillet (2002), "A thermomechanical analysis of the friction stir process", *Materials Science Forum* 396 (2002) 1537-1542

30. P. Heurtier, M.J. Jones, C. Desrayaud, J.H. Driver, F. Montheillet, D. Allehaux (2006), "Mechanical and thermal modeling of friction stir welding", *Journal of Materials Proccesing Technology* 171 (2006) 348-357

31. T.J.R. Hughes, G.R. Feijóo, L. Mazzei, J.-B. Quincy, The variational multiscale method – a paradigm for computational mechanics, *Computer Methods in Applied Mechanichs and Engineering* 166 (1998) 3–24

32. M. Khandkar, J. Khan (2001), "Thermal modeling of overlap friction stir welding for AL alloys", *Journal of Materials Processing and Manufacturing Science* 10 (2001) 91-105

33. M. Khandkar, J. Khan, A. Reynolds (2003), "Prediction of temperature distribution and thermal history during friction stir welding: Input torque based model", *Science and Technology of Welding and Joining* 8, 3 (2003) 165-174

34. M. Langerman, E. Kvalvik (2003), "Modeling plasticized aluminum flow and temperature fields during friction stir welding", *Proceedings of the 6th ASME-JSME Thermal Engineering Joint Conference*, Hapuna Beach Prince Hotel, Kohala Coast, Hawaii Island, Hawaii, USA, March 16-20, 2003

35. Y. Li, L.E. Murr, J.C. McClure (1999), "Flow visualization and residual microstructures associated with the friction-stir welding of 2024 aluminium to 6061 aluminium", *Materials Science and Engineering: A* 271 (1999) 213-223

36. J.C. McClure, W. Tang, L.E. Murr, X. Guo, Z. Feng, J.E. Gould (1998), "A thermal model of friction stir welding" *Proceedings of the 5th International Conference on Trends in Welding Research*, Pine Mountain, Georgia, USA, June 1-5, 1998, pp. 590-595

37. N. Nikiforakis (2005), Towards a whole system simulation of FSW, *Proceedings of the 2nd FSW Modelling and Flow Visualisation Seminar*, GKSS Forschungszentrum, Geesthacht, Germany, January 31-February 1, 2005

38. H. Schmidt, J. Hattel (2004), "Modelling thermo mechanical conditions at the tool/matrix interface in Friction Stir welding", *Proceedings of the 5th International Symposium on Friction Stir Welding (5ISFSW)*, Metz, France, September 14-16, 2004

39. A.P. Reynolds, T.U. Seidel (2001), "Visualization of the material flow in AA2195 friction-stir welds using a marker insert technique", *Metallurgical and Material Transactions A* 32A (2001) 2879-2884

40. T.U. Seidel, A.P. Reynolds (2003), "Two-dimensional friction stir welding process model based on fluid mechanics", *Science and Technology of Welding and Joining* 8, 3 (2003) 175-183

41. H.R. Shercliff, M.J. Russell, A. Taylor, T.L. Dickerson (2005), "Microstructural modeling in friction stir welding of 2000 series aluminium alloys", *Mécanique & Industries* 6 (2005) 25-35

42. Q. Shi, T. Dickerson, H. Shercliff (2003), "Thermo-mechanical FE modeling of friction stir welding of AL-2024 including tool loads", *Proceedings of the 4th International Symposium on Friction Stir Welding (4ISFSW)*, Park City, Utah, USA, May 14-16, 2003

43. M. Song, R. Kovacevic (2003), "Numerical and experimental study of the heat transfer process in friction stir welding", *Journal of Engineering Manufacture* 217, Part B (2003) 73-85

44. P. Ulysse (2002), "Three-dimensional modeling of the friction stir welding process", *International Journal of Machine Tools and Manufacture* 42 (2002) 1549-1557

45. S.A. Urquiza, M.J. Venere (2002), "An application framework architecture for FEM and other related solvers", *Mecánica Computacional XXI*, 3099-3109, 2002

46. S. Xu, X. Deng, A.P. Reynolds, T.U. Seidel (2001), "Finite element simulation of material flow in friction stir welding", *Science and Technology of Welding and Joining* 6 (3) 191-193, 2001

47. S. Xu, X. Deng (2003), "Two and three-dimensional finite element models for the friction stir welding process", *Proceedings of the 4th International Symposium on Friction Stir Welding (4ISFSW)*, Park City, Utah, USA, May 14-16, 2003

48. S. Xu, X. Deng (2004), "Two and three-dimensional finite element models for the friction stir welding process", University of South Carolina, Department of Mechanical Engineering, Columbia, South Carolina 29208, USA, 2004

49. H. Zhao (2005), "Friction Stir Welding (FSW) Simulation Using an Arbitrary Lagrangian-Eulerian (ALE) Moving Mesh Approach", Ph.D. Dissertation, West Virginia University, Morgantown, West Virginia, USA, w : http://hdl.handle.net/10450/4367

50. A.M. Jorge Jr., O. Balancín, "Prediction of steel flow stresses under hot working conditions", *Materials Research*, Vol. 8, No. 3, 309-315, 2004

51. X.K. Zhu, Y.J. Chao, "Numerical simulation of transient temperature and residual stresses in friction stir welding of 304L stainless steel", *Journal of Materials Processing Technology* 146 (2004) 263-272

52. C. Agelet de Saracibar, M. Chiumenti, D. Santiago, N. Dialami, G. Lombera, "On the numerical modeling of FSW processes", *Proceedings of the International Symposium on Plasticity and its Current Applications, Plasticity 2010*, St. Kitts, St. Kitts and Nevis, January 3-8, 2010

53. C. Agelet de Saracibar, M. Chiumenti, M. Cervera, N. Dialami, D. Santiago, G. Lombera, "Advances in the numerical simulation of 3D FSW processes", to be published on the *Proceedings of the International Symposium on Plasticity and its Current Applications, Plasticity 2011*, Puerto Vallarta, Mexico, January 3-8, 2011